FLORIDA INTERNATIONAL UNIVERSITY

Miami, Florida

HOMO- AND HETEROMETALLIC INDIUM/IRON OXO/HYDROXO POLYNUCLEAR COMPLEXES SUPPORTED BY PYRAZOLE/PYRAZOLATO LIGANDS

A dissertation submitted in partial fulfillment of

the requirements for the degree of

DOCTOR OF PHILOSOPHY

in

CHEMISTRY

by

Susana Herrera

2023

To: Dean Michael R. Heithaus
College of Arts, Sciences and Education

This dissertation, written by Susana Herrera, and entitled Homo- and Heterometallic Indium/Iron Oxo/Hydroxo Polynuclear Complexes Supported by Pyrazole/Pyrazolato Ligands, having been approved in respect to style and intellectual content, is referred to you for judgment.

We have read this dissertation and recommend that it be approved.

Konstantinos Kavallieratos

Christopher Dares

Cheng Yu-Lai

Sonia Underwood

Raphael G. Raptis, Major Professor

Date of Defense: June 27, 2023

The dissertation of Susana Herrera is approved.

Dean Michael R. Heithaus
College of Arts, Sciences and Education

Andrés G. Gil
Vice President for Research and Economic Development
and Dean of the University Graduate School

Florida International University, 2023

DEDICATION

I dedicate this dissertation to my family. To my parents who sacrificed everything so I could pursue my dreams. Without their understanding, motivation, unconditional love and support, the completion of this work would not have been possible.

(Dedico esta disertación a mi familia. A mis padres que sacrificaron todo para que yo pudiese lograr mis sueños. Sin su entendimiento, motivación, amor y apoyo incondicional, completar este trabajo no hubiese sido posible.)

ACKNOWLEDGMENTS

I am forever indebted to my parents, for their bravery to leave everything behind to give me and my brother a better future. I want to acknowledge my boyfriend who has borne with me through all good and hard times, your patience and understanding are unmatchable, and I am forever grateful to have you by my side. I also want to acknowledge the incredible support from my extended family and friends, your patience, help, advice, and encouragement have been a driving force to get me here.

I would like to thank my advisor Professor Raphael G. Raptis who trusted me and guided me teaching me along the way and making me a better scientist and person. I have learned a lot throughout all the years of working next to him and I have come to admire and respect him. I am honored to have such a mentor. I would also like to thank the members of my committee for their advice, guidance, and feedback over the years. I would like to thank our collaborators and technical staff that promoted this work, without your support and help none of this would be possible.

I would also like to thank the National Nuclear Security Administration (NNSA) and Pacific Northwest National Laboratory for choosing me to be an NNSA Graduate Fellow. NGFP gave me the most incredible year and allowed me to work and collaborate with some amazing people along the way. They provided me with an unforgettable experience that allowed me to grow my professional network and expectations and taught me a great deal about myself. I am forever indebted to my colleagues and mentors from Lawrence Livermore National Laboratory who invested their time and supported me since the first day.

Lastly, I would like to thank Prof. Raptis' research group for their invaluable support and friendship: Dr. Indranil Chakraborty, Dr. Kelly Rue, Dr. Eduardo Mollinedo, Reneisha Banner, and Zhichun Shi. I will forever value our coffee breaks. Thank you for sharing your experiences and expertise. I am lucky I got to share this journey with you.

ABSTRACT OF THE DISSERTATION

HOMO- AND HETEROMETALLIC INDIUM/IRON OXO/HYDROXO POLYNUCLEAR COMPLEXES SUPPORTED BY PYRAZOLE/PYRAZOLATO LIGANDS

by

Susana Herrera

Florida International University, 2023

Miami, Florida

Professor Raphael G. Raptis, Major Professor

The main objective of this project is the study of indium as a surrogate for lanthanides and actinides, based on the assumption that cations of similar ionic radii will form similar oxide structures. Chosen as convenient starting materials, a new family of In(III) complexes of formula *mer*-[$InCl_3(pz^*H)_3$] and *trans*-[$InCl_2(4\text{-Me-pzH})_4]^+$, ($pz^*H$ = pzH, 4-Cl-pzH, 4-Br-pzH, 4-I-pzH, 4-Ph-pzH, 4-Me-pzH, and 3,5-Me_2-pzH) was synthesized and characterized by SCXRD, elemental analysis, FTIR, and VT-^{1}H NMR. The results showed the labile nature of indium complexes, and the VT-^{1}H NMR revealed a complex interplay of simultaneous coordination flexibility, dissociation, and tautomerization processes.

Subsequently, higher nuclearity complexes were obtained upon addition of base under various reaction conditions. Hexanuclear complexes of general formula $[In_6Cl_6(\mu_3\text{-}OH_{0.5})(\mu\text{-}OH)_6(\mu\text{-}pz^*)_6]^{3-}$ (pz^* = pz, 4-Cl-pz, 4-Ph-pz) and polymeric species $[In(\mu\text{-}pz^*)_3]_n$ (pz^* = pz, 4-Cl-pz, 4-I-pz, 4-Ph-pz) were isolated and characterized by SCXRD, elemental analysis, ^{1}H NMR, and FTIR. The hexanuclear indium complexes have a novel

motif formed by two trianionic units bridged by both oxo/hydroxo groups. The luminescence properties of the polymeric species showed longer emission lifetimes than previously reported indium luminophores.

Upon deprotonation of the mononuclear indium complexes and the reaction with iron salts both heterobimetallic and homometallic species were isolated. Complexes of general formula $[Fe_{8-x}In_xCl_4(\mu_4\text{-}O)_4(\mu\text{-}pz)_{12}]$ and $[In_{6-x}Fe_xCl_6(\mu_3\text{-}OH_{0.5})(\mu\text{-}OH)_6(\mu\text{-}pz^*)_6]^{3-}$ were isolated and characterized by SCXRD, ESI-MS and SEM-EDS.

The serendipitously prepared complexes $[Fe_7In_2Cl_4(\mu_3\text{-}O)_2(\mu_3\text{-}OH)_2(\mu_3\text{-}OH_{0.5})_2(\mu\text{-}OH)_2(\mu\text{-}4\text{-}Cl\text{-}pz)_{12}(4\text{-}Cl\text{-}pzH)_2](Et_3NHCl)$, $(HNEt_3)_2[Fe_6Cl_2(\mu_3\text{-}O)_2(\mu\text{-}OH)_4(\mu\text{-}4\text{-}Cl\text{-}pz)_{10}]$ and $[Fe_5Cl_3(\mu_4\text{-}O)(\mu_3\text{-}O)(\mu\text{-}OH)_2(\mu\text{-}4\text{-}I\text{-}pz)_6(4\text{-}I\text{-}pz)_4]\cdot(Et_2O)$ were isolated and characterized crystallographically. The latter, with an all-ferric Fe_5O_4-core with a rare "incomplete cubane" topology, like the $[Mn_4CaO_5]$-unit in Photosystem II, was also studied electrochemically, revealing two reductive and one oxidative step to mixed-valent species.

TABLE OF CONTENTS

CHAPTER PAGE

LIST OF TABLES

TABLES PAGE

LIST OF FIGURES

FIGURES PAGE

LIST OF SCHEMES

SCHEMES PAGE

ABBREVIATIONS AND ACRONYMS

CV	Cyclic voltammogram
DCM	Dichloromethane
DMF	Dimethylformamide
DMSO	Dimethylsulfoxide
DPV	Differential pulse voltammogram
EDS	Energy Dispersive X-ray Spectroscopy
ESI-MS	Electrospray Ionisation Mass Spectrometry
FTIR	Fourier transform - infrared
HiPIPs	High potential iron proteins
MOFs	Metal Organic Frameworks
NMR	Nuclear magnetic resonance
OEC	Oxygen-evolving complex
pip	Piperidine
pipH	Piperidinium
pipHCl	Piperidinium chloride
pz	Pyrazolato
pzH	Pyrazole
PXRD	Powder X-ray diffraction
THF	Tetrahydrofuran
UV-Vis-NIR	Ultraviolet - visible - near infrared
SCXRD	Single crystal X-ray diffraction

SEM	Scanning Electron Microscopy
SWV	Square wave voltammogram
TGA	Thermogravimetric analysis
VT	Variable temperature

LIST OF COMPOUNDS

Chapter 2: Indium pyrazole/pyrazolato complexes

mer-$[InCl_3(pzH)_3]$ (1)

mer-$[InCl_3(4\text{-}Cl\text{-}pzH)_3]$ (2)

mer-$[InCl_3(4\text{-}Br\text{-}pzH)_3]$ (3)

mer-$[InCl_3(4\text{-}I\text{-}pzH)_3]$ (4)

mer-$[InCl_3(3,5\text{-}Me_2\text{-}pzH)_3{\cdot}H_2O]$ (5)

mer-$[InCl_3(4\text{-}Ph\text{-}pzH)_3]$ (6)

mer-$[InCl_3(4\text{-}Me\text{-}pzH)_3]$ (7)

trans-$[InCl_2(4\text{-}Me\text{-}pzH)_4]Cl{\cdot}(4\text{-}Me\text{-}pzH)_2{\cdot}(H_2O)$ (8)

$(pipH)_3[In_6Cl_6(\mu_3\text{-}OH_{0.5})(\mu\text{-}OH)_6(\mu\text{-}pz)_6]$ (9)

$(pipH)_3[In_6Cl_6(\mu_3\text{-}OH_{0.5})(\mu\text{-}OH)_6(\mu\text{-}4\text{-}Cl\text{-}pz)_6]$ (10)

$(pipH)_3[In_6Cl_6(\mu_3\text{-}OH_{0.5})(\mu\text{-}OH)_6(\mu\text{-}4\text{-}Ph\text{-}pz)_6]$ (11)

$[In(\mu\text{-}pz)_3]_n$ (12)

$[In(\mu\text{-}4\text{-}Cl\text{-}pz)_3]_n$ (13)

$[In(\mu\text{-}4\text{-}I\text{-}pz)_3]_n$ (14)

$[In(\mu\text{-}4\text{-}Ph\text{-}pz)_3]_n$ (15)

Chapter 3: Synthesis and characterization of heterobimetallic oxide complexes

$[(Fe_{0.64}In_{0.36})_4Fe_4Cl_4(\mu_4\text{-}O)_4(\mu\text{-}pz)_{12}]$ (16)

$(HNEt_3)_3[(In_{0.88}Fe_{0.12})_6Cl_6(\mu_3\text{-}OH_{0.5})_2(\mu\text{-}OH)_6(\mu\text{-}pz)_6]$ (17)

$(HNEt_3)_3[(In_{0.92}Fe_{0.08})_6Cl_6(\mu_3\text{-}OH_{0.5})_2(\mu\text{-}OH)_6(\mu\text{-}4\text{-}I\text{-}pz)_6]$ (18)

Chapter 1: Introduction

1. Metal oxides

Metal oxides play a key role in environmental remediation and are used for several other applications including energy production[1] and storage (e.g., lithium zinc titanium oxides)[2], catalysis (e.g., titanium, zinc, and manganese oxides)[3], and biomedicine.[4,5] Metal oxides exhibit a great variety of functionalities, which are strongly determined by their crystal structure, composition, doping, and intrinsic defects.[6]

1.1. Metal containing proteins in biological systems

Metal oxides can be found in biological systems where they act as catalysts for electron transfer reactions and play a similar role as the better studied metal sulfides. Well-studied example of metalloproteins found in biological systems are ferredoxins, which comprise a large family of iron-sulfur (Fe-S) proteins. The [4Fe-4S] cluster core is found in 4Fe ferredoxins and high potential iron proteins (HiPIPs), which share the same resting state: $[Fe_4S_4]^{2+}$ but have different active sites.[7] Despite sharing the same resting state and being structurally similar, HiPIPs react by oxidation of the resting state at physiological potentials, while 4Fe ferredoxins are reduced (Figure 1).[7,8] A less common [3Fe-4S] cluster is also found in the inactive state of some proteins like aconitase, where interconversion of active [4Fe-4S] cluster to inactive [3Fe-4S] occurs (Figure 2).[9]

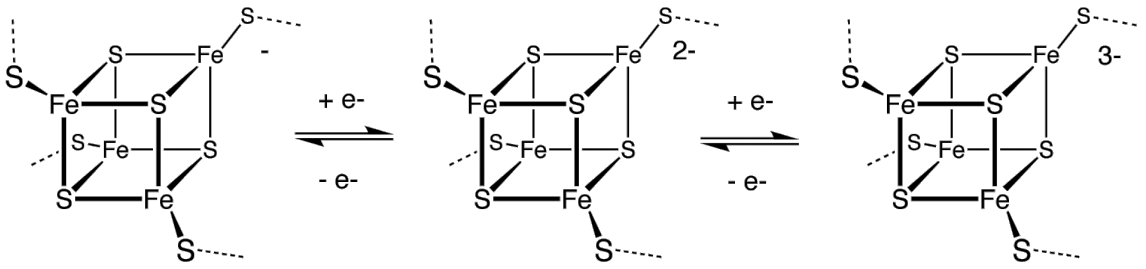

Figure 1. Reduction and oxidation mechanism in low- and high- potential ferredoxins.[7]

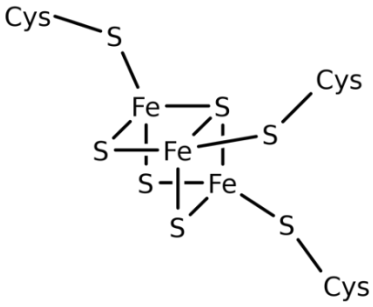

Figure 2. Structural representation of [3Fe-4S] binding unit of ferredoxins.[9]

Analogous rich redox activity, involving a metalloprotein cycling over four discrete oxidation states, is encountered in photosystem II -- its Mn_4CaO_5-core catalyzes the light-driven reaction that oxidizes water, producing energized protons and O_2 (Figure 3).[10] Oxygenic photosynthesis is a fundamental biological process by which cyanobacteria, algae, and plants reduce atmospheric carbon dioxide.[11]

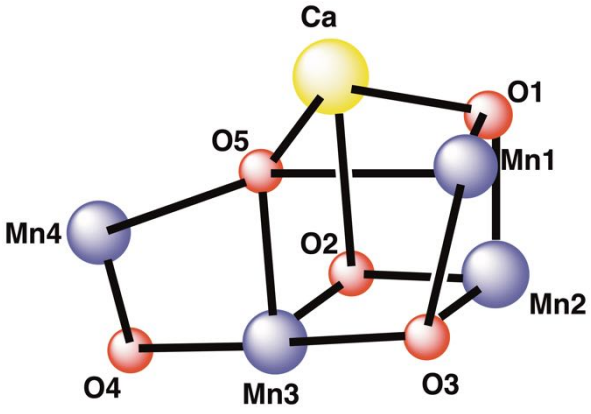

Figure 3. Proposed structure of [Mn_4CaO_5]-unit in the oxygen-evolving complex (OEC) of Photosystem II.[12]

1.2. Iron oxide minerals

Iron is involved in several spinels and inverse spinels, a class of oxide minerals of general formula AB_2O_4 that crystallize in the cubic crystal system,[13] and is known to accommodate several other metals ions in their lattices; for example: magnetite, Fe_3O_4, which is the most abundant inverse spinel, cuprospinel ($CuFe_2O_4$), and trevorite ($NiFe_2O_4$), among others. Iron oxides are found throughout the near-surface environment and regulate migration of pollutants. Adsorption of heavy metals and radionuclides to iron oxides has long been recognized as a permanent immobilization method that may prevent leaching of radioactive materials to the water table. In fact, hydrous oxides have been shown to be the major host mineral for trace elements and isotopes of plutonium and americium.[14] Iron oxides are also known to play an important role in the retention of uranium, with several studies showing successful uranium uptake by amorphous ferric oxyhydroxides.[15,16,17]

1.3. Lanthanide and actinide chemistry

Even though lanthanide and actinide chemistry has come a long way since the middle of the 20th century after the Manhattan Project, much remains unexplored. Many *4f* and *5f* elements have proven immensely versatile, often exceeding what can be accomplished with transition metal systems. However, working with lanthanides and actinides materials is challenging, because of their insolubility,[18] physical properties,[19] limited coordination chemistry and radioactivity (for actinides).

Rare earth elements are widely used in modern technology, from molecular magnets[20–22] to medical imaging agents.[23–25] Their essential role in biological systems was only recently discovered in 2011[19] and it propelled major efforts into the study and continuity of bioinorganic chemistry with principles well established from transition metals. They

also play a role in geopolitical dynamics with their demand only growing in the energy and defense sectors.[26]

Actinides are extremely controversial to society, due to their potentially harmful impact and yet this is what drives the fundamental research and understanding that is essential for their use, disposal, and remediation.[27] Studies of uranium have historically dominated the actinide field. However, the rest of the actinide and transuranic series have started to find a more commonplace, with the most promising advances coming not from the study of one singled out element but the full understanding and continuity across the *4f* and *5f* series.

1.4. Indium and environmental concerns

Indium, discovered and isolated in 1863 by Reich and Richter, has two stable isotopes, ^{115}In and ^{113}In. Other radioisotopes of distinct half-lives are known, the longest-lived being ^{111}In, with a half-life of 2.8 days. Indium was also recognized as a stabilizer for non-ferrous metals, as well as a candidate to form alloys with nobler metal. The supply of the metal has increased exponentially, and its price has dropped greatly over the years. Indium cations are not toxic, to the best of our knowledge.

Indium is stable at two oxidation states, as In^{+} and In^{3+}. With an ionic radius of 0.92 Å,[28] and a d^{10} electronic structure, In^{3+} is a hard (but milder relative to $AlCl_3$, $FeCl_3$) Lewis acid,[29] bonding strongly with hard donor ligands like fluoride, but stable complexes with softer bases and coordination numbers from 4 to 8 are also known.[30] Its chemistry is promising, with recent developments in the fields of polymers, metalorganic frameworks (MOFs), and supramolecular assemblies.

Indium(III)-MOFs, with 6-to-8-coordinate In^{3+}-centers, exhibit intense photoluminescent emission, are excellent candidates for gas storage, having high thermal

and chemical stability.[31] However, other In chemistry is not yet well developed. Most studies of indium complexes involving N-donor ligands focus on homoleptic species and their use as precursors for nitride complexes. Polydentate N-ligands form ^{111}In(III) complexes with promising applications in oncology.[32]

Indium hexahydrates have been recognized in the crystal structure of several indium salts. Indium cation is also easily coordinated by hydroxide and sulfate anions. Its sulfides, [InS] and [In_2S_3] are also known. The oxo anions of indium, including [In_2O_3], and [In_3O_4], are of interest for their unique electronic and optical properties and applications in solar cells, gas absorption, optoelectrical devices and photocatalysis.[33–36] Indium halides are the main starting materials for further indium chemistry. To the best of our knowledge, no work has been published on the coordination chemistry of In^{3+} and pyrazoles.

1.5. Polynuclear complexes of interest

Pyrazole coordination chemistry had been studied since the late 1970's and pyrazolato complexes have been proven to be models of biological protein active sites.[37] Pyrazoles are heterocyclic aromatic rings with three carbon atoms and two nitrogen atoms (Scheme 1). Pyrazole can be monodentate or bidentate pyrazolato chelators by deprotonation of N1. Pyrazoles are versatile and their 5-membered ring is amenable to peripheral substitution, allowing tunning of their properties (Scheme 1 and 2). Both its electron donor ability and steric requirements can be tailored by introduction of the appropriate substituents at the 3, 4, and 5-positions.[38,39]

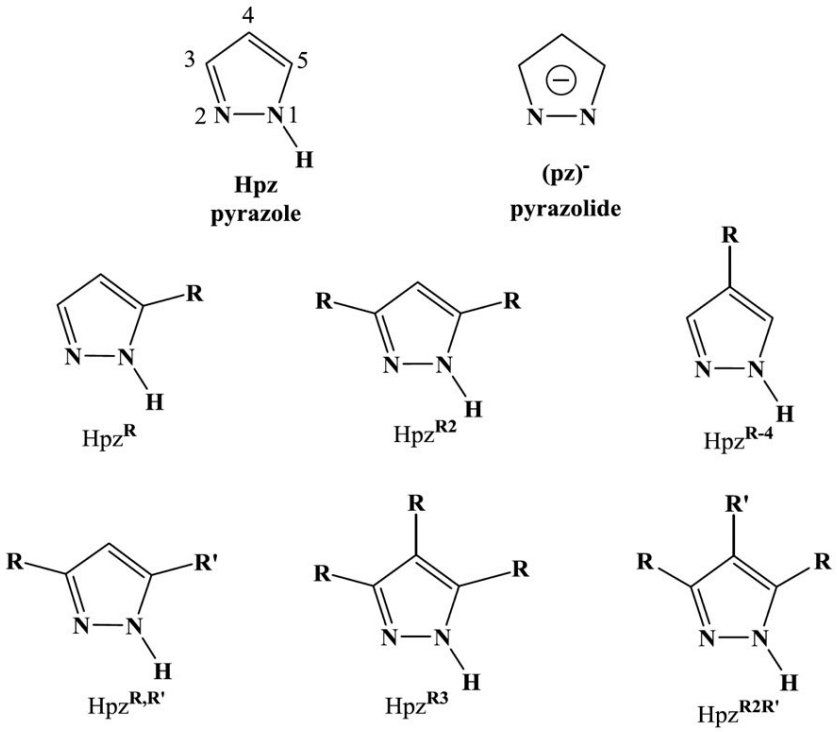

Scheme 1. Substituent positions of pyrazoles (pzH).

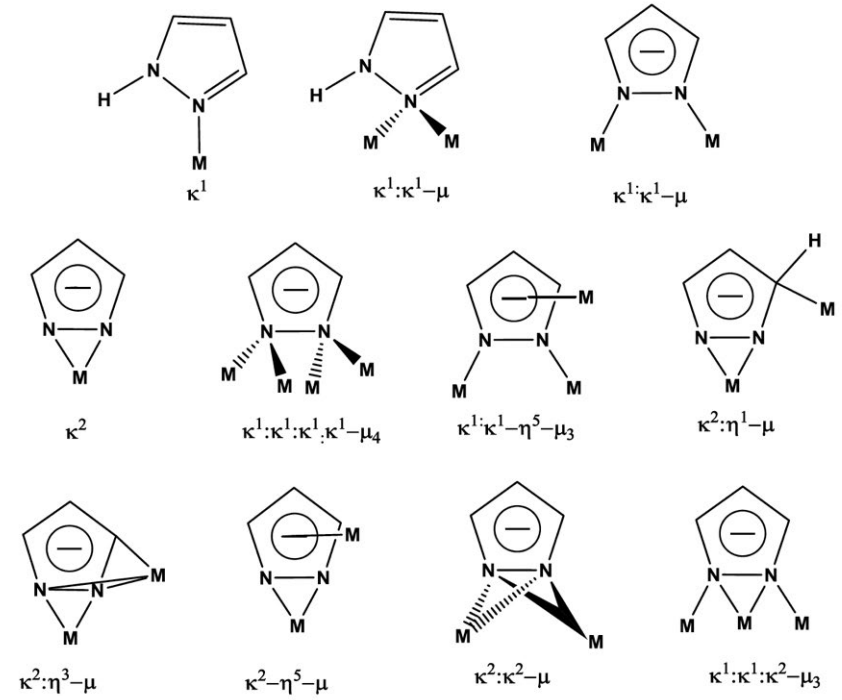

Scheme 2. Coordination modes of pyrazoles (pzH) and pyrazolato anions (pz).[38]

1.5.1. Octanuclear iron pyrazolato complexes

Iron(III) species are commonly found in Nature. The hydrolysis of Fe(III) species is of relevance, due to water being the principal solvent in the natural environment. Upon hydrolysis, its uncontrollable polymerization leads to the formation of several oxide/hydroxide minerals. Dr. Raptis' group has explored methods of controlling the mineral growth by arresting the hydrolytic polymerization with organic ligands that occupy peripheral iron coordination sites. Synthetic octanuclear iron complexes containing a redox-active Fe_4O_4-cubane core using pyrazolato bridging ligands have been one of the focuses of such efforts. They have described in a series of publications the structural, spectroscopic, magnetic, and redox properties of a family of redox-active octanuclear complexes of formula $[Fe^{III}_8(\mu_4\text{-}O)_4(\mu\text{-}pz^*)_{12}X_4]$, where pz^* = 4-substituted pyrazolato anion and X = Cl, Br and NCS (Figure 4).[40] Additionally, X = N_3 and OAr species have been prepared, but not published yet. These complexes consist of an $Fe_4(\mu_4\text{-}O)_4$-cubane surrounded by four additional outer Fe-atoms, twelve bridging pyrazolato ligands and four terminal X ligands. The $Fe_8(\mu_4\text{-}O)_4$-core is the same as the repeat units of the minerals maghemite, magnetite, and ferrihydrite (Figure 5).

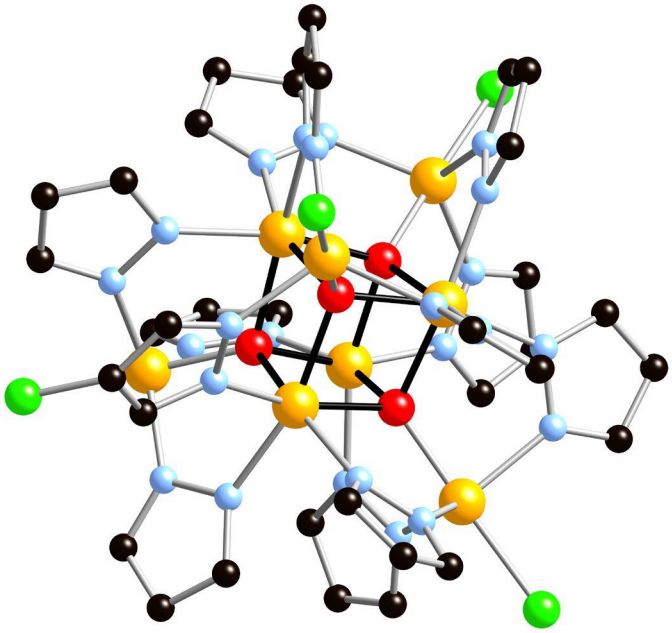

Figure 4. Ball-and-stick representation of $[Fe^{III}_8Cl_4(\mu_4\text{-}O)_4(\mu\text{-}pz)_{12}]$ (Fe, yellow; Cl, green; O, red; N, blue; C, black).[41]

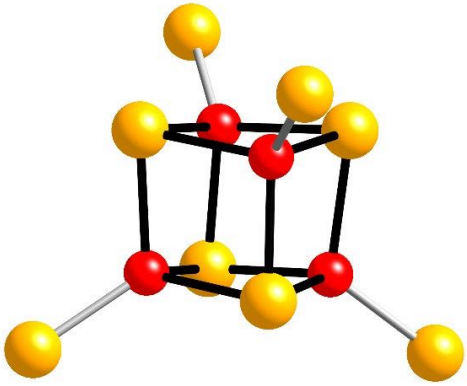

Figure 5. Structure of the Fe_8O_4 core of $[Fe^{III}_8X_4(\mu_4\text{-}O)_4(\mu\text{-}pz^*)_{12}]$.

Furthermore, ^{57}Fe-Mossbauer spectroscopy has shown that these Fe_8 compounds are also electronic analogues of iron minerals, allowing the study of these mineral-model materials in its various accessible oxidation states. These complexes possess exceptional redox activity, consisting of four consecutive one-electron reduction steps spaced by 0.25 - 0.35 V from each other (Figure 6), converting the all-ferric starting complex, $[Fe_8]^0$, into

a series of mixed-valence species of the form $[Fe_8]^{-/2-/3-/4-}$.[41] The redox potentials vary with different terminal ligands and pyrazolato ligands.

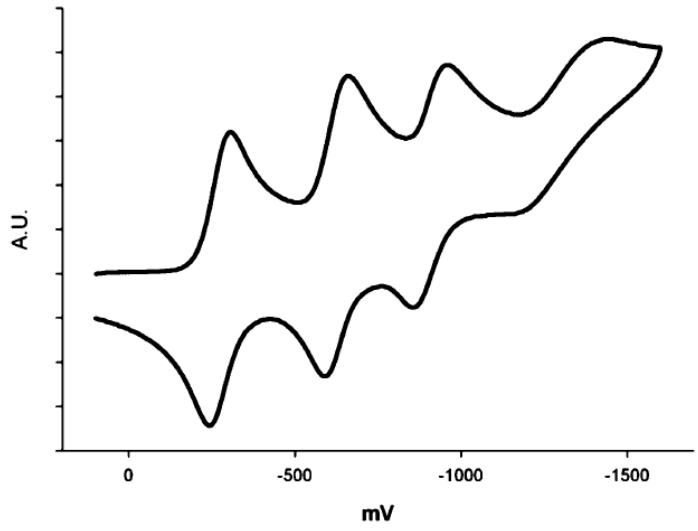

Figure 6. Cyclic voltammogram of $[Fe^{III}_8(\mu_4\text{-}O)_4(\mu\text{-}pz)_{12}Br_4]$ in 0.5 M $TBAPF_6$/DCM, Pt -disk working electrode, *vs.* Fc^+/Fc.[41]

Variable temperature magnetic susceptibility studies have revealed a weak antiferromagnetic coupling (J_1/hc = -2.1 cm^{-1}) within the cubane and a stronger antiferromagnetic coupling (J_2/hc = -50.6 cm^{-1}) between the cubane and the outer Fe-atoms, resulting in a diamagnetic ground state and a wide-spaced ladder of excited spin states.[41] Even though, spin states from S = 0 to S = 20 are possible in theory for the eight high-spin Fe(III) centers, because of the wide spacing, only the lowest three or four states are populated at ambient temperature, resulting in a μ_{eff} of 7.0 B.M.

1.6. Hypothesis and rationale

Main group trivalent ions, like Ga^{3+} and In^{3+}, have been shown by the Raptis group to form $[Fe_{8-x}M_x]$ heterobimetallic materials whose structural unit models the structures of the iron oxide minerals maghemite [γ-Fe_2O_3], ferrihydrite [$Fe_5O_3(OH)_9$] and magnetite

[Fe_3O_4] (unpublished results). Given that the crystal radii of Ga^{3+} (0.76 Å) and In^{3+} (0.94 Å) span the crystal radii of several lanthanides and actinides, it is reasonable to believe that formation of Fe/Ln and Fe/An octanuclear pyrazole/pyrazolato compounds modeling natural or synthetic Fe/Ln- and Fe/An-oxides is possible.

Magnetic oxides exhibit ferromagnetism, electrical conductivity, and have high working temperatures. Nanoparticles of general formula FeM_2O_4, where M = Al^{3+}, Ga^{3+} have previously been synthesized by furnace heating. These can possess the inverse spinel structure inherited from magnetite, but the magnetic properties can be tunable, making possible to potentially use them as magnetic-resonance imaging contrast agents.[42,43] While some spinels like $FeAl_2O_4$ are well studied materials, other, like $FeGa_2O_4$, are poorly understood, and some like $FeIn_2O_4$ have not been studied at all. Therefore, any new Fe/In, Fe/Ln or Fe/An complex can be calcinated to identify possible formation of new mixed-metal oxide phases. Indium can be used as a surrogate for the Fe/Ln- and Fe/An-oxide-pyrazolato complexes to fully characterize and optimize the procedures and obtain a spectroscopic fingerprint.

The current research focuses on developing new well-defined heterobimetallic pyrazolato complexes as models of mixed-metal oxide minerals. The study of indium pyrazole/pyrazolato chemistry has not been developed elsewhere. The following strategies have been applied towards the overall goal of this project:

1) Synthesis and characterization of mononuclear indium pyrazole adducts to be further used as starting materials for the preparation of polynuclear species.

Pyrazole can be deprotonated to form bridging bidentate anions. Polynuclear homometallic and heterometallic complexes can be synthesized starting from mononuclear

pyrazolato anions. Mononuclear iron(III) pyrazole complexes have been isolated and employed to synthesize trinuclear and octanuclear iron pyrazolato species (Scheme 3).[40] The synthesis of analogous mononuclear indium(III) complexes is a practical approach to obtain homometallic indium pyrazolato complexes as well as heterobimetallic $[Fe^{III}_{8-x}In_x(\mu_4\text{-}O)_4(\mu\text{-}pz^*)_{12}X_4]$ complexes.

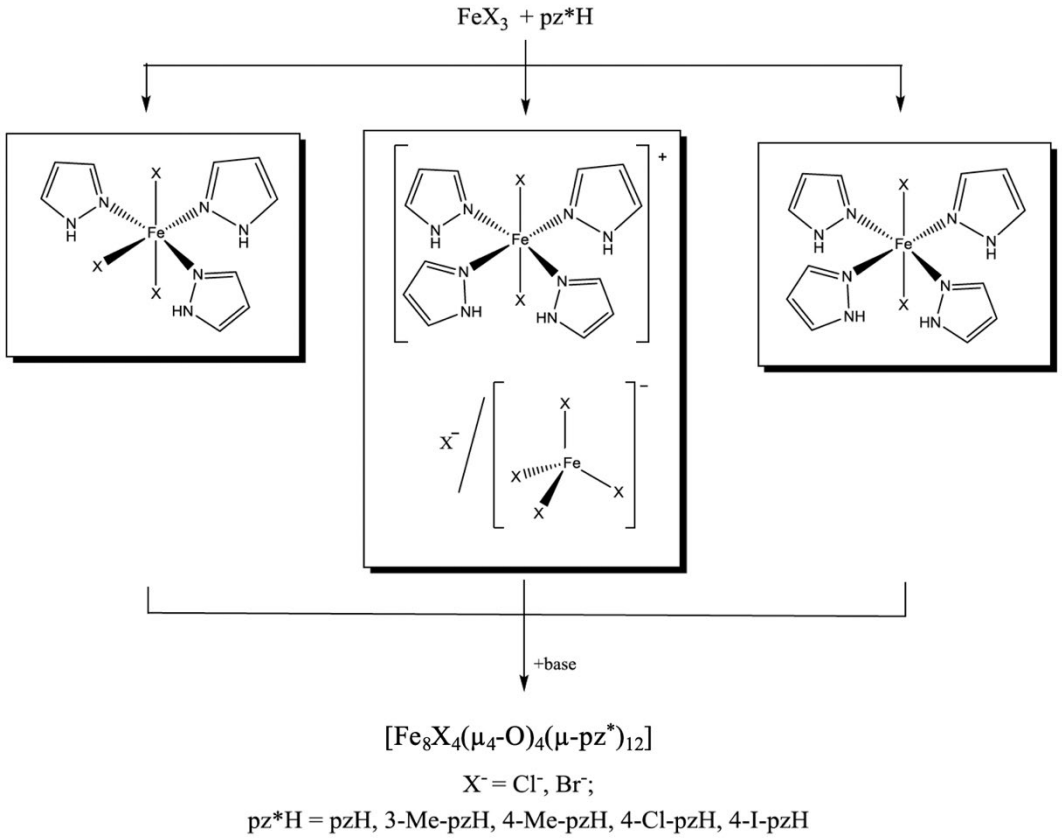

Scheme 3. Mononuclear ferrous and ferric pyrazole adducts as intermediate in the polynuclear Fe^{III} pyrazolato synthesis.[40]

2) Synthesis and characterization of homometallic and heterobimetallic pyrazolato complexes as surrogates for the preparation of iron-lanthanide and iron-actinide species.

Deprotonation of mononuclear pyrazole complexes will allow synthesis of homometallic indium(III) complexes not previously studied, as well as preparation of

Fe/In-hydroxo/oxo pyrazolato complex to identify suitable synthetic procedures towards these heterobimetallic compounds and the spectroscopic study of their $[(Fe/In)_n]$ core. The long -term goal is to adopt the synthetic protocols towards the preparation of Fe/Ln- and Fe/An-hydroxo/oxo pyrazolato complexes and fully characterize them.

Chapter 2: Indium pyrazole/pyrazolato complexes

2. Synthesis of mononuclear indium pyrazole complexes

2.1. Introduction

Mononuclear complexes containing monodentate pyrazoles are convenient starting materials for the synthesis of oligonuclear and polynuclear homometallic and heterometallic complexes upon deprotonation, turning the monodentate pyrazole (κ^1-pz*H) into a bridging pyrazolato (μ, κ^2-pz*) ligand (pz*H = substituted pyrazole). Several transition metals have been reported to form polynuclear pyrazolato complexes; however, only one relevant dinuclear indium complex containing a chelating 1-(2-hydroxyethyl)-2,5-dimethylpyrazolato has been reported to date.[44] Complexes of the form *mer*-[MX_3(pz*H)$_3$] where M = Cr, Fe, Rh, and Re, X = Cl and Br, have previously been reported,[40,45–48] serving as starting materials for the synthesis of dinuclear and polynuclear complexes.[41,44,49] Complexes of the form *trans*-[MX_2(pz*H)$_4$] where M = Os, Ni, Fe, Cu, Cr, Mn, Co, Rh, Cd, Hg, Ru, Ga, and Zn, X = Cl, have previously been reported as well.

Herein we report the synthesis, crystal structure, and dynamic solution ^{1}H-NMR behavior of the first series of six mononuclear In(III)– pyrazole complexes of general formula *mer*-[MX_3(pz*H)$_3$] and co-crystallized *mer*-[$In^{III}Cl_3$(4-Me-pzH)$_3$] and *trans*-[$In^{III}Cl_2$(4-Me-pzH)$_4$]Cl·(4-Me-pzH)$_2$·(H_2O) species. The syntheses of three hexanuclear indium pyrazolato complexes and four indium pyrazolato polymers by further deprotonation of the mononuclear In(III) complexes are reported as well (Scheme 4).

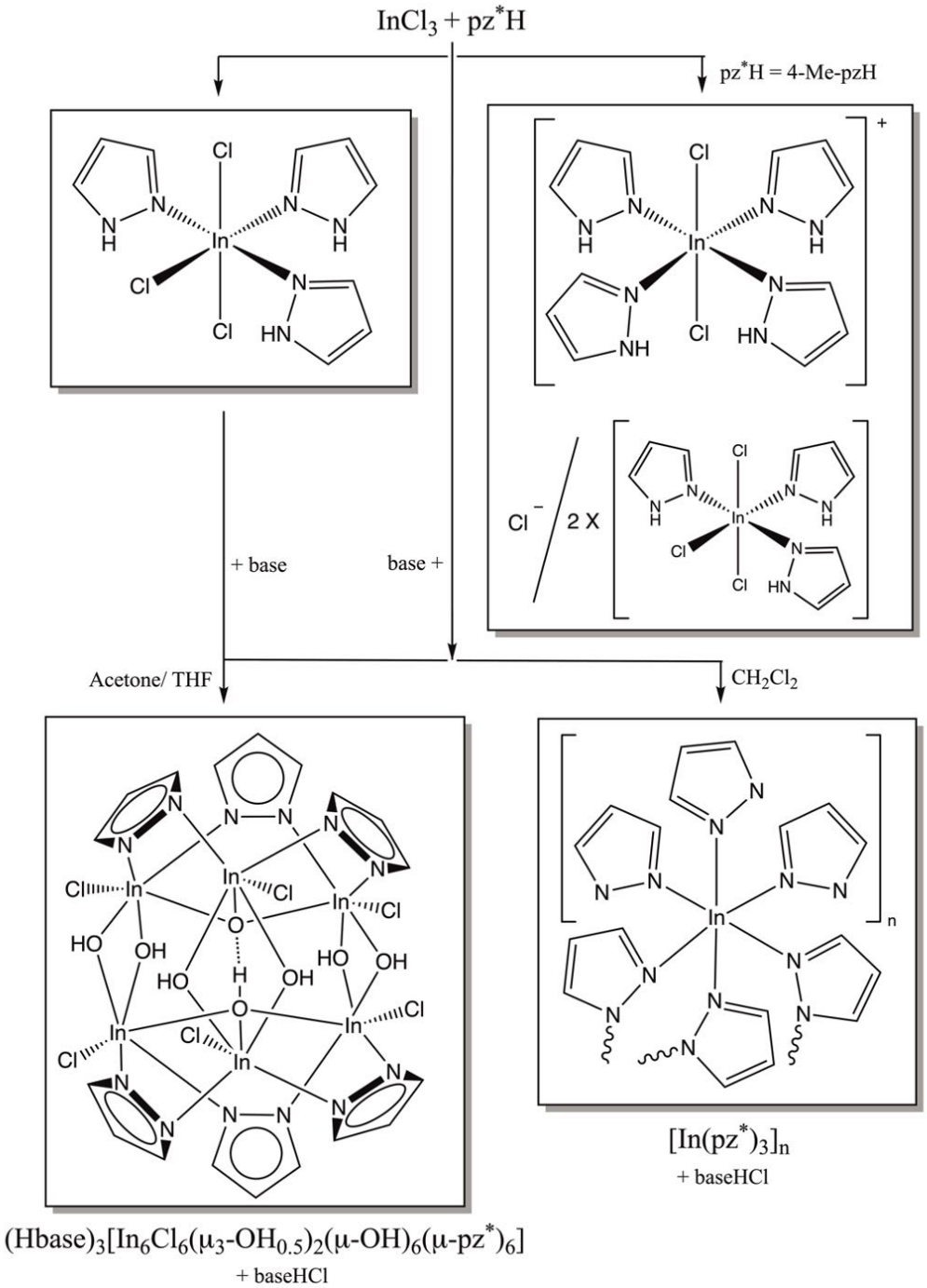

pz*H/pz* = pzH, 4-Cl-pzH, 4-Br-pzH, 4-I-pzH, 4-Ph-pzH, 4-Me-pzH, 3,5-Me_2-pzH

base = piperidine (pip), triethylamine (Et_3N)

Scheme 4. Synthetic pathway for In(III) mononuclear, hexanuclear, and polymeric pyrazole/pyrazolato complexes.

2.2.Results and Discussion

2.2.1. Synthesis of In(III) pyrazole monomers (partially published in *Dalton* **2022**, *5*1, 14277-14286)[50]

Complexes **1 – 6** of general formula *mer*-[$In^{III}Cl_3(pz^*H)_3$], where pz^*H = pzH, 4-Cl-pzH, 4-Br-pzH, 4-I-pzH, 4-Ph-pzH, and 3,5-Me_2-pzH, were prepared by reacting anhydrous $InCl_3$ and pz^*H in CH_2Cl_2 and recrystallized as colorless prism-like crystals (Scheme 4).

Complexes of formula *mer*-[$In^{III}Cl_3$(4-Me-pzH)$_3$] (**7**) and *trans*-[$In^{III}Cl_2$(4-Me-pzH)$_4$]Cl·(4-Me-pzH)$_2$·(H_2O) (**8**) were prepared from a reaction mixture of anhydrous $InCl_3$ and 4-Me-pzH in MeOH (Scheme 4). Recrystallization of the reaction product yielded **7** and **8** as visually indistinguishable, colorless, prism-like crystals. In solution, species **7** and **8** are in dynamic equilibrium (*vide infra*), rendering any efforts to isolate them worthless.

2.2.2. Crystallographic description of In(III) monomers

Crystallographic data collection and refinement parameters for complexes **1 – 5** and **7 – 8** are summarized in Table 8. Complexes **1 – 5** crystallized with one whole molecule per asymmetric unit. Complexes **1** and **5** crystallized in monoclinic $P2_1/n$ space group. Complexes **3** and **4** crystallized in monoclinic $C2/c$ space group and complex **2** crystallized in triclinic *P*-1 space group. Complexes **7** and **8** crystallized in orthorhombic $P2_12_12_1$ and triclinic *P*-1 space groups, respectively. Complex **8** crystallized with two half-molecules related by an inversion center on the metal atom, one chloride counter ion, two pyrazoles, and one water molecule per asymmetric unit. All complexes contain a 6-coordinate

pseudooctahedral In(III)-center with *mer*-[$InCl_3(pz^*H)_3$] or *trans*-[$InCl_2(pz^*H)_4$]$^+$ coordination sphere.

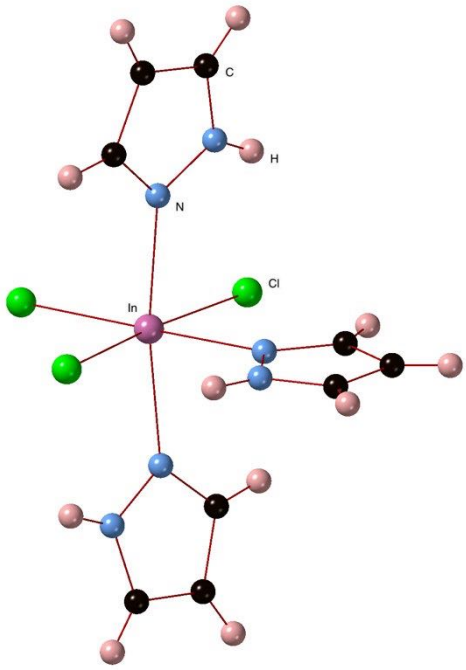

Figure 7. Ball-and-stick representation of *mer*-[$InCl_3(pzH)_3$] (**1**).

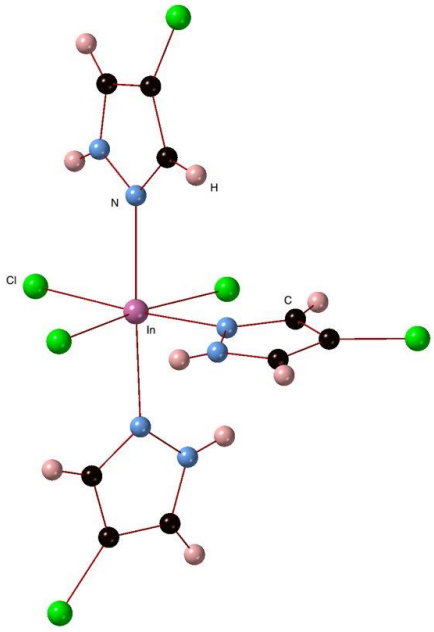

Figure 8. Ball-and-stick representation of *mer*-[$InCl_3(4\text{-}Cl\text{-}pzH)_3$] (**2**).

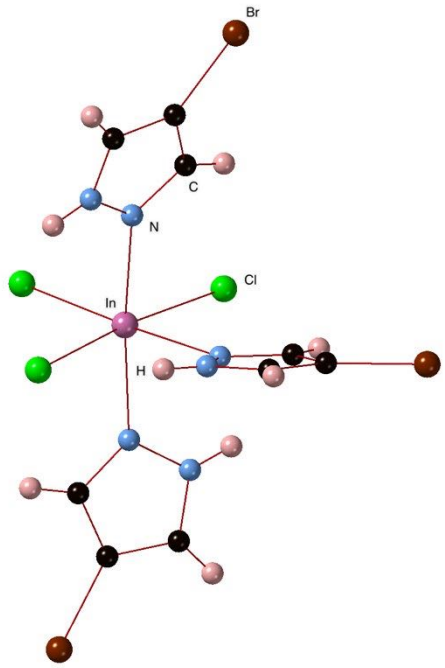

Figure 9. Ball-and-stick representation of *mer*-[$InCl_3$(4-Br-pzH)$_3$] (**3**).

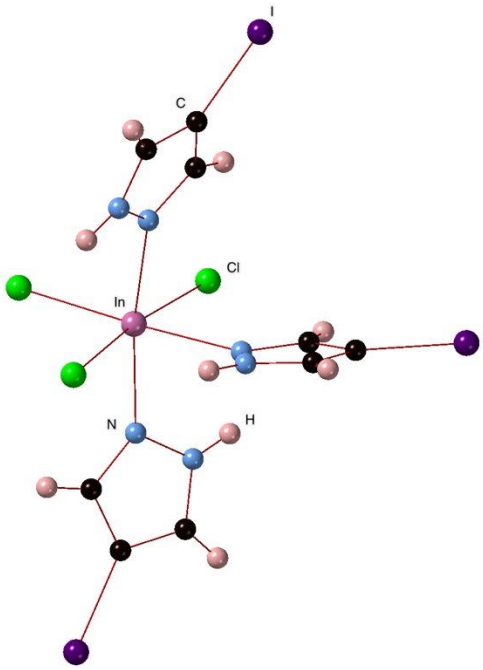

Figure 10. Ball-and-stick representation of *mer*-[$InCl_3$(4-I-pzH)$_3$] (**4**).

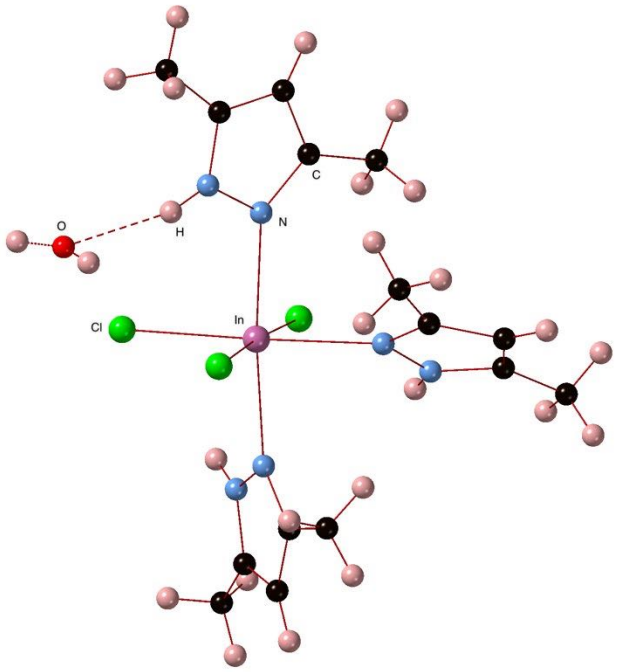

Figure 11. Ball-and-stick representation of *mer*-[$InCl_3$(3,5-Me_2-pzH)$_3$]·(H_2O) (**5**).

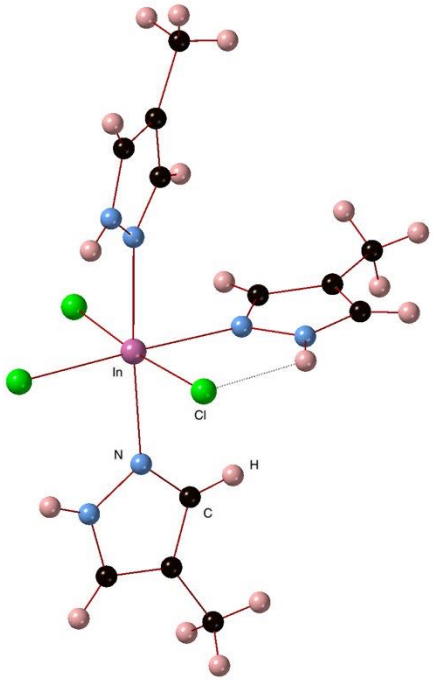

Figure 12. Ball-and-stick representation of *mer*-[$InCl_3$(4-Me-pzH)$_3$] (**7**).

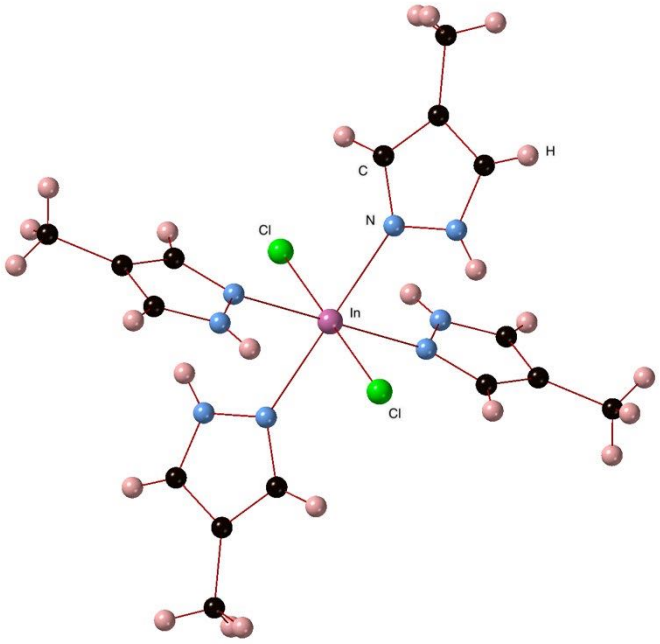

Figure 13. Ball-and-stick representation of *trans*-$[InCl_2(4\text{-Me-pzH})_4]^+$ cation (**8**). Chloride counter ion, free pyrazoles and H_2O solvent molecule omitted.

For the four *mer*-complexes of 4-R-substituted pyrazoles (**1 – 4**), the In – N bonds *trans* to a halogen atom are statistically indistinguishable from those *trans* to another pyrazole, similarly to analogous *mer*-$[FeCl_3(pz^*H)_3]$ and *mer*-$[CrCl_3(pz^*H)_3]$.[40,41,45,51–57] However, for the 3,5-Me_2-substituted complex (**5**), the In – N bond *trans* to a halogen atom is shorter than those *trans* to a pyrazole. No crystals appropriate for X-ray structure determination of complex **6** have been obtained, yet. Complexes **1 – 5** have θ_1 (N_{trans}– In – N_{trans}) in the range of 170.36(7)° – 177.89(8)° and θ_2 (Cl_{trans} – In – Cl_{trans}) of 170.94(2)° – 176.58(5)°. The *cis* pyrazoles are approximately coplanar with the *mer*-$InCl_3$ moiety, while the *trans* pyrazoles are in anti-arrangement, except in **5**. Selected bond distances and angles for complex **1 – 5** are listed in Table 1 and 2, respectively. Complex **2** is isostructural to the analogous ferric compound, *mer*-$[FeBr_3(4\text{-Cl-pzH})_3]$.[40]

In complexes **7** and **8** the In – N bonds *trans* to a halogen atom are statistically indistinguishable from those *trans* to another pyrazole. The bond lengths and angles of complexes **7** and **8** are within experimental error from each other. Selected bond distances and angles for complex **7** and **8** are listed in Table 3 and 4, respectively.

Table 1. Selected bond lengths (Å) for **1 – 5**.

	Compound				
Bond	**1**	**2**	**3**	**4**	**5**
In – Cl	2.47(1)[a]	2.44(1)[a]	2.48(7)[a]	2.48(1)[a]	2.51(1)[a]
	2.45(3)[b]	2.45(5)[b]	2.45(1)[a]	2.46(1)[a]	2.46(3)[b]
	2.48(4)[a]	2.47(5)[a]	2.45(1)[b]	2.45(1)[b]	2.46(1)[a]
In – N	2.26(1)[a]	2.26(1)[a]	2.26(1)[a]	2.26(1)[a]	2.30(1)[a]
	2.30(1)[b]	2.30(3)[b]	2.27(1)[a]	2.27(1)[a]	2.29(1)[b]
	2.26(1)[a]	2.27(1)[a]	2.31(1)[b]	2.32(1)[b]	2.29(3)[a]

[a]*trans*-Cl – In – Cl, or *trans*-N – In – N bonds
[b]*trans*-Cl – In – N bonds

Table 2. Selected bond angles (°) for **1 – 5**.

	Compound				
Bond Angle	**1**	**2**	**3**	**4**	**5**
N – In – N	84.67(7)	88.07(8)	81.8(2)	81.3(3)	87.0(1)
	85.76(7)	90.77(8)	90.5(2)	89.4(3)	87.7(1)
	170.36(7)	177.79(8)	172.3(2)	170.6(3)	174.7(2)
Cl – In – N	84.94(5)	84.65(5)	85.9(2)	86.3(2)	84.6(1)
	95.99(5)	93.50(6)	94.4(2)	94.8(2)	94.2(1)
	176.60(5)	175.17(6)	176.0(2)	175.9(2)	176.2(1)
Cl – In – Cl	95.46(2)	93.07(3)	92.14(6)	92.28(9)	90.70(5)
	92.15(2)	95.88(3)	95.47(6)	95.10(9)	91.14(5)
	172.39(2)	170.94(2)	172.28(6)	172.49(9)	176.58(5)

Table 3. Selected bond lengths (Å) for **7** and **8**.

	Compound	
Bond	**7**	**8**
In – Cl	2.51(1)[a]	2.44(5)
	2.46(3)[b]	2.45(1)
	2.46(1)[a]	
In – N	2.30(1)[a]	2.26(2)
	2.29(1)[b]	2.26(7)
	2.29(3)[a]	2.25(5)
		2.25(4)

[a]*trans*-Cl – In – Cl, or *trans*-N – In – N bonds
[b]*trans*-Cl – In – N bonds

Intermolecular interactions associated with distances shorter than the sum of the van der Waals radii of nearby atoms are considered bonding.[58] All intermolecular bonding interactions are characterized by a directional preference in which contacting atoms orient themselves. Among all bonding interactions, halogen ··· halogen interactions have been well characterized within four different types: type I ($90° < \theta_1 \approx \theta_2 < 180°$), θ_1 = A-halogen ··· halogen angle and θ_2 = halogen ··· halogen-B angle, where A and B refer to the atoms attached to halogen atom and van der Waals forces are dominant; type II ($\theta_1 = 180°$ and $\theta_2 = 90°$) where electrostatic forces are dominant; type III ($\theta_1 \approx \theta_2 = 180°$) where dispersion forces are dominant; and type IV ($\theta_1 \approx \theta_2 = 90°$) where dispersion forces are the most prevalent contributions (Scheme 5).[59]

Table 4. Selected bond angles (°) for **7** and **8**.

	Compound	
Bond Angle	**7**	**8**
N – In – N	87.7(2)	93.9(2)
	87.9(2)	91.1(2)
	175.6(2)	180.0
Cl – In – N	87.2(2)	90.3(1)
	93.1(2)	90.6(1)
	177.7(2)	87.7(1)
		91.0(1)
Cl – In – Cl	90.72(7)	
	94.57(6)	180.0
	174.63(7)	

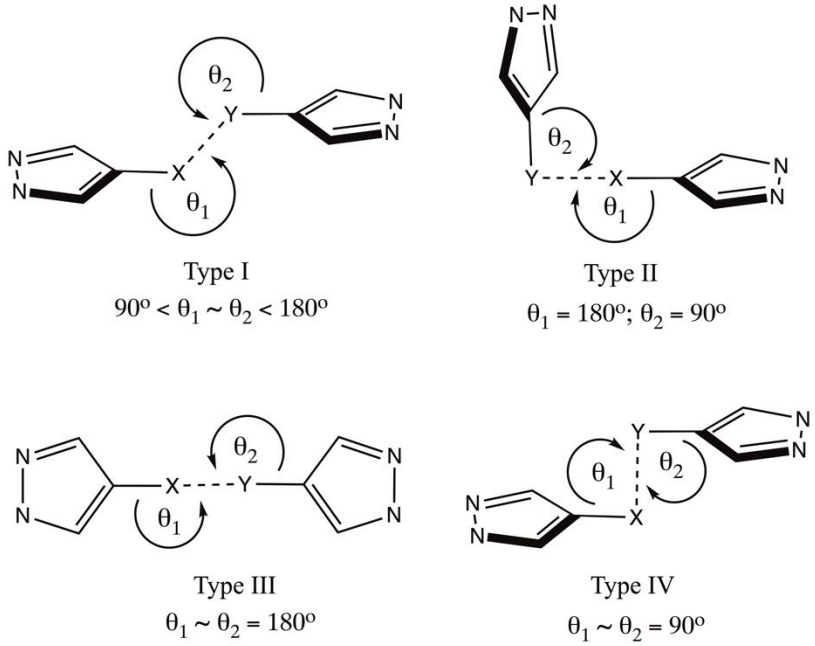

Scheme 5. Structural representation of the four types of halogen (X) ··· halogen (Y) intermolecular bonding interactions.

Halogen ··· halogen interactions give rise to close packing for **2** and **4**, exhibiting a type I, R – X ···Y – R contact interaction (X, Y = halogen atoms). Complex **2** shows Cl1 ··· Cl3 distance, C2 – Cl1 ··· Cl3 angle, and Cl1 ··· Cl3 – C8 angle equal to 3.347 Å, 161.92°,

and 102.21°, respectively, from two 4-Cl-pyrazole ligands to another two pyrazole ligands in the adjacent monomer, resulting in a 2D network observed in the crystal packing diagram in Figure 14. Complex **4** shows I2 ··· Cl1 distance of 3.652 Å, shorter than the sum of the van der Waals radii, C5 – I2 ··· Cl1 angle and I2 ··· Cl1 – In angle of 153.31° and 123.67°, respectively, from a 4-I-pyrazole ligand to an adjacent chloride ligand. The Cl ··· I intermolecular bonding in **4** results in a 1D chain depicted in Figure 15. Intermolecular halogen bonding distances and angles are listed in Table 5. Halogen-halogen bonding distances for **3** are longer than the sum of their van der Waals radii.

Table 5. Halogen ··· halogen bond geometry for **2** and **4** and sums of van der Waals radii.

Sum van der Waals radii/Å[58]	**Compound**	A – X – Y	d(X – Y)/Å	A – X – Y/°
3.52	**2**	C2 – Cl1 ··· Cl3 (θ_1) Cl1 ··· Cl3 – C8 (θ_2)	3.347	161.92 102.21
3.73	**4**	C5 – I2 … Cl1 (θ_1) I2 … Cl1 – In (θ_2)	3.652	153.31 123.67

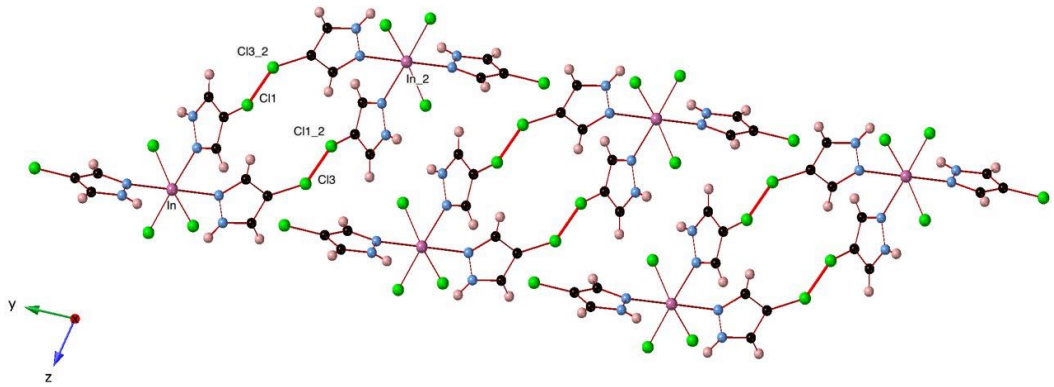

Figure 14. Illustration of crystal packing of **2**, showing two 1D chains linked by intermolecular halogen bonding (red lines).

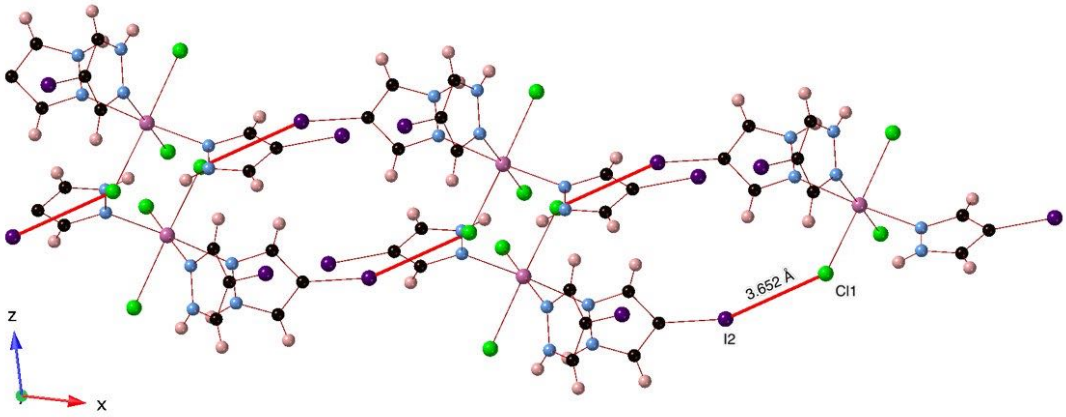

Figure 15. Illustration of crystal packing of **4**, showing two 1D chains linked by intermolecular halogen bonding (red lines).

2.2.3. Nuclear magnetic resonance of In(III) monomers

Indium(III) has a d^{10} electronic configuration and is diamagnetic. In the case of complexes **1 – 6** of general formula *mer*-[$InCl_3(pz^*H)_3$], the spectra should contain two distinct pyrazole environments, one corresponding to the two pyrazoles *trans* to each other and to the pyrazole in the *cis* position. Due to metal coordination to N2, *mer*-In(III) with 4-R-substituted pyrazoles should show nonequivalent H^3 and H^5, so that for complexes **1** and **5**, a total of eight resonances should appear in the NMR; and for **2 – 4** and **6**, six and twelve resonances should be observed, respectively.

Contrary to expectation, all **1 – 6** showed fewer resonances in THF-d_8 and dimethylsulfoxide-d_6. Spectra of **1** showed a singlet at 12.40 ppm, a doublet at 7.76 ppm, and a triplet at 6.32 ppm with integration 1:2:1 in THF-d_8 (Figure 16). These peaks were assigned to the H^1-pz, $H^{3,5}$, and H^4, respectively. Similarly, spectra of **2** showed a singlet at 12.30 and a singlet at 7.63 with integrations 1:2, assigned to H^1-pz and $H^{3,5}$ in THF-d_8 (Figure 16). Spectra of **3** and **4** showed separation of the resonances for H^3 and H^5, with **3**

showing peaks at 13.19 ppm, 7.97 ppm, and 7.56 ppm; and **4** showing peaks at 13.17 ppm, 7.93 ppm, and 7.55 ppm with integration 1:1:1, assigned to H^1-pz, H^3 and H^5, respectively (Figure 17). Spectra of **5** also showed 3 resonances at 11.99 ppm for H^1-pz, 5.73 ppm for H^4, and at 2.11 ppm for C – $H_3^{3,5}$ with integration 1:1:6 (Figure 17). Lastly, spectra of **6** showed a peak at 12.93 corresponding to H^1-pz, and two singlets at 8.18 ppm and 7.91 ppm assigned to H^3 and H^5 (Figure 17). The resonances for the phenyl group in the 4-postion was assigned with both vicinal coupling and long-range coupling observed: a doublet of doublets at 7.60 ppm assigned to H^{ortho}-Ph-pz, a triplet of triplets at 7.34 ppm assigned to H^{meta}-Ph-pz, and a triplet of triplets at 7.17 ppm assigned to H^{para}-Ph-pz. The integration for spectra of **6** was 1:1:1:2:2:1.

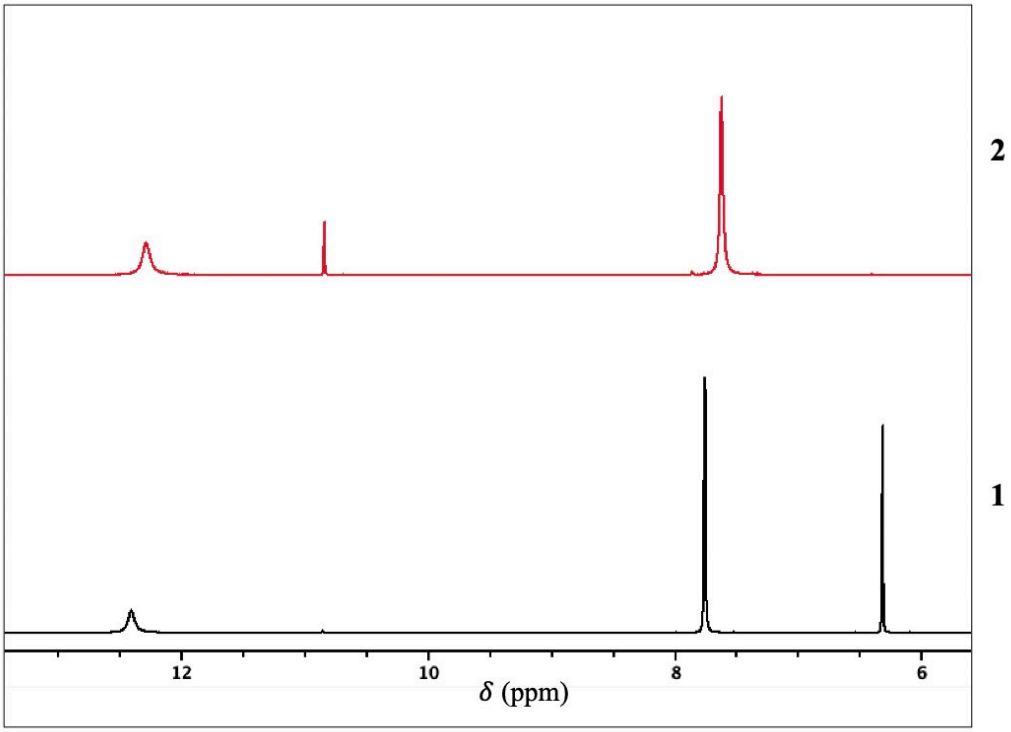

Figure 16. ^{1}H NMR of complex **1** (black) and **2** (red) in THF-d_8 at ambient temperature 400 MHz.

The ambient temperature ^{1}H NMR spectra of **1 – 6**, showing a single set of resonances, is inconsistent with the solid-state structure of the complexes. These spectra indicate a dynamic solution behavior -- the latter comprising (at least) three simultaneous processes: pyrazole N – H proton dissociation/association, *cis*/*trans*-pyrazole exchange, and N^1/N^2 tautomerization of the *cis*- and of the *trans*-pyrazoles (Scheme 6).

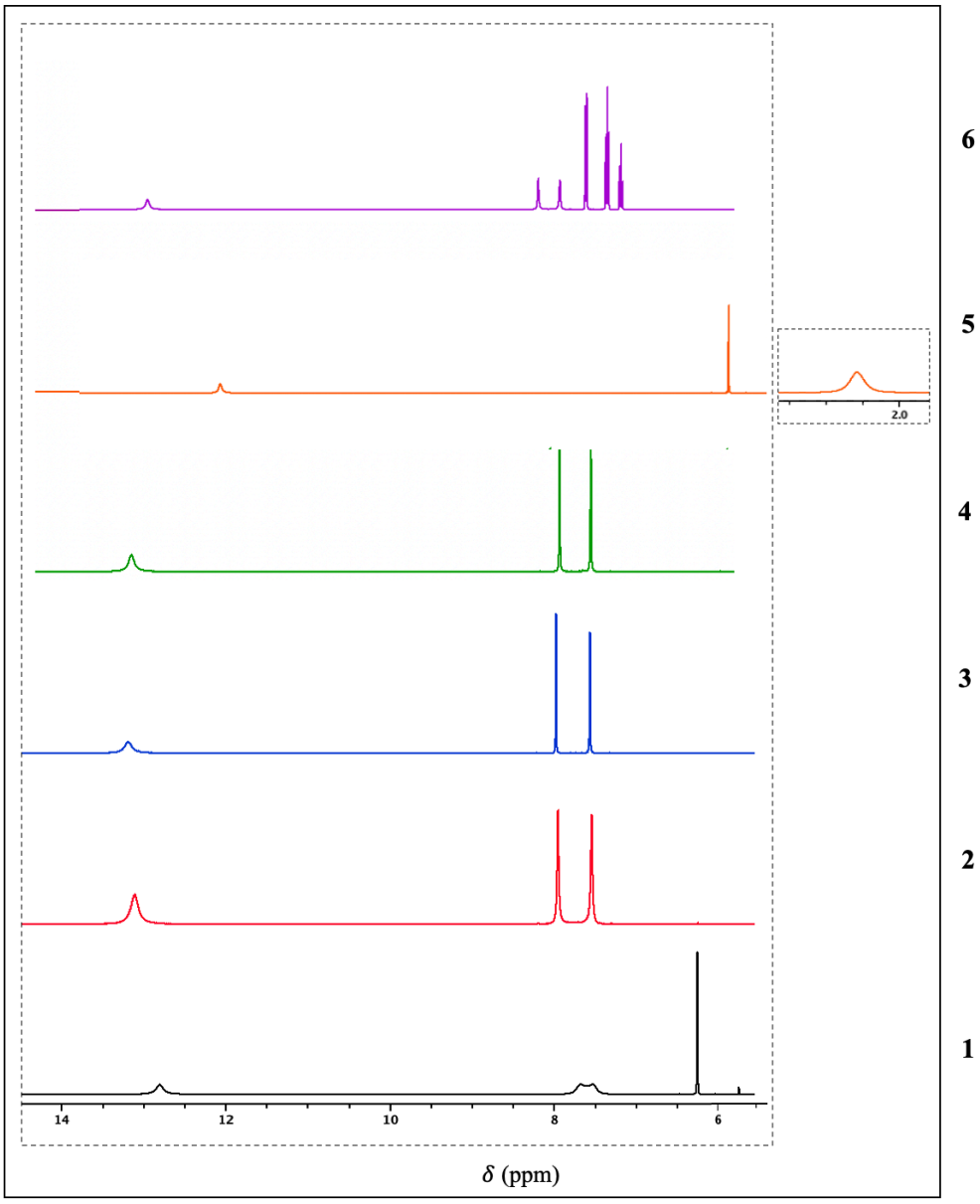

Figure 17. ^{1}H NMR of complex **1** (black), **2** (red), **3** (blue), **4** (green), **5** (orange), and **6** (purple) in DMSO-d_6 at ambient temperature 400 MHz.

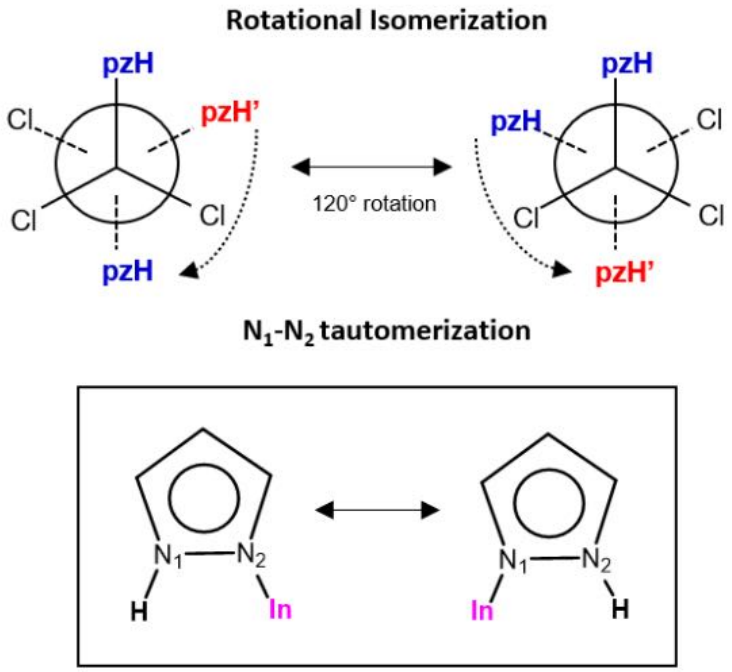

Scheme 6. Dynamic behavior of complex **1**, as determined by VT-^{1}H NMR showing rotational isomerization (upper) and N_1 - N_2 tautomerization and N-H dissociation/association (lower).

To probe the dynamic processes, the ^{1}H NMR spectra of **1** were recorded in THF-*d*$_8$ solution in the 328 K to 173 K range (Figure 18). The spectra at or above 243 K show a single set of three resonances, inconsistent with the solid-state structure of **1**, The N – H proton resonance is further broadened by unresolved coupling to quadrupolar ^{14}N. The assignment of the $H^{3,5}$ and H^{4} peaks was based on their 2:1 integrated intensity, while the assignment of the N – H was based on the observation that this resonance is absent in spectra recorded in protic solvents, such as $CDCl_3$.

As expected, all three resonances are shifted downfield with respect to free pyrazole (Figure 19) because of coordination to the In(III)-center, and shift further downfield with decreasing temperature, attributed to decreasing dissociation of the N – H protons. The temperature-dependent shift is more pronounced for the N – H resonance, than the $H^{3,5}$ and

H^4 (Figure 20). At higher temperatures, the downfield H^1/H^2 resonance is broader, and the vicinal coupling of the two upfield resonances larger, showing a $J^3 = 2.12$ Hz for the $H^{3,5}$ and H^4 resonances at 7.72 ppm and 6.30 ppm, respectively, at 328 K.

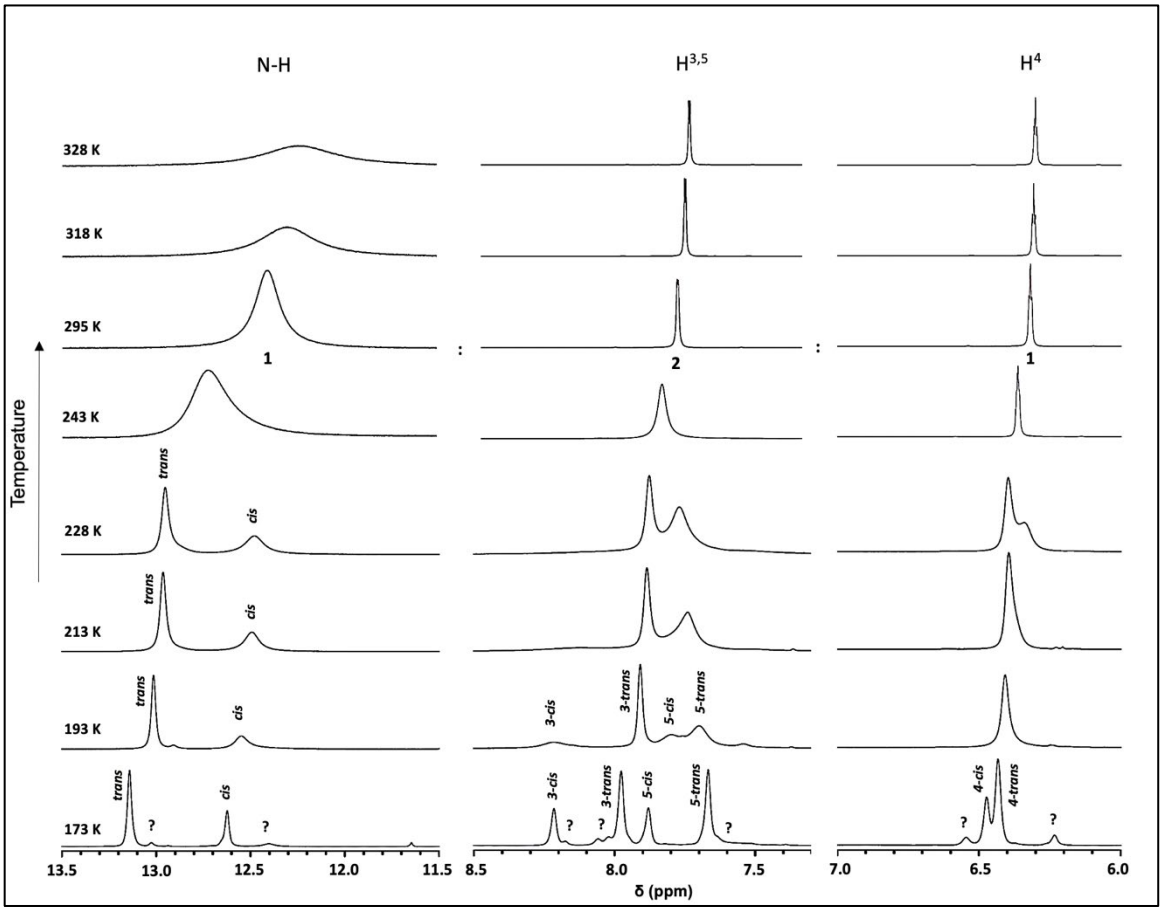

Figure 18. Variable temperature ^{1}H NMR of complex **1** in THF-d_8 at 400 MHz.

Upon cooling to 243 K, only broadening of the three resonances and loss of vicinal coupling (at the upfield resonance) is observed. However, further cooling causes de-coalescence: at 228 K and 213 K, quenching of the *cis*/*trans* exchange is apparent, as each of the three resonances are split into two with integrated areas of 1:2 (proton assignments in Scheme 7). At 193 K, the H^3 and H^5 resonances are differentiated for both *cis* and *trans* pyrazoles, while the *cis*-H^4 resonance crosses under the *trans*-H^4.

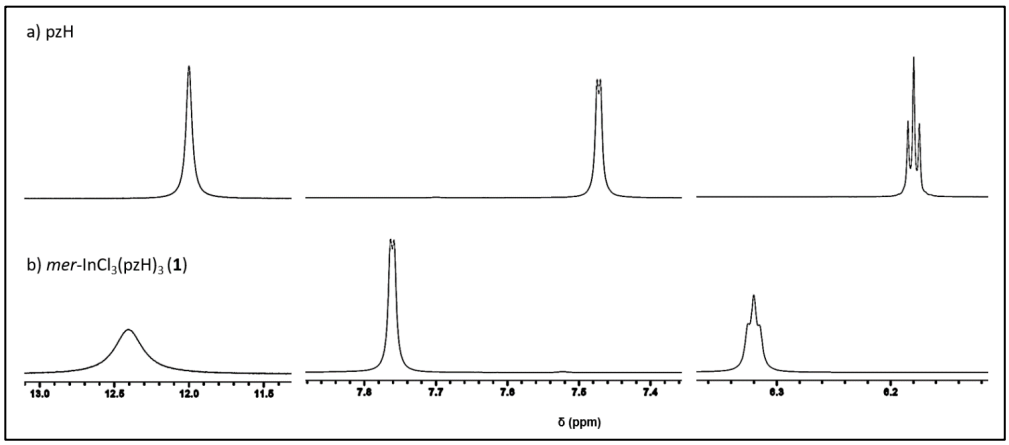

Figure 19. ^{1}H NMR of (a) free pyrazole and (b) complex **1** in THF-d_8 at ambient temperature, 400 MHz.

Finally, at our minimum reachable temperature of 173 K, all resonances become sharper, while several smaller unassigned peaks, accounting for approximately 16.5% of total intensity, appear in the vicinity of all resonances (Figure 21). Because none of these weak peaks coincide with those of free pyrazole in the same solvent and temperature, the possibility of pyrazole dissociation has been excluded. Therefore, these weaker peaks can be tentatively assigned to the freezing of rotations around In – N bonds, or equilibria between protonated/deprotonated species, or association/dissociation of chlorides.

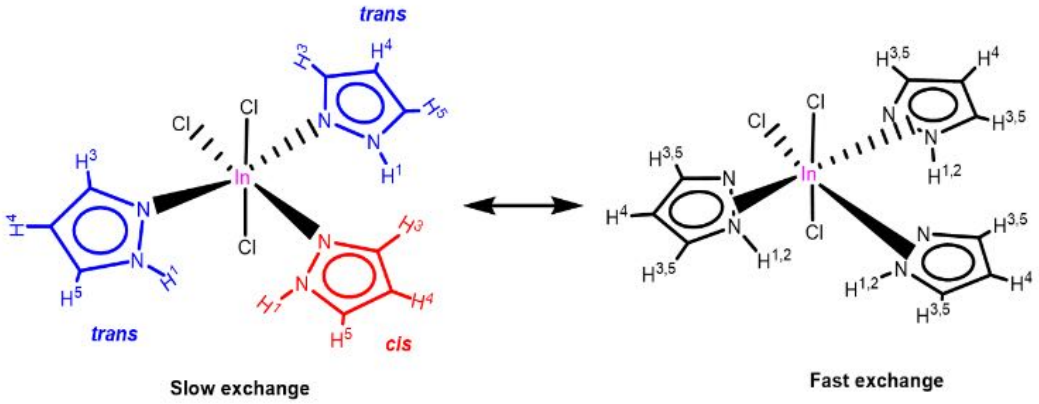

Scheme 7. Static and dynamic behavior of **1**, as determined by VT-^{1}H NMR, with proton labeling scheme.

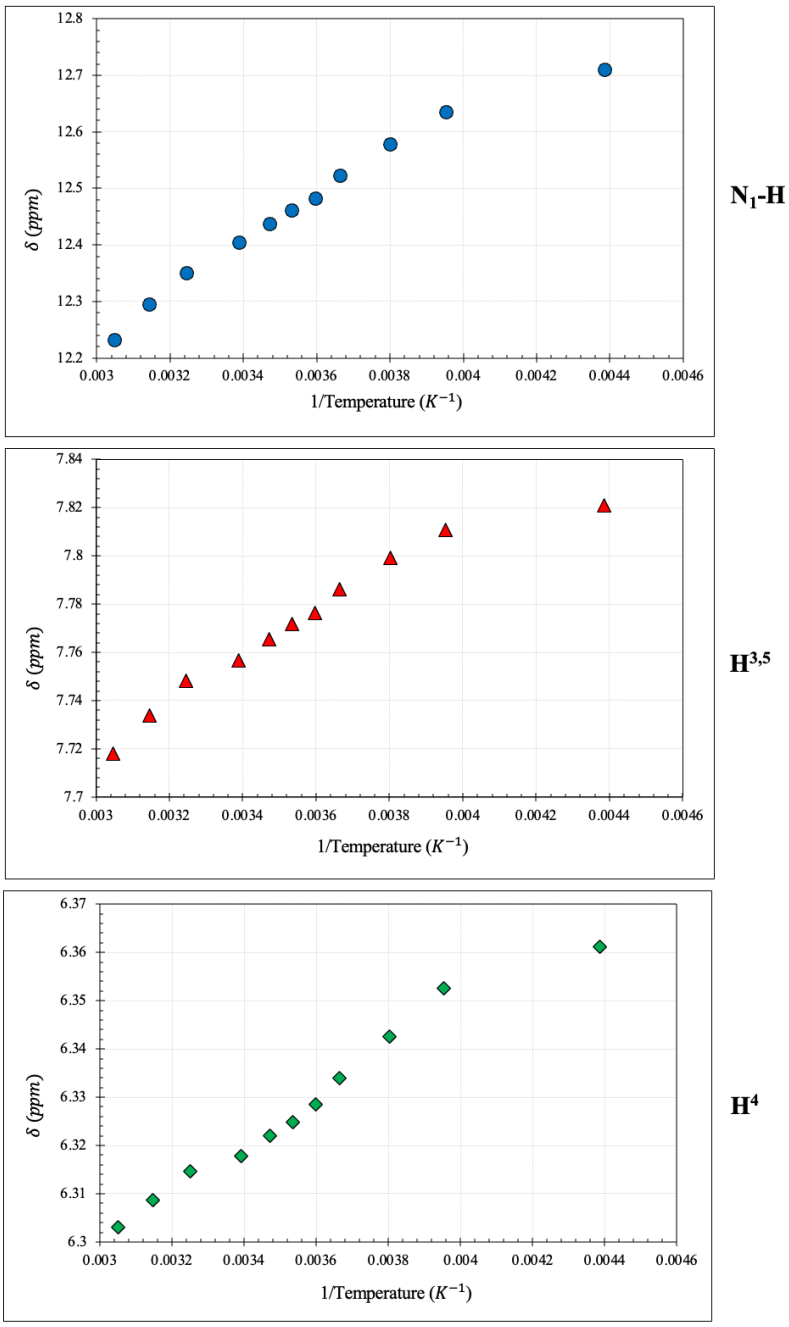

Figure 20. Temperature dependence of H chemical shifts of complex **1**.

The exclusion of pyrazole dissociation leaves only two possible mechanisms for the *cis/trans* exchange: chloride dissociation and Berry pseudorotation of the five-coordinate complex, or a cog-wheel type rotational isomerization. Whereas the N^1/N^2 tautomerization of pyrazoles is well established in the literature (Scheme 6),[45,60–62]

examples of internal rotational isomerization of *mer*- complexes with no bulky ligands are scarce. The simultaneous operation of several dynamic processes in solutions of **1** prevent the determination of kinetic and thermodynamic parameters based on the above variable temperature experiments. Attempts to calculate approximate parameters led to rate constants in the order of 10^2 s^{-1} and negative apparent activation energies, which are meaningless in this case, but provide an additional indication for the occurrence of multiple simultaneous processes.

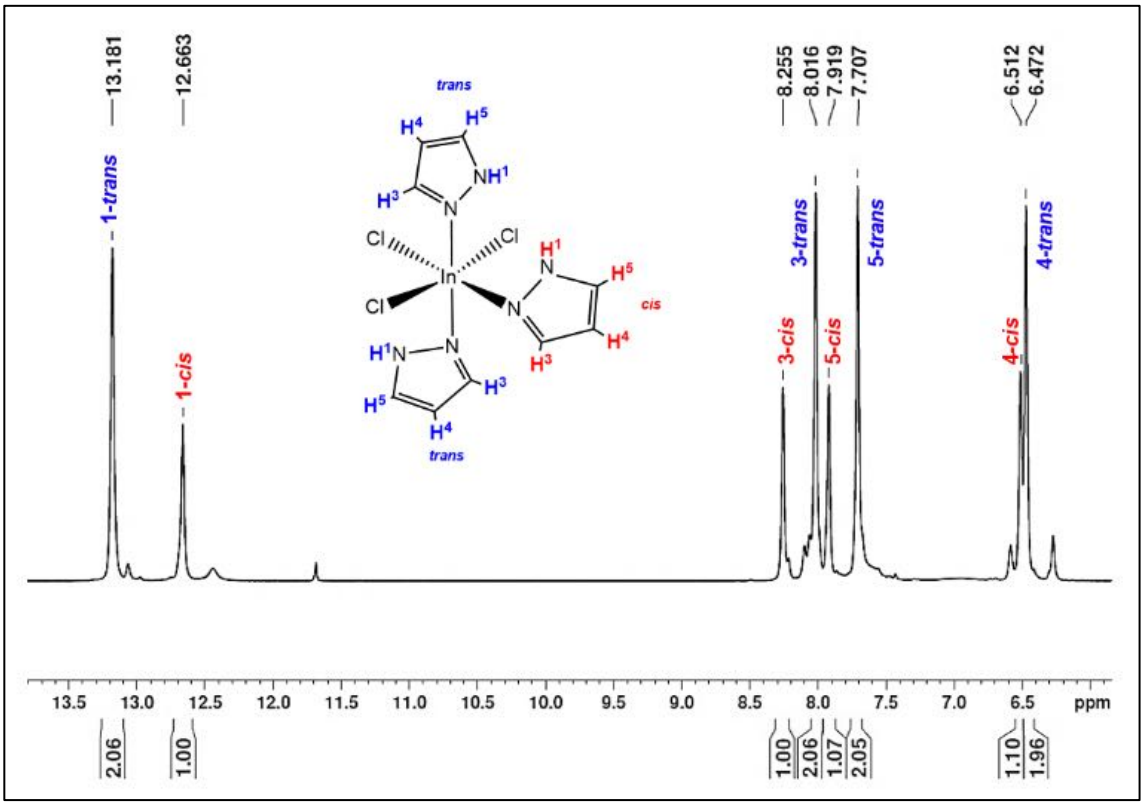

Figure 21. ^{1}H NMR of complex **1** at 173 K in THF-d_8 400 MHz.

Similar behavior is observed by variable temperature ^{1}H-NMR for complex **2**, involving 4-Cl-pzH (Figure A6). However, at the lowest temperature reached, its spectrum is still not fully resolved, consequently, it can only be concluded that the isomerization and exchange rates of **2** are even faster than those of **1**.

Similarly, the ^{1}H NMR at ambient temperature of complexes **7** and **8** showed a single set of three resonances, assigned to N – H, $H^{3,5}$, and CH_3 protons, even though the solution was a mixture of both complexes, meaning there is a dynamic equilibrium in solution that make the *mer*- and *trans*- complexes indistinguishable. The assignment of the three resonances was based on their 1:2:3 integrated area intensities. Variable-temperature solution ^{1}H-NMR study of **7** and **8** was performed in the temperature range of 296 K to 202 K in THF-d_8 (Figure 22).

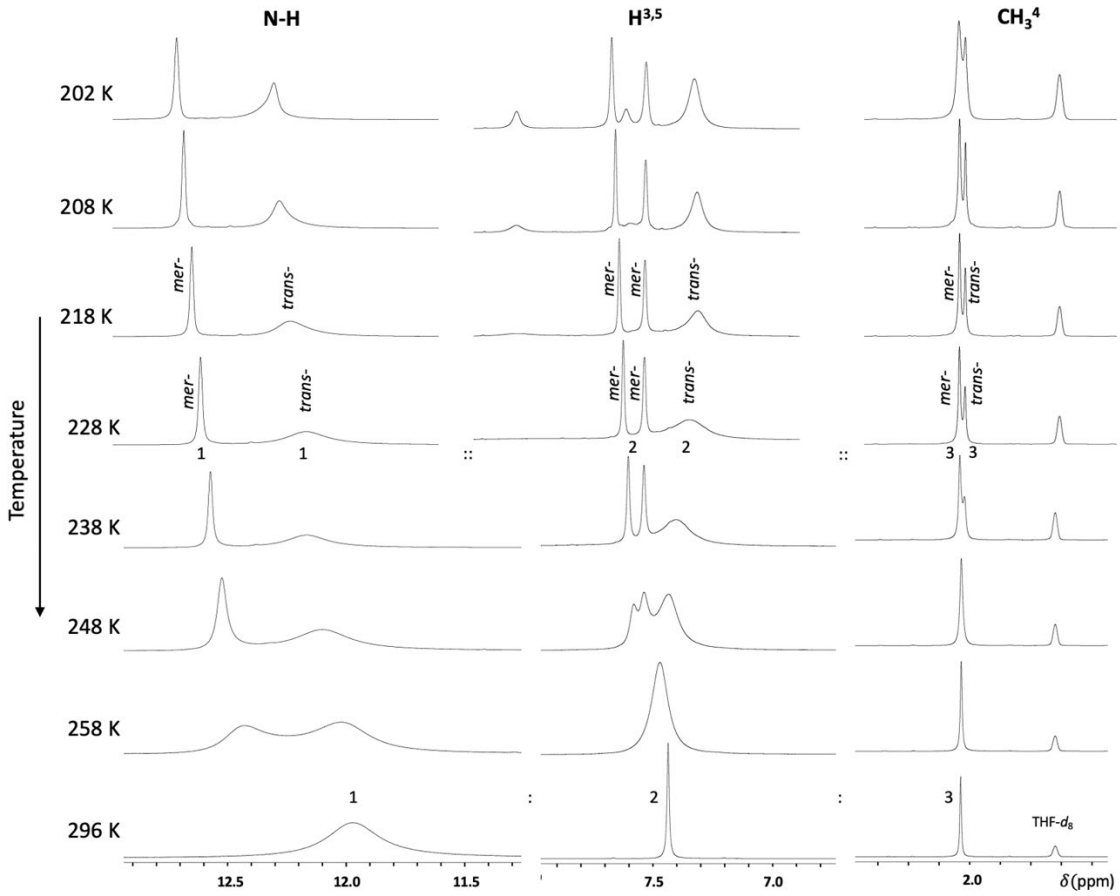

Figure 22. VT ^{1}H NMR of **7** and **8** mixture in THF-d_8 at 400 MHz.

Same dynamic behavior was observed for **7** as for complex **1**. Upon cooling to 258 K, de-coalescence and splitting of the N – H peak, along with broadening of the $H^{3,5}$

resonance, were observed, with the latter splitting into three resonances at 248 K. At 228 K, the *trans*- and *mer*- complexes set of resonances can be assigned based on their integrated intensities, each set showing a 1:2:3 integration, and at 228 K showing 2:3 integration of the **7** to **8** complexes, respectively. At 198 K, the $H^{3,5}$ resonance of the *trans*-complex shows further splitting, however no assignments can be made at this point. At the lowest reached temperature of 202 K, the spectrum is not fully resolved. Compared to previous VT-^{1}H-NMR studies of **1** and **2**, the mixture of **7** and **8** show faster isomerization and exchange rates. None of the peaks coincide with free 4-Me-pzH in the same solvent and temperature (Figure A7), therefore the possibility of the 4-Me-pzH dissociation has been excluded as well.

2.2.4. Powder X-ray diffraction of In(III) monomers

Complexes **7** and **8** co-crystallize as indistinguishable colorless crystals that were in a dynamic equilibrium in solution, therefore individual characterization other than by single crystal X-ray diffraction was not possible. Elemental analysis of the batch confirmed there was a mixture of 27% of **7** and 73% of **8**. Powder X-ray diffraction (PXRD) patterns were collected for the bulk reaction product and compared to the simulated PXRD patterns of the obtained crystal structures of **7** and **8**, which confirmed that the bulk reaction product was indeed a mixture (Figure 23).

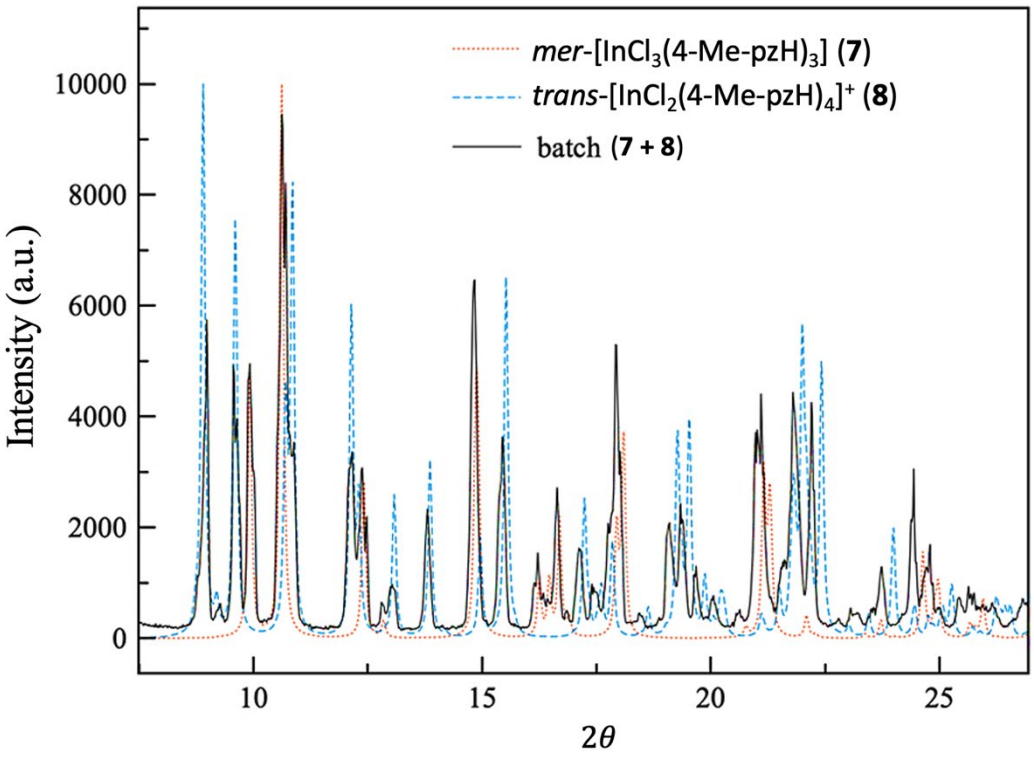

Figure 23. PXRD of bulk reaction product of **7** and **8** fitted to the simulated PXRD patterns of the SCXRD of the respective complexes.

2.3. Base addition to mononuclear In(III) complexes

Deprotonation of pyrazole ligands creates a pyrazolato anion able to form higher nuclearity complexes. In(III) monomers with formula *mer*-[$InCl_3(pz^*H)_3$] were reacted with bases like triethylamine or piperidine in various solvents to deprotonate the coordinating pyrazole and obtain higher nuclearity complexes.

2.3.1. In(III) hexanuclear pyrazolato complexes

Complexes **9 – 11** with general formula $(pipH)_3[In_6Cl_6(\mu_3\text{-}OH_{0.5})_2(\mu\text{-}OH)_6(\mu\text{-}pz^*)_6]$ were synthesized according to the reaction pathway shown in Scheme 4. The synthesis of the hexanuclear indium clusters is achieved only in acetone or tetrahydrofuran solvents, using piperidine (pip) or triethylamine (Et_3N) as the base, in open reaction vessels

(atmospheric humidity is the required water source). However, addition of water, or prolonged exposure to humidity, triggers the precipitation of indium oxide. Only hexanuclear complexes with 4-R-substituted pyrazoles are obtained.

2.3.2. Crystallographic description of In(III) hexanuclear complexes

Crystals of the trianionic hexanuclear complexes with three different pyrazole ligands and piperidinium (pipH) counter ions have been obtained. Crystallographic data collection, refinement parameters, and selected metric parameters are summarized in Table 9 and 6, respectively. Each indium center is 6-coordinate, in a pseudo-octahedral *fac*-O_3N_2Cl environment, with two μ-4-R-pyrazolato bridges (where R = H, Cl, Ph), two μ-OH, one (μ_3-$OH_{0.5}$), and one terminal chloride. Complex **11** crystallized with six-fold symmetry, while the presence of interstitial solvent molecules lowered the solid-state symmetry of **9** and **10**.

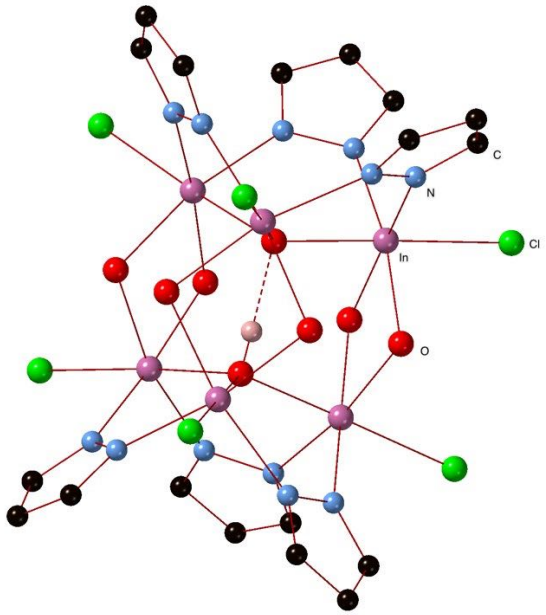

Figure 24. Ball-and-stick representation of $[In_6Cl_6(\mu_3\text{-}OH_{0.5})_2(\mu\text{-}OH)_6(\mu\text{-}pz)_6]^{3-}$ (**9**). Counterions and solvents are omitted for simplicity. H atoms are not shown, except for μ_3-OH.

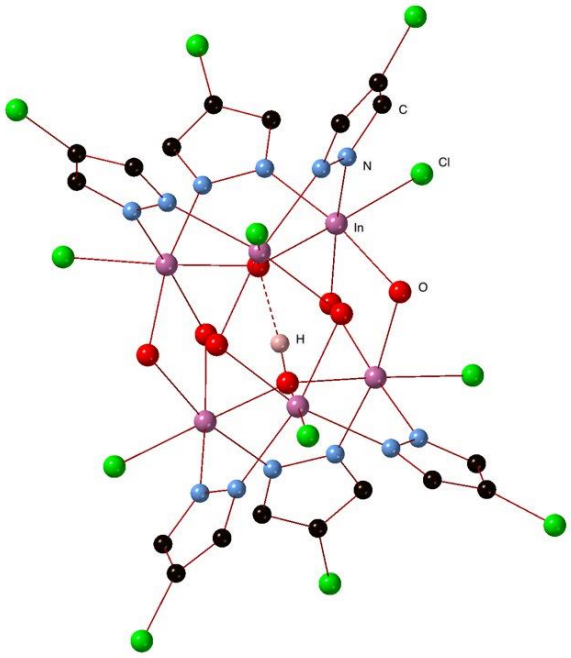

Figure 25. Ball-and-stick representation of $[[In_6Cl_6(\mu_3\text{-}OH_{0.5})_2(\mu\text{-}OH)_6(\mu\text{-}4\text{-}Cl\text{-}pz)_6]^{3-}$ (**10**). Counterions and solvents are omitted for simplicity. H atoms are not shown, except for μ_3-OH.

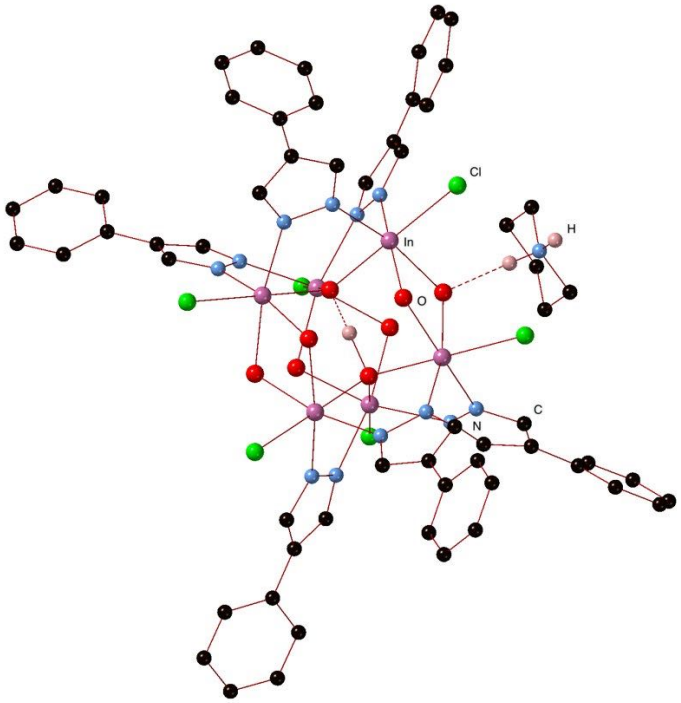

Figure 26. Ball-and-stick representation of $[In_6Cl_6(\mu_3\text{-}OH_{0.5})_2(\mu\text{-}OH)_6(\mu\text{-}4\text{-}Ph\text{-}pz)_6]^{3-}$ (**11**). Only one of three pipH cations is shown for simplicity. H atoms are not shown, except for μ_3-OH and pip-NH_2.

The six indium centers of **9 – 11** form a trigonal prism, the trigonal faces consisting of inward-pointing pyramidal [$In_3(\mu_3\text{-}OH_{0.5})$] moieties, strongly H – bonded to each other (O···O, 2.527 – 2.558 Å). The structures of the hexanuclear D_{3h}-symmetric anions are completed by six additional μ-OH groups, bridging the In_3 faces parallel to the axis of the prism and forming intramolecular H – bonds (O ··· O, 2.719– 2.778 Å), in addition to H – bonds to the pipH cations (N ··· O, 2.693 – 2.852 Å). The In – Cl, In – N, In – O bond lengths (Table 6) are unexceptional. Only four structurally characterized complexes containing In – (μ_3-O), In – (μ-OH), and In – (μ-O) motifs have been reported, to date (Scheme 8).[63–66] In these four literature complexes, the reported In – (μ_3-O) and In – (μ-OH) bond distances of 2.03 Å - 2.04 Å and 2.10 Å - 2.18 Å, respectively, are shorter in comparison to the In – (μ_3-$OH_{0.5}$) and In – (μ-OH) of **9 – 11**. In contrast, the In – N(triazole) bond distances of 2.27 Å - 2.38 Å in the literature examples, are longer than the In – N(pyrazolato) bonds in **9 – 11**. The In ··· In intramolecular distances for the (μ-OH) and (μ-pz) bridged centres are between 3.36 – 3.42 Å and 3.67 – 3.74 Å, respectively (Table 6).

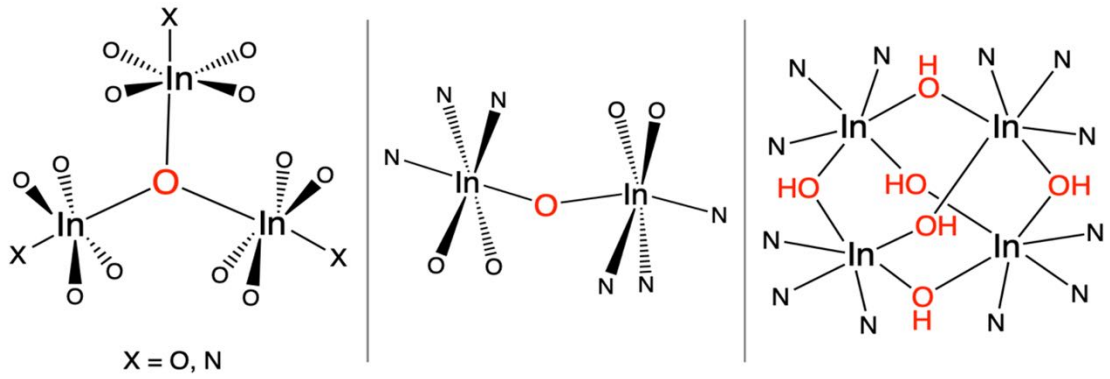

Scheme 8. Examples of known In-(μ_3-O), In-(μ-O), and In-(μ-OH) motifs.

Table 6. Selected bond lengths (Å) for **9 – 11**.

	Compounds		
Interatomic distances	**9**	**10**	**11**
In ··· In[a]	3.36(1) – 3.40(4)	3.36(8) – 3.42(9)	3.41(6)
In ··· In[b]	3.67(2) – 3.74(6)	3.70(4) – 3.73(1)	3.70(5)
In – Cl	2.46(7) – 2.50(1)	2.45(6) – 2.46(3)	2.46(1)
In – (μ-OH)	2.16(7) – 2.20(7)	2.17(9) – 2.21(1)	2.19(6) – 2.20(7)
In – N	2.19(7) – 2.23 (7)	2.21(8) – 2.23(5)	2.21(5) – 2.22(1)
In – (μ_3-$OH_{0.5}$)	2.16(9) – 2.20(5)	2.18(2) – 2.20(3)	2.18(5)

[a](μ-OH) bridged; [b](μ-pz) bridged

2.3.3. Nuclear magnetic resonance of In(III) hexanuclear complexes

Compounds **9 – 11** were crystallized by evaporation of the acetone or THF reaction mixtures. However, once crystallized, **9 – 11** are insoluble in the same or other organic solvents, except DMF and DMSO (only **11**). The ^{1}H-NMR spectrum of **9** DMF-d_7 (Figure 27) shows one set of resonances and no H^1/H^2 resonance downfield, confirming that all six pyrazoles are bridging and equivalent. A doublet at 8.06 ppm and a triplet at 6.15 ppm correspond to $H^{3,5}$ and H^4, respectively. Additional resonances between 13 and 14 ppm disappear when the solution is spiked with D_2O and are attributed to the μ-OH and piperidinium N – H. The piperidinium counterions show a set of two resonances, a broad triplet at 3.00 ppm (4H) and overlapping peaks at 1.42 ppm (6H). The corresponding $H^{3,5}$ and $pipH^+$ resonances of **10** appear at 8.09, 3.07 and 1.54 ppm, respectively (Figure 28). Unfortunately, the ^{1}H-NMR spectra of **11** in DMSO show more resonances than expected for the crystallographically determined molecular structures, indicating that DMSO is a non-innocent solvent, leading to coordination changes, or decomposition of **11**.

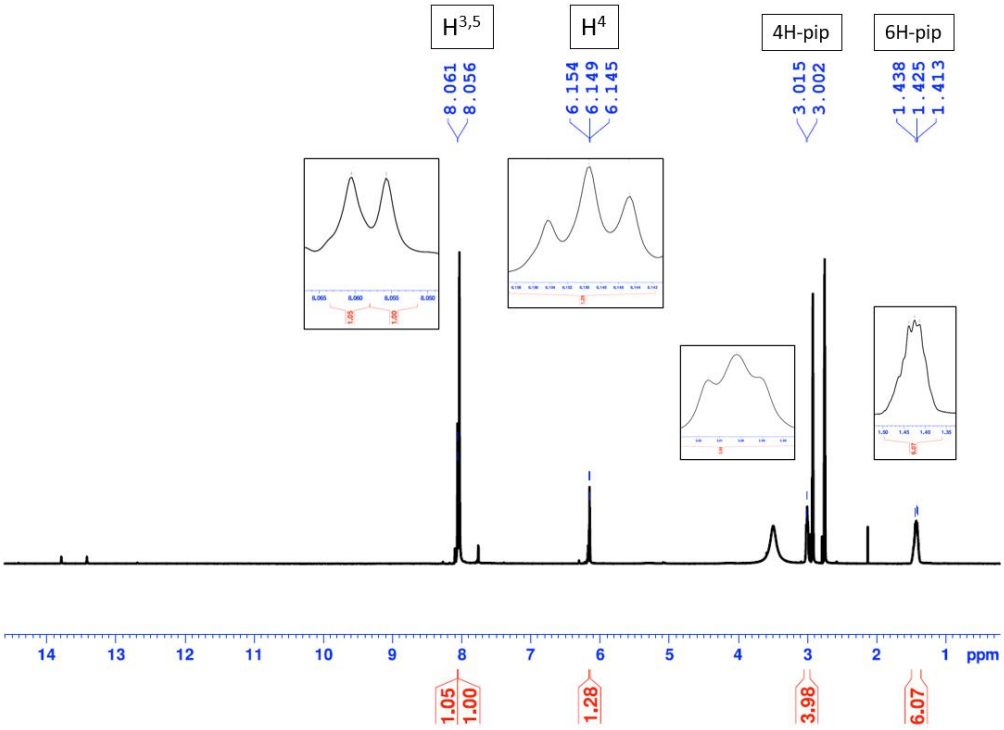

Figure 27. ^{1}H NMR of $(pipH)_3[In_6Cl_6(\mu_3\text{-}OH_{0.5})_2(\mu\text{-}OH)_6(\mu\text{-}pz)_6]$ (**9**) in DMF-d_7 at 400 MHz and ambient temperature.

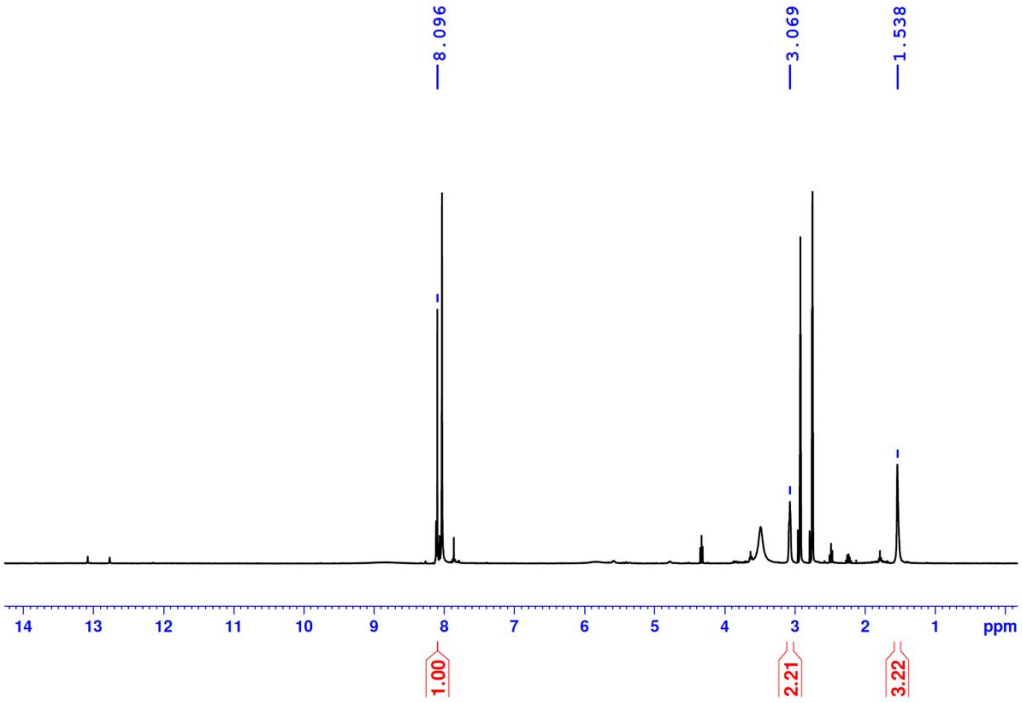

Figure 28. ^{1}H NMR of $(pipH)_3[In_6Cl_6(\mu_3\text{-}OH_{0.5})_2(\mu\text{-}OH)_6(\mu\text{-}4\text{-}Cl\text{-}pz)_6]$ (**10**) in DMF-d_7 at 400 MHz and ambient temperature.

2.3.4. Thermogravimetric analysis of In(III) hexanuclear complexes

To investigate the thermal stability of the In(III) hexanuclear complexes, thermogravimetric analysis (TGA) was carried out in the temperature range 25 – 450ºC under a flow of argon with a heating rate of 10ºC/min (Figure 29). For **11**, the weight loss of 12% in the temperature range 25 – 160ºC (calc. 11.998%) corresponds to the removal of the three piperidinium cations, after which there is no obvious loss until 360ºC, with only about 20% of the weight remaining at 435ºC, corresponding to some In_xO_y phase. The indium phase diagram calculated based on thermodynamic models and melting points agrees with the presence of In_2O_3 in the temperature range of 200 – 800ºC and under 60% oxygen atomic weight.[67] Indeed, a remaining In_2O_3 phase would be 16.35% of **11** after the weight loss observed from 360 – 435ºC.

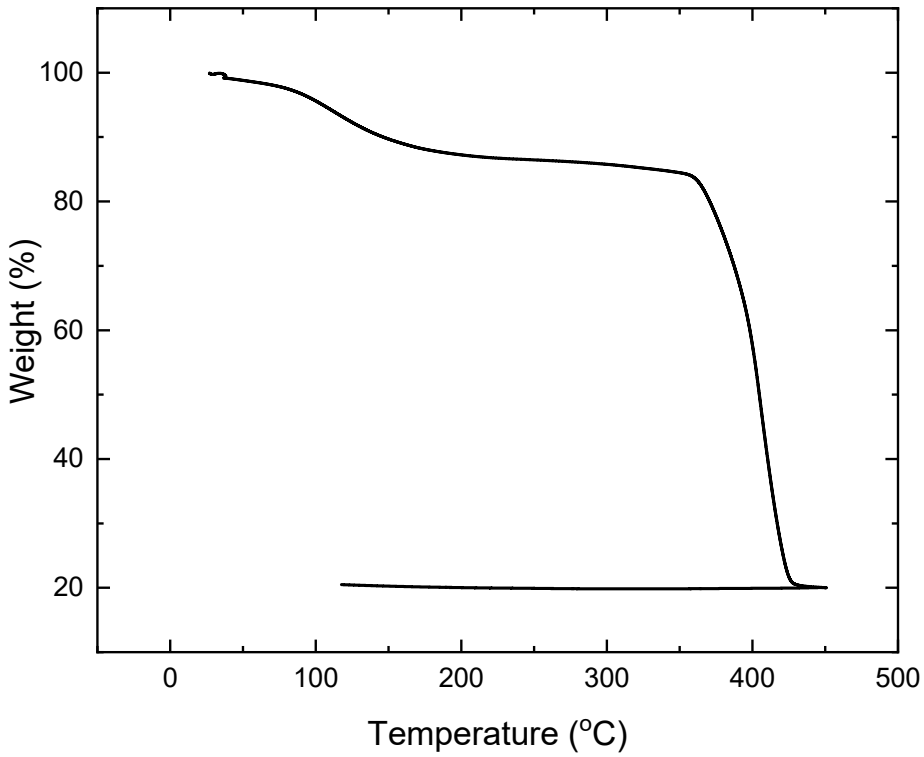

Figure 29. TGA curves of **11**.

2.4. In(III) supramolecular chemistry

Metal-based supramolecular chemistry and coordination chemistry is a field of great interest due to their potential applications, which include luminescence properties, catalytic activities, and medicinal chemistry. Polydentate ligands, such as carboxylic acids, are widely used in the field of structural design. Carboxylates have been broadly compared with the pyrazolato, as they share some structural similarities, even though they differ in rigidity (Scheme 9) and reactivity.[68]

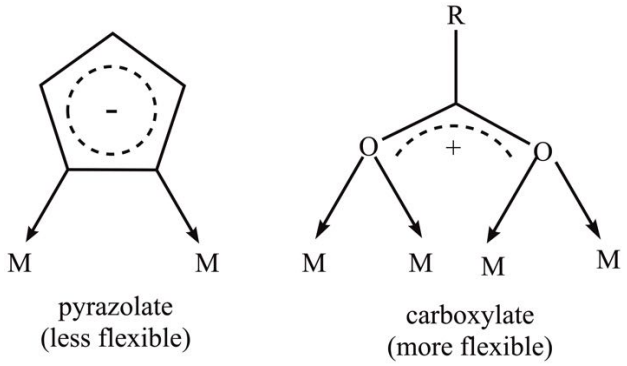

Scheme 9. Structural comparison between pyrazolato and carboxylate bridging modes.

Indium(III)-coordination polymers based on *C*$_3$-symmetric tricarboxylate ligand of general formula {[In(L)(H$_2$O)](DMF)}$_n$, where H$_3$L = 2,4,6-tris[(4-carboxyphenoxy)methyl]-1,3,5-trimethylbenzene have been previously reported showing anticancer activity on neuroblastoma.[69] The structure determination from single crystal data showed that the compound crystallized in a monoclinic space group *C*2/c and reveals a 3D two-fold interpenetrated net.[69]

In(III) centers are also commonly used as coordination nodes to construct highly stable coordination polymers with high oxidation state metal ions. Coordination polymers are a class of solid crystalline materials with a wide range of applications including

catalysis, sensing, and proton conduction. High proton conductivity materials are desirable for fuel cells that can be employed as efficient and clean energy devices. One of the commonly applied strategies to design highly proton conducting coordination polymers is the use of imidazoles as proton carriers together with specific ligands with acidic functional groups.[70] Imidazoles and pyrazoles have similar electronic structures (Figure 30).[71] To date, only a limited number of coordination polymers and metal organic frameworks (MOFs) have been reported from indium halides with N-donor ligands.[72,73]

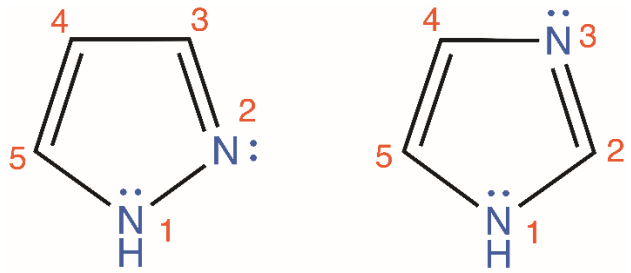

Figure 30. Electronic structure comparison between pyrazolato and imidazole ligands.

2.4.1. In(III) pyrazolato oligomers or polymers

Reaction of *mer*-[$InCl_3(pz^*H)_3$] with three equivalents of piperidine in CH_2Cl_2 (Scheme 4) leads to deprotonation of the pyrazoles to form a polymer or oligomer of general formula $[In(pz^*)_3]_n$ (**12 – 15**) and pipHCl. The resulting microcrystalline precipitate can be washed with ethanol to remove the salts. Complexes **12 – 15** are insoluble in all solvents, to the best of our knowledge.

2.4.2. Powder X-ray diffraction of In(III) oligomers or polymers

PXRD data was collected for **12** and **13** (Figures 31 and 32) but were not sufficiently defined – no measurable high-angle data -- for a Rietveld refinement.

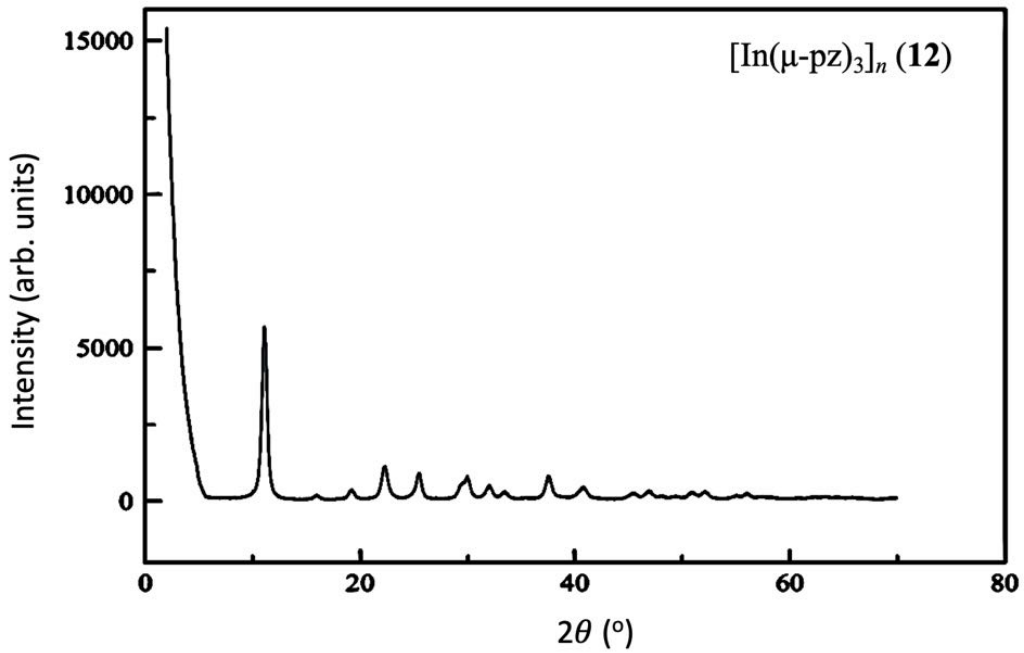

Figure 31. PXRD pattern for [In(μ-pz)$_3$]$_n$ (**12**).

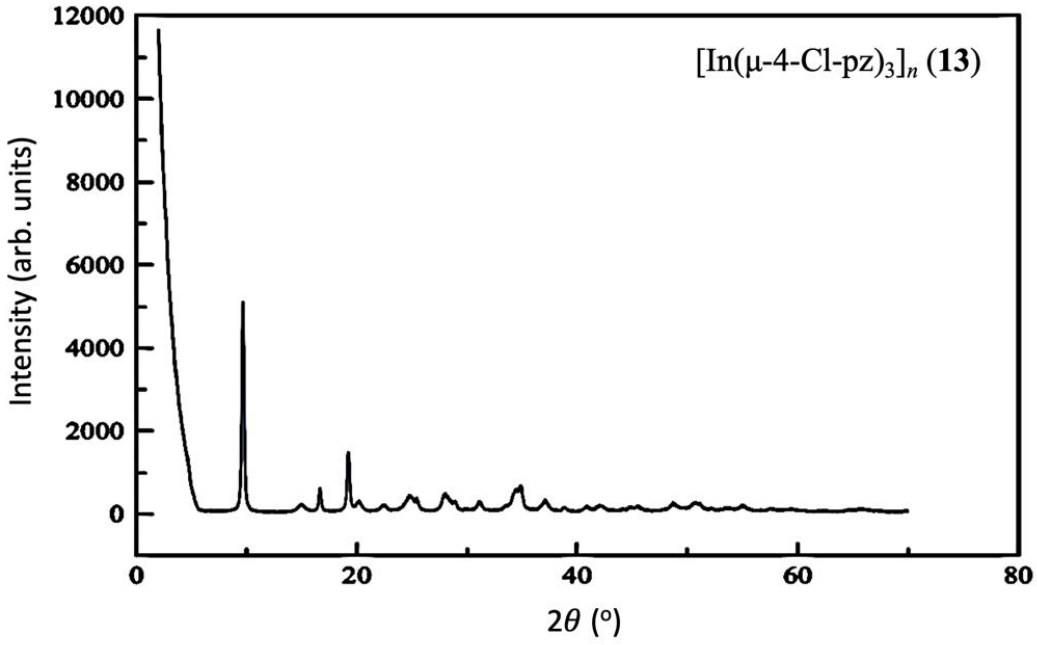

Figure 32. PXRD pattern for [In(μ-4-Cl-pz)$_3$]$_n$ (**13**).

2.4.3. **Photophysical properties of In(III) oligomers or polymers** (by Jonathan Cedeño and Jaroslava Miksovska).

Photophysical properties of In(III) oligomers or polymers were investigated by collaborators.. The solid-state emission spectra of **12 – 15** normalized to 1.0 at the maximum wavelength are shown in Figure 33. All compounds exhibit green-fluorescent emission maxima in the vicinity of 550 nm, except for **15**, which shows a second red emission at 676 nm. All samples also have an additional lower intensity emission band at 500 nm. The compounds investigated display two distinct fluorescence lifetimes with a shorter lifetime, τ_1, in the range of 0.2 ns to 1.0 ns and additional longer lifetime, τ_2, in the ranges of 5.0 ns – 6.5 ns (Table 7). Pyrazoles are not known as a strongly luminescent species and indeed previous studies reported no emission from some of the pyrazoles employed here, even at cryogenic temperatures.[74] However, pyrazolato bridges promote d^{10} – d^{10} metallophilic interactions resulting in interesting photophysical properties.[75–77] Therefore, the luminescent properties of **12 – 15** are tentatively attributed to the In-centres. Luminescent indium compounds have been reported previously by others, but with shorter lifetimes -- 0.20 ns < τ < 1.1.ns -- in solution than the ones reported here.[78] The longer lifetimes of **12 – 15** are attributed to the increased rigidity of their polymeric structure compared to molecular emitters.

Table 7. Photophysical Data for **12 – 15**.

Compound	τ_1 (ns)	τ_2 (ns)	λ_{max} (nm)
12	0.21	5.39	560
13[a]	-	-	556
14	0.30	5.88	554
15	1.07	6.36	676

[a]Because of intense scattering, lifetimes could not be determined accurately.
The errors represent 10% of the reported lifetime values.

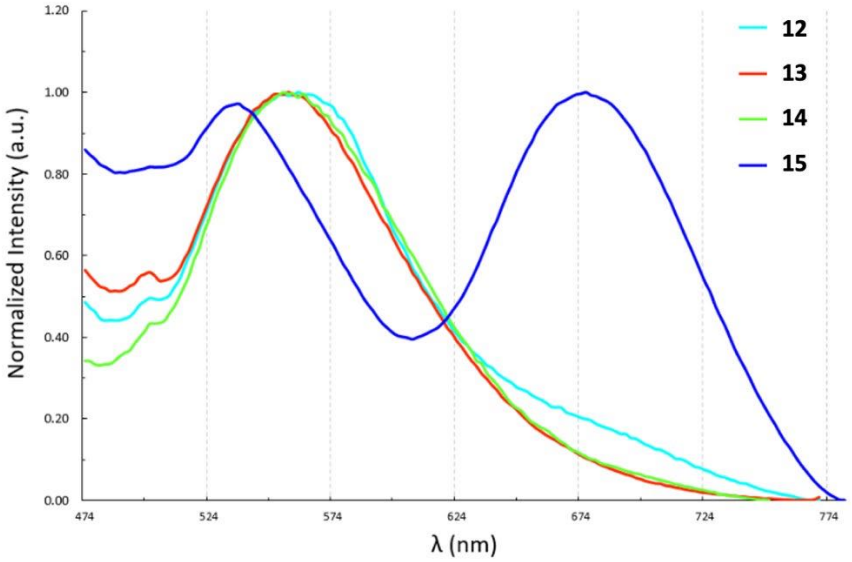

Figure 33. Solid-state emission spectra of **12 – 15**.

2.4.4. Infrared spectroscopy of In(III) monomers, hexanuclear complexes, and polymers

Comparison of the 4000 - 400 cm^{-1} FTIR spectra of **1**, **9** and **12** to that of free pzH (Figure 34) support the formulation of *mer*-[$InCl_3(pzH)_3$] (**1**), $(pipH)_3[In_6Cl_6(\mu_3\text{-}OH_{0.5})(\mu\text{-}OH)_6(\mu\text{-}pz)_6]$ (**9**), and $[In(pz)_3]_n$ (**12**). Some peaks are conserved throughout the series of free pzH and corresponding mononuclear, hexanuclear and polymeric compounds (Figure A8 - Figure A12). Both free pzH and **1**, show sharp bands at 3122 cm^{-1} and 3313 cm^{-1}, respectively, corresponding to N – H stretching vibrations; the N – H stretch for **1** is at higher wavenumbers due to the absence of strong intermolecular hydrogen bonding interactions present for solid state pyrazole ligands.[62,79–82] The absence of N – H stretching vibrations in **9** and **12** is consistent with the bidentate, bridging coordination mode of all pyrazole ligands. The most significant differences among the spectra of **1**, **9** and **12** are the following: The ring stretching mode of **1** at 1354 cm^{-1} shift to 1377 cm^{-1} in **12** and 1373

cm^{-1} in **9**; The ring breathing mode of **1** at 1120 cm^{-1} shifts to 1157 cm^{-1} in **12**; The in-plane C – H stretching mode of **1** and **9** at 1045 cm^{-1} shifts to 1051 cm^{-1} in **12**, while the out-of-C – H bending mode of **1** at 773 cm^{-1} shifts to 756 cm^{-1} in **9** and 758 cm^{-1} in **12**. Finally, the pyrazole ring deformation at 596 cm^{-1} of **1**, shifts to 625 cm^{-1} in **9** and 623 cm^{-1} in **12**. These assignments are based on previously published vibrational spectroscopic studies of pyrazoles. [83–86]

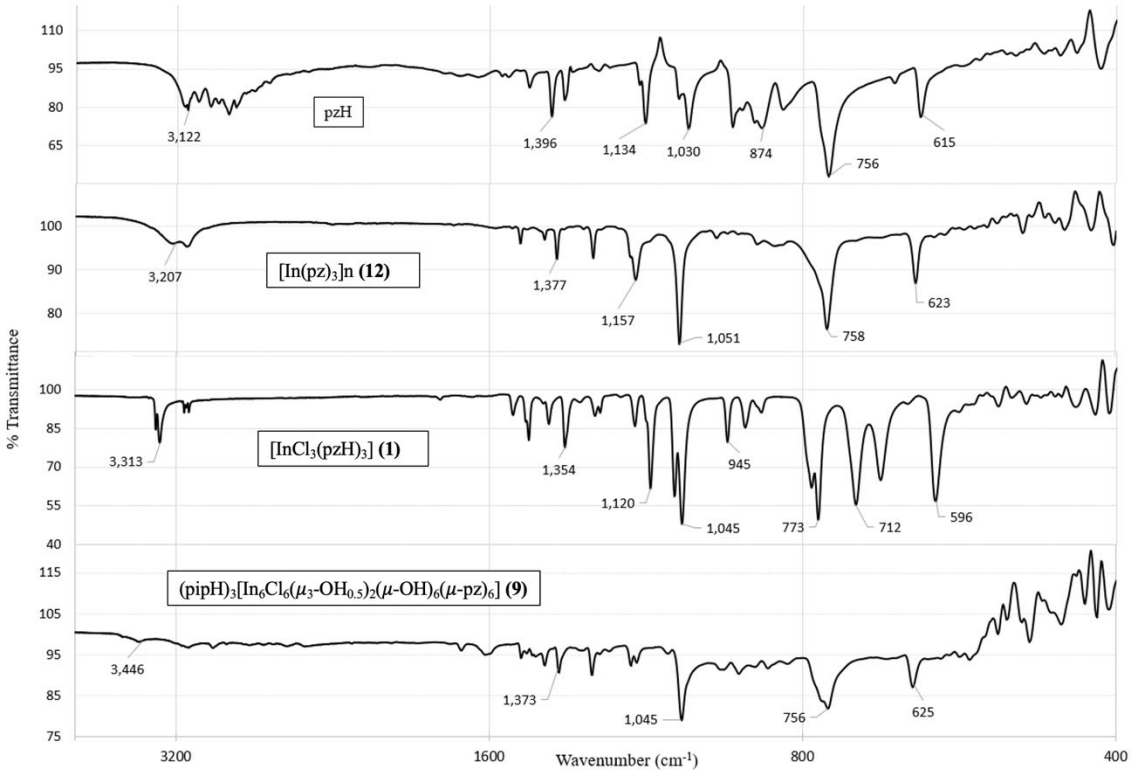

Figure 34. FTIR spectra of pzH (top), $[In(pz)_3]_n$ (**12**), *mer*-$[InCl_3(pzH)_3]$ (**1**), $(pipH)_3[In_6Cl_6(\mu_3\text{-}OH_{0.5})_2(\mu\text{-}OH)_6(\mu\text{-}pz)_6]$ (**9**).

2.5. Antibacterial studies of In(III) pyrazole/pyrazolato monomers and hexanuclear complexes (by Dr. Masafumi Yoshinaga; manuscript submitted for publication)

Indium-based drugs and prodrugs have been known for a long time. The ^{111}In radioisotope is used in radiopharmaceuticals and cell labeling,[87,88] while Auger electrons

emitted by ^{111}In are employed in palliative cancer treatment.[89] It has also been shown that non-radioactive In_2O_3 nanopowders show significant antibacterial activity towards both gram-negative (*E. coli*) and gram-positive (*S. aureus*) bacteria, being more effective against the latter.[90] In(III) complexes of organic ligands find pharmacological applications, because of their antimicrobial and antiproliferative properties.[91–93] For example, indium(III) thiosemicarbazones have shown antimicrobial activity, as well as potent cytotoxic effects against human solid tumors and leukemia cell lines, showing increased activity compared the free thiosemicarbazones.[94] Yet, indium remains an underexplored element in biomedicine, which has prompted us to ask our collaborators to investigate the antibacterial properties of the indium(III) pyrazolato complexes we have synthesized – the first of this family of compounds.

The antibacterial properties of our indium(III) pyrazolato complexes were examined by collaborators from Florida International University Herbert Wertheim College of Medicine. Using several representative pathogenic bacteria strains (*E. faecium* (vancomycin-resistant), *S. aureus* (methicillin-resistant and vancomycin-intermediate), *K. pneumoniae* (carbapenem-resistant), *P. aeruginosa* (carbapenem-resistant), *E. coli* (carbapenem-resistant) and *E. cloacae* (carbapenem-resistant)) (Figure 35 A-F), strains were cultured in cation-adjusted Mueller Hinton II broth in the absence or presence of the indicated indium (III) compounds and growth was estimated from the A_{600nm} after 16 h (A-F) or the bioluminescence after 7 days (G). They all belong to the ESKAPE pathogens, a group of six nosocomial pathogens that often have high levels of resistance and frequently "escape" the effects of antibacterial drugs, leading to high morbidity and mortality:[95] *E. faecium, S. aureus, K. pneumoniae, Acinetobacter baumannii, P. aeruginosa,* and

Enterobacter species. The ESKAPE pathogens are included in the WHO (World Health Organization) global priority pathogens list issued to guide and promote research and development of new antibiotics.[96] Our indium(III) compounds had little effect on the Gram-positive pathogens *E. faecium* and *S. aureus.* In contrast, the Gram-negative pathogens *K. pneumoniae, P. aeruginosa, E. cloacae* and *E. coli* were relatively more sensitive to the indium(III) drugs. Interestingly, *P. aeruginosa* was especially sensitive, and all the tested indium(III) compounds (100 μM) inhibited the growth by approximately 80 to 95% with *mer*-[$InCl_3$(4-Ph-pzH)$_3$] (**6**) being the most effective. *mer*-[$InCl_3$(4-Ph-pzH)$_3$] (**6**) was also the most effective drug against the other Gram-negative strains, although the effect was much lower. Previously, a 1:1 complex of indium(III) with the MCC 1,4,8,11-tetraazacyclotetradecane-1,4,8,11-tetra-acetic acid (TETA) was shown to be effective against the Gram-positive *Mycobacterium tuberculosis*,[92] the etiologic agent of human tuberculosis, a leading cause of death due to an infectious disease. Thus, we also examined the potential of our indium(III) compounds as antituberculosis agents using a related pathogenic strain, *M. bovis* BCG, an attenuated etiologic agent of bovine tuberculosis (Figure 35 G). *M. bovis* BCG is also sensitive to all the drugs, yet the effect was relatively moderate compared to *P. aeruginosa*. As with the case of *P. aeruginosa*, *mer*-[$InCl_3$(4-Ph-pzH)$_3$] (**6**) was especially effective, inhibiting the growth of *M. bovis* BGC about 85%. Either pzH or 4-Ph-pzH has little or no effect on most of the tested pathogens (Figure 36), suggesting that the indium moiety plays an essential role to exhibit the antibiotic activity. The results demonstrate that our indium(III) pyrazole and pyrazolato complexes have a potential to lead to development of novel classes of antipseudomonal and antituberculosis drugs.

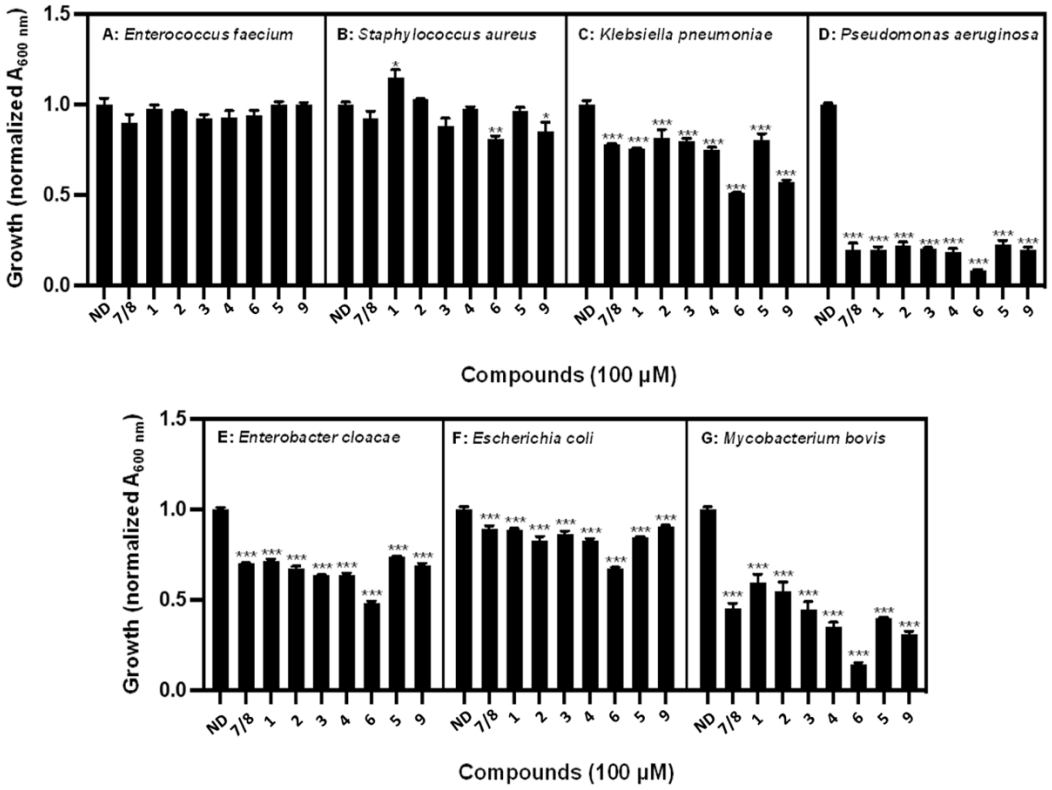

Figure 35. Antibiotic activity of indium (III) pyrazolato complexes; **ND**, no drug. Viabilities were normalized to the relative viability of untreated control samples (1.0). Data are the mean ± standard error (n = 3). One-way ANOVA tests were used to calculate the *p* values (*$p < 0.03$; **$p < 0.001$; ***$p < 0.0001$).

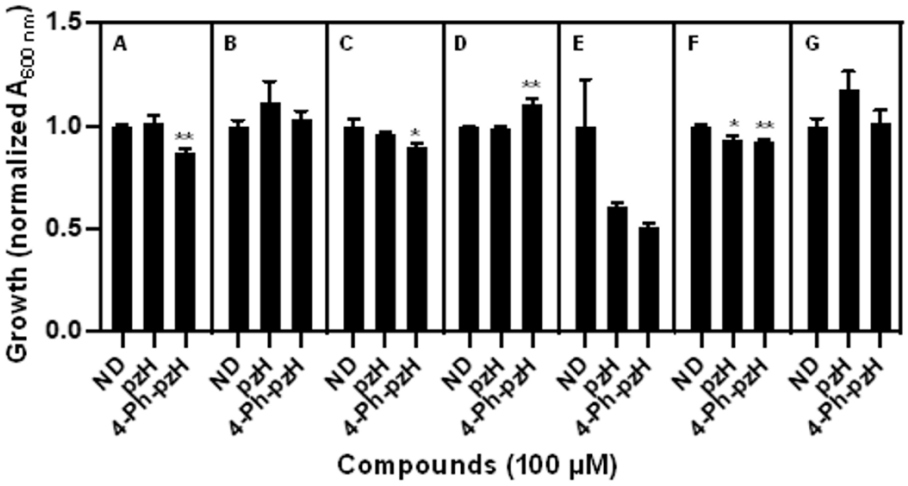

Figure 36. Antibiotic activity of monodentate pyrazoles. Viabilities were normalized to the relative viability of untreated control samples (1.0). Data are the mean ± standard error (n = 3). One-way ANOVA tests were used to calculate the *p* values (*$p < 0.03$; **$p < 0.001$; ***$p < 0.0001$). A, *E. faecium*; B, *S. aureus*; C, *K. pneumoniae*; D, *P. aeruginosa*; E, *E. cloacae*; F, *E. coli*; G, *M. bovis*.

2.6. Conclusions

The coordination chemistry of indium(III) with pyrazole ligands has been studied for the first time. As expected for a d^{10} metal center, the new family of *mer*-$[InCl_3(pz^*H)_3]$ complexes are fluxional in solution: variable temperature ^{1}H-NMR revealed the complex interplay of simultaneous coordinative flexibility, dissociation, and tautomerization processes. The co-crystallization of *mer*- and *trans*- complexes also shows similar variable temperature behavior, and upon cooling the *mer*- and *trans*- complexes can be uniquely identified. Similarly, to previously studied *mer*-$[MCl_3(pz^*H)_3]$, M = Fe and Ru, the new indium pyrazole complexes are useful starting materials for the synthesis of polynuclear and polymeric species. The hexanuclear $[In_6Cl_6(\mu_3\text{-}OH_{0.5})_2(\mu\text{-}OH)_6(\mu\text{-}pz^*)_6]^{3-}$ complexes represent a new motif of indium(III)-oxo/hydroxo species and the first example of complex showing both μ-OH and μ_3-O(H) bridges. As the crystalline faces of indium oxide, containing μ-O(H) groups, have been shown to be efficient photocatalysts for the reduction of CO_2,[97] future research will investigate whether the hexanuclear complexes described here might show similar properties in solution. The emission spectra of polymeric $[In(\mu\text{-}pz^*)_3]_n$ complexes vary depending on pyrazole substitution; their maxima are red-shifted, and their lifetimes are longer compared to monomeric indium luminophores in the literature.[78]

Antibacterial activity of representative examples of the new In(III) complexes described here was investigated. The results show the versatility of indium(III) complexes and demonstrate that development of novel classes of antipseudomonal and antituberculosis drugs using indium(III) species is promising.

2.7. Experimental section

2.7.1. Materials and physical measurements

Reagent grade chemicals were obtained from commercial sources and used as received. All solvents were stored over 4 Å molecular sieves. Anhydrous $InCl_3$ was stored and weighed in a glove box compartment under argon. Elemental analyses (C, H, N) were performed by Galbraith Laboratories, Inc. at Knoxville, TN.

2.7.1.1. Fluorescence emission

Fluorescence emission spectra were collected using a PC1 fluorometer (ISS, Champaign IL). The crystalline samples were placed between two quartz slides positioned in the sample holder at ~ 45° with respect to the excitation light. The samples were excited using CW output from a 378 nm laser diode. Fluorescence lifetimes were measured in frequency mode on a ChronosFD fluorometer (ISS, Champaign, IL) using 378 nm excitation light and the emission was collected using a 400 nm long pass filter (Andover Corp, Salem NH) placed in the emission light pathway. 1,4-bis(5-phenyloxazol-2-yl) benzene dissolved in 100% ethanol was used as a lifetime reference (τ =1.35 ns). For the lifetime measurements, the crystalline samples were suspended in glycerol and placed in a 5 mm x 1.0 cm quartz cuvette. Due to the higher scattering of the crystalline samples, only phase shift data were used to determine fluorescence lifetimes. The data were analyzed using a double exponential decay in VINCI software (ISS, Champaign IL).

2.7.1.2. Assay of antibiotic activity

Solution of each indium(III) compound was freshly prepared in DMSO at 10 mM and the concentration was confirmed by inductively coupled plasma mass spectrometry (NexION 1000; PerkinElmer, Waltham, MA, USA) using a linear calibration curve based

on measurement of indium standard solutions in the range of 1–20 ppb prepared from Multi-element Solution 2 (SPEX CertiPrep, Metuchen, NJ). The indium(III) solutions were immediately used for the assays within the same day. *Enterococcus faecium* (vancomycin-resistant, ATCC #: BAA-472), *Staphylococcus aureus* Mu50 (methicillin-resistant and vancomycin-intermediate, 700699), *Klebsiella pneumoniae* (carbapenem-resistant, BAA-2342), *Escherichia coli* (carbapenem-resistant, BAA-2340), *Enterobacter cloacae* (carbapenem-resistant, BAA-2341), *Mycobacterium bovis* BCG (ATCC19274) were obtained from American Type Culture Collection (ATCC, Manassas, VA). *Pseudomonas aeruginosa* DK-2 (carbapenem-resistant) was a gift from Professor Søren Molin, Technical University of Denmark. All used pathogens are Risk Group 2 bacterial agents, and they were appropriately handled in Biosafety Level 2 containment setting. Middlebrook 7H9 broth (Difco Laboratories Inc., Detroit, MI, USA) supplemented with 5 g bovine serum albumin, 2 g dextrose, 0.85 g NaCl and 0.05% tween 80 (Fisher Scientific International Inc., Pittsburg, PA, USA) was used to culture *M. bovis* BCG. An autoluminescent strain of *M. bovis* BGC was prepared using pMV306hsp+LuxG13,[98] the plasmid containing the entire bacterial luciferase (*lux*) operon (addgene, Watertown, MA) for rapid analysis of viability in culture and macrophages as described.[99] The autoluminescent mycobacterial cells were inoculated at a density of 5.0×10^5 CFU/ml in 96-well flat bottom opaque white plates (Corning Inc., Corning, NY) in triplicate and cultured in the presence or absence of indicated indium(III) compounds (100 μM, final concentration) in an incubator humidified at 37 °C under 5% CO_2 for 7 days. Viable cells in each culture were determined by bioluminescence intensity using a microplate reader (SYNERGY neo2, BioTek, Winooski, VT). All other bacterial strains were inoculated at a cell density of an A_{600nm} of 0.04−0.06

in cation-adjusted Mueller Hinton II broth (17.5 g l^{-1} casein acid hydrolysate, 3.0 g l^{-1} beef extract, 1.5 g l^{-1} starch, 0.5 mM $MgSO_4$ and 0.5 mM $CaCl_2$) in 96-well clear flat bottom plates in triplicate and incubated with or without indicated indium(III) compounds (100 μM) in an incubator humidified at 37 °C for 16 h. The A_{600nm} was determined using SYNERGY neo2 microplate reader to compare the antibiotic activity of each compound. Growth controls containing no drug (1% DMSO) were prepared for each assay. Sterile controls without bacteria were prepared for each condition. One-way ANOVA tests were used to calculate the *p* values of drug effects on bacteria.

2.7.2. Instrumentation

^1H NMR spectra were recorded on a 400 MHz Bruker Avance NMR spectrometer and were referenced using the residual solvent proton resonances. Infrared spectra (FT-IR) were recorded on an Agilent Avance Cary-660 FT-IR spectrometer at room temperature.

2.7.3. Synthesis and characterization

2.7.3.1. Synthesis of *mer*-[$InCl_3(pzH)_3$] (1)

To a suspension of $InCl_3$ (109.3 mg, 0.494 mmol) in 3 mL CH_2Cl_2 was added pzH (105.2 mg, 1.545 mmol) under stirring and allowed to react for 12 h. A white precipitate was collected by suction filtration and washed with Et_2O. The white powder was allowed to dry in a desiccator for 24 h. The powder was then recrystallized from MeOH by layering over CH_2Cl_2. Colorless, prism-like, X-ray grade crystals were obtained after two days and washed with Et_2O. Yield: 81.91%. Analysis for $C_9H_{12}Cl_3InN_6$ (425.41 g mol^{-1}), Calcd: C, 25.41; H, 2.84; N, 19.75; Found: C, 25.63; H, 2.60; N, 19.90. FTIR (cm^{-1}, solid): 3343(m), 3313(s), 3104(w), 1781(w), 1519(m), 1465(m), 1403(m), 1354(m), 1253(w), 1160(m), 1120(vs), 1062(s), 1045(vs), 945(m), 908(w), 773(vs), 712(vs), 675(vs), 595(vs). ^1H NMR

(400 MHz, THF-d_8, 295 K), δ (ppm): 12.40 (s, 1H, H^1-pz), 7.76 (d, J^3 = 1.82 Hz, 2H, $H^{3,5}$-pz), 6.32 (t, J^3 = 1.96 Hz, 1H, H^4-pz).

2.7.3.2. Synthesis of *mer*-[$InCl_3$(4-Cl-pzH)$_3$] (2)

To a suspension of anhydrous $InCl_3$ (446.78 mg, 2.02 mmol) in 10 mL CH_2Cl_2 was added 4-Cl-pzH (617.1 mg, 6.02 mmol) under stirring and allowed to react for 12 h. A white precipitate was collected by filtration in a Büchner funnel and washed with Et_2O. The white powder was left to dry in a desiccator for 24 h, then dissolved in 2 mL MeCN. A 1mL solution was layered on CH_2Cl_2 and X-ray grade, colorless crystals were obtained after three days, and washed thoroughly with Et_2O. Yield: 73.8%. Analysis for $C_9H_9Cl_6InN_6 \cdot 0.6CH_3CN$ (528.52 g mol^{-1}), Calcd: C, 22.14; H, 1.97; N, 16.71; Found: C, 21.87; H, 1.73; N, 17.03. FTIR (cm^{-1}, solid): 3325(w), 3280(m), 3126(w), 2087(w), 1695(w), 1531(w), 1462(m), 1390(s), 1342(s), 1259(m), 1194(s), 1115(vs), 1047(vs), 962(vs), 951(vs), 868(m), 850(vs), 706(m), 681(vs), 596(vs). ^{1}H NMR (400 MHz, THF-d_8, 297 K), δ (ppm): 12.30 (s, 1H, H^1-pz), 7.63 (s, 2H, $H^{3,5}$-pz).

2.7.3.3. Synthesis of *mer*-[$InCl_3$(4-Br-pzH)$_3$] (3)

4-Br-pzH (221.6 mg, 1.508 mmol) was added to a suspension of $InCl_3$ (110.81 mg, 0.501 mmol) in 3 mL CH_2Cl_2 under stirring and allowed to react for 12 h. A white powder was collected by suction filtration and washed with Et_2O. The powder was left to dry in a desiccator for 24 h, then dissolved in 2 mL MeCN. 1 mL solution was layered on CH_2Cl_2. X-ray grade, colorless crystals formed after three days. Crystals were washed thoroughly with Et_2O. Yield: 86.54%. Analysis for $C_9H_9Cl_3Br_3InN_6$ (662.10 g mol^{-1}), Calcd: C, 16.33; H, 1.37; N, 12.69; Found: C, 16.42; H, 1.33; N, 12.76. FTIR (cm^{-1}, solid): 3532(w), 3322(m), 3289(m), 3133(w), 2096(w), 1631(w), 1521(m), 1467(s), 1388(s), 1336(m),

1259(s), 1193(m), 1122(vs), 1049(vs), 948(vs), 862(vs), 827(m), 677(vs), 588(s). ^{1}H NMR (400 MHz, $(CD_3)_2SO$, 296 K) δ (ppm): 13.19 (s, 1H, H^1-pz), 7.97 (s, 1H, $H^{3,5}$-pz), 7.56 (d, J^3 = 1.22 Hz, 1H, $H^{3,5}$-pz).

2.7.3.4. Synthesis of *mer*-[$InCl_3$(4-I-pzH)$_3$] (4)

To a suspension of anhydrous $InCl_3$ (441.66 mg, 2.00 mmol) in 10 mL CH_2Cl_2 was added 4-I-pzH (1.160 g, 5.98 mmol) under stirring and allowed to react for 12 h. A white precipitate was collected by filtration in a Büchner funnel and washed with Et_2O. The white powder was left to dry in a desiccator for 24 h. The powder was then dissolved in MeCN and layered on CH_2Cl_2 for recrystallization. Colorless, prism-like, X-ray grade crystals were obtained after four days and washed with Et_2O. Yield: 82.12%. Analysis for $C_9H_9Cl_3I_3InN_6$ (803.10 g mol^{-1}), Calcd: C, 13.46; H, 1.13; N, 10.46; Found: C, 13.52; H, 1.07; N, 10.11. FTIR (cm^{-1}, solid): 3334(m), 3295(m), 3124(w), 2082(w), 1683(w), 1459(m), 1378(m), 1332(m), 1249(m), 1124(s), 1049(vs), 939(vs), 862(s), 833(m), 675(vs), 590(vs). ^{1}H NMR (400 MHz, $(CD_3)_2SO$, 296 K) δ (ppm): 13.17 (s, 1H, H^1-pz), 7.93 (s, 1H, H^5-pz), 7.55 (s, 1H, H^3-pz).

2.7.3.5. Synthesis of *mer*-[$InCl_3$(3,5-Me_2-pzH)$_3$·H_2O] (5)

3,5-Me_2-pzH (28.7 mg, 0.3 mmol) were added to a suspension of $InCl_3$ (23.01 mg, 0.104 mmol) in 3 mL CH_2Cl_2 under stirring and allowed to react for 24 h. A white precipitate was collected by filtration in a Büchner funnel and washed with Et_2O. The white powder was left to dry in a desiccator for 24 h. The powder was then dissolved in MeOH, and the solvent was allowed to slowly evaporate. Colorless X-ray grade crystals were obtained in two days and washed with Et_2O. Yield: 42.1% Analysis for $C_{15}H_{26}Cl_3InN_6O$ (527.59 g mol^{-1}), Calcd: C, 34.15; H, 4.97; N, 15.93; Found: C, 35.01; H, 4.38; N, 16.12.

IR ($\tilde{\nu}_{max}$, cm^{-1}): 3548(w), 3338(m), 3029(w), 1569(s), 1467(m), 1407(m), 1279(s), 1168(s), 1157(s), 1035(s), 1022(s), 804(s), 651(vs), 551(s). ^{1}H NMR (400 MHz, $(CD_3)_2SO$, 298 K) δ (ppm): 11.99 (s, 1H, H^1-pz), 5.73 (s, 1H, H^4-pz), 2.11 (s, 6H, $CH_3^{3,5}$-pz).

2.7.3.6. Synthesis of *mer*-[$InCl_3$(4-Ph-pzH)$_3$] (6)

To a suspension of $InCl_3$ (111.63 mg, 0.5 mmol) in 3 mL of CH_2Cl_2 were added 4-Ph-pzH (216.25 mg, 1.5 mmol) under stirring and allowed to react for 24 h. A clear solution was obtained, and solvent was removed under reduced pressure. The resulting white precipitate was washed with EtOH and Et_2O and allowed to dry in a desiccator for 24h. Yield: 60.55%. Analysis for $C_{27}H_{24}Cl_3InN_6 \cdot 0.4Et_2O$ (653.71 g mol^{-1}), Calcd: C, 50.27; H, 4.13; N, 12.30; Found: C, 50.63; H, 3.96; N, 12.64. FTIR (cm^{-1}, solid): 3290(m), 3116(w), 1603(m), 1568(w), 1483(w), 1450(w), 1385(m), 1362(m), 1280(w), 1134(s), 1114(m), 1045(vs), 958(m), 945(s), 874(m), 765(vs), 758(vs), 688(vs), 679(vs), 598(m). ^{1}H NMR (400 MHz, $(CD_3)_2SO$, 297 K) δ (ppm): 12.93 (s, 1H, H^1-pz), 8.18 (s, 1H, $H^{3,5}$-pz), 7.91 (s, 1H, $H^{3,5}$-pz), 7.60 (dd, J^3 = 8.32 Hz, J^4 = 1.20 Hz, 2H, H^{ortho}-Ph-pz), 7.34 (tt, J^3 = 7.76 Hz, J^4 = 1.84 Hz, 2H, H^{meta}-Ph,pz), 7.17 (tt, J^3 = 7.38 Hz, J^4 = 1.20 Hz, 1H, H^{para}-Ph-pz).

2.7.3.7. Synthesis of *mer*-[$InCl_3$(4-Me-pzH)$_3$] (7) and *trans*-[$InCl_2$(4-Me-pzH)$_4$]Cl·(4-Me-pzH)$_2$·(H_2O) (8)

4-Me-pzH (165µL, 2.00 mmol) was added to a mixture of $InCl_3$ (110.23 mg, 0.497 mmol) in 3 mL MeOH under stirring and allowed to react for 12 hours. A clear solution was obtained and was left for slow evaporation of the solvent. An oily product was observed after evaporation of methanol, to which diethyl ether was added and left in the fridge. After two months, a white powder was obtained, and diethyl ether had evaporated. The powder was redissolved in MeOH, and the solution was placed in the refrigerator at

275 K for crystallization. X-ray grade, colorless crystals of **7** formed after one month. In a separate recrystallization effort, Et_2O was added into the MeOH prior to placing the solution in the refrigerator at 275 K. X-ray quality crystals of **8** grew after 2 days. Analysis for $C_{12}H_{18}Cl_3InN_6$ (467.49 g mol^{-1}, **7**), Calcd: C, 30.83; H, 3.88; N, 17.98 and for $C_{24}H_{38}Cl_3InN_{12}O$ (731.81 g mol^{-1}, **8**), Calcd: C, 40.27; H, 5.35; N, 23.48 Found: C, 37.10; H, 4.94; N, 21.43, corresponding to 27% *cis* (**7**) and 73% *trans* (**8**). ^{1}H NMR (400 MHz, THF-d_8, 296.9 K) δ (ppm): 11.99 (s, 1H, H^1-pz), 7.42 (s, 2H, $H^{3,5}$-pz), 2.03 (s, 3H, CH_3-pz).

2.7.3.8. Synthesis of $(pipH)_3[In_6Cl_6(\mu_3\text{-}OH_{0.5})_2(\mu\text{-}OH)_6(\mu\text{-}pz)_6]$ (9)

To a solution of piperidine (pip) (148.3 μL, 1.5 mmol) in 5 mL acetone, *mer*-$[InCl_3(pzH)_3]$ (213.8 mg, 0.5 mmol) was added under stirring and allowed to react for 48 h. Some precipitate formed. The solvent was allowed to evaporate, and crystals were obtained and washed with EtOH and Et_2O. Yield: 22%. Analysis for $C_{33}H_{61}Cl_6In_6N_{15}O_8$ (1697.56 g mol^{-1}), Calcd: C, 23.35; H, 3.62; N, 12.38; Found: C, 23.50; H, 3.61; N, 12.09. ^{1}H NMR (400 MHz, DMF-d_7, 297 K) δ (ppm): 8.06 (d, J^3 = 1.95 Hz, 2H, $H^{3,5}$-pz), 6.15 (t, J^3 = 1.90 Hz, 1H, H^4-pz), 3.00 (t, J^3 = 5.84 Hz, 4H -$pipH^+$), 1.42 (m, 6H - $pipH^+$). FTIR (cm^{-1}, solid): 3463(w), 3106(w), 2944(w), 2713(m), 2497(w), 1699(w), 1612(w), 1444(w), 1369(m), 1272(m), 1168(m), 1045(s), 917(w), 752(s), 624(m).

2.7.3.9. Synthesis of $(pipH)_3[In_6Cl_6(\mu_3\text{-}OH_{0.5})_2(\mu\text{-}OH)_6(\mu\text{-}4\text{-}Cl\text{-}pz)_6]$ (10)

Compound **10** was prepared in the same manner as for **9**, using *mer*-$[InCl_3(4\text{-}Cl\text{-}pzH)_3]$ (264 mg, 0.5 mmol) and pip (148.3 μL, 1.5 mmol) in 5 mL acetone. The solvent was allowed to evaporate, and the crystals obtained after 2 days were washed with EtOH and Et_2O. Yield: 14%. ^{1}H NMR (400 MHz, DMF-d_7, 297 K) δ (ppm): 8.07 (s, 2H, $H^{3,5}$-

pz), 6.15, 3.05 (t, J^3 = 5.84 Hz, 4H -pipH$^+$), 1.52 (m, 6H - pipH$^+$). FTIR (cm^{-1}, solid): 3390(w), 2947(m), 2750(m), 2524(w), 1591(w), 1458(m), 1387(m), 1300(s), 1197(m), 1153(w), 1049(vs), 989(m), 968(vs), 945(w), 835(s), 613(vs), 555(m).

2.7.3.10. Synthesis of (pipH)$_3$[In$_6$Cl$_6$(μ$_3$-OH$_{0.5}$)$_2$(μ-OH)$_6$(μ-4-Ph-pz)$_6$] (11)

Compound **11** was prepared in the same manner as for **9**, using *mer*-[InCl$_3$(4-Ph-pzH)$_3$] (30.5 mg, 0.047 mmol) and pip (13.6 μL, 0.137 mmol) in 2 mL acetone. The solvent was removed under reduced pressure, the precipitate was washed with EtOH and Et$_2$O and allowed to dry in a desiccator for 24 h. Crystals were obtained from slow evaporation of acetone after 3 days. Yield: 95%. FTIR (cm^{-1}, solid): 3448(w), 3191(w), 2965(w), 1953(w), 1701(m), 1604(m), 1560(m), 1456(m), 1377(m), 1353(s), 1246(s), 1161(s), 1111(s), 1045(vs), 999(m), 951(s), 904(m), 868(s), 766(vs), 756(vs), 700(vs), 683(vs), 659(s). After washing of crystals with wet solvents, formation of small amounts of In$_2$O$_3$ was observed. Analysis for (pipH)$_3$[In$_6$Cl$_6$(μ$_3$-OH$_{0.5}$)(μ-OH)$_6$(μ-Ph-pz)$_6$](In$_2$O$_3$), Calcd: C, 34.08; H, 3.52; N, 8.64; Found: C, 34.29; H, 4.06; N, 8.30.

2.7.3.11. Synthesis of [In(μ-pz)$_3$]$_n$ (12)

To a suspension of **1** (42.3 mg, 0.1 mmol) in 3 mL CH_2Cl_2, pip (29.7 μL, 0.3 mmol) were added under stirring and allowed to react for 24 h. A white precipitate was obtained and isolated by suction filtration. The precipitate was washed with EtOH and Et$_2$O and allowed to dry in a desiccator for 24 h. Yield: 83%. Analysis for $C_9H_9InN_6$ (316.03 g mol^{-1}), Calcd for **12**•0.5CH_2Cl_2: C, 31.83; H, 3.37; N, 23.43; Found: C, 31.97; H, 2.56; N, 23.46. FTIR (cm^{-1}, solid): 3226(m), 3118(m), 1492(w), 1415(w), 1377(m), 1271(m), 1157(s), 1051(vs), 966(w), 850(w), 758(vs), 621(s).

2.7.3.12. Synthesis of $[In(\mu\text{-}4\text{-}Cl\text{-}pz)_3]_n$ (13)

Compound **13** was prepared in the same manner as for **12**, using complex **2** (52.5 mg, 0.1 mmol) and pip (29.7 μL, 0.3 mmol) in 3 mL CH_2Cl_2. Yield: 91%. Analysis for $C_9H_6Cl_3InN_6$ (419.37 g mol^{-1}), Calcd: C, 25.95; H, 1.45; N, 20.19; Found: C, 25.91; H, 1.76; N, 17.71. FTIR (cm^{-1}, solid): 3280 (w), 3122(w), 1494(w), 1390 (m), 1298(s), 1203(m), 1051(vs), 971(s), 841(s), 760(w), 613(s).

2.7.3.13. Synthesis of $[In(\mu\text{-}4\text{-}I\text{-}pz)_3]_n$ (14)

Compound **14** was prepared in the same manner as for **12**, using complex **4** (402.2 mg, 0.5 mmol) and pip (148.3 μL, 1.5 mmol) in 3 mL CH_2Cl_2. Yield: 95%. Analysis for $C_9H_6I_3InN_6$ (693.72 g mol^{-1}), Calcd for **14**•EtOH: C, 17.86; H, 1.64; N, 11.36; Found: C, 17.53; H, 2.31; N, 10.83. FTIR (cm^{-1}, solid): 3315(w), 2942(w), 1471(w), 1371(m), 1286(s), 1155(m), 1049(vs), 987(m), 941(vs), 839(s), 611(vs).

2.7.3.14. Synthesis of $[In(\mu\text{-}4\text{-}Ph\text{-}pz)_3]_n$ (15)

Compound **15** was prepared in the same manner as for **12**, using complex **6** (13.2 mg, 0.02 mmol) and pip (6 μL, 0.06 mmol) in 2 mL CH_2Cl_2. Yield: 97%. Analysis for $C_{24}H_{21}InN_6$ (508.29 g mol^{-1}), Calcd for **15**•EtOH: C, 56.33; H, 4.90; N, 15.16; Found: C, 56.79; H, 4.85; N, 14.14. FTIR (cm^{-1}, solid): 3322(w), 2919(w), 1606(w), 1560(w), 1458(w), 1373(m), 1247(m), 1157(m), 1111(m), 1047(s), 953(m), 850(m), 758(s), 692(s), 611(w).

2.7.4. X-ray crystallography

Single crystal X-ray diffraction data were collected on a Bruker D8 QUEST diffractometer equipped with a PHOTON 100 or a PHOTON 2 detector operating at T =

298 K. Data were collected with the shutterless ω-scan technique using graphite-monochromated Mo-Kα radiation (λ = 0.71073 Å). Data were collected using the APEX 3 suite and structure solutions were obtained using intrinsic phasing with SHELXT.[100,101] Data were refined on Olex2 interface, by full-matrix least-squares minimization in SHELXL.[102] Multiscan absorption corrections were applied. All non-hydrogen atoms were refined anisotropically. Residual electron density in solvent-accessible voids of the lattice, attributed to disordered interstitial solvent molecules (MeOH for **1**, and acetone for **9**, **10** and **11**), which could not be refined, was removed with the SQUEEZE routine of the PLATON suite.[103]

Table 8. Structure refinement parameters for complexes **1 – 8**.

Compound	**1**	**2**	**3**	**4**	**5**	**7**	**8**
CCDC #	2174008	2174009	2174010	2174011	2174012	2270927	2270928
Empirical formula	$C_9H_{12}Cl_3InN_6$	$C_9H_9Cl_6InN_6$	$C_9H_9Br_3Cl_3InN_6$	$C_9H_9Cl_3I_3InN_6$	$C_{15}H_{26}Cl_3InN_6O$	$C_{12}H_{18}Cl_3InN_6$	$C_{24}H_{38}Cl_3InN_{12}O$
Formula weight	425.42	528.74	678.12	803.09	527.59	467.49	731.83
Temperature/K	296	296	296	296	296	296	296
Crystal system	monoclinic	triclinic	monoclinic	monoclinic	monoclinic	orthorhombic	triclinic
Space group	$P2_1/n$ (No. 14)	P-1 (No. 2)	$C2/c$ (No. 15)	$C2/c$ (No. 15)	$P2_1/n$ (No. 14)	$P2_12_12_1$ (No. 19)	P-1 (No. 2)
a/Å	8.6493(8)	6.885(1)	21.514(2)	21.946(1)	9.332(2)	11.6835(9)	10.2095(6)
b/Å	14.177(1)	10.552(2)	13.477(1)	13.7032(8)	16.936(3)	11.867(1)	10.2382(6)
c/Å	12.887(1)	12.437(2)	14.590(1)	14.760(1)	13.806(3)	13.770(1)	17.191(1)
α/°	90	78.541(5)	90	90	90	90	75.916(2)
β/°	106.311(3)	89.430(5)	103.642(2)	103.395(2)	92.046(5)	90	82.198(2)
γ/°	90	87.010(5)	90	90	90	90	89.170(2)
Volume/$Å^3$	1516.6(2)	884.4(3)	4110.7(6)	4318.2(4)	2180.6(8)	1909.2(3)	1726.5(2)
Z	4	2	8	8	4	4	2
ρ_{calc} g/cm^3	1.863	1.986	2.327	2.478	1.580	1.626	1.408
μ/mm^1	2.082	2.244	7.374	5.775	1.465	1.662	0.954
Ref. Coll./Indp.	19686/2675	12966/3883	8140/4230	8512/5153	45430/5406	41695/4221	19101/4467
R_{int}/R_σ	0.0230/0.0216	0.0198/0.0259	0.1635/0.0646	0.0518/0.0661	0.0492/0.0674	0.0386/0.0502	0.0418/0.1140
Θ_{max}/ % completn.	25.047/1.00	27.099/0.996	26.442/0.962	27.939/0.997	28.279/0.997	28.303/1.00	26.398/0.998
T_{min}/T_{max}	0.704/0.745	0.661/0.746	0.336/0.745	0.673/0.746	0.679/0.746	0.525/0.923	0.6856/0.7454
Param./[a]Obsv. Ref.	173/2434	204/3643	200/3376	200/3340	245/4302	211/4734	391/7038
[b]GooF on F^2	1.161	1.106	1.015	1.034	1.121	1.185	1.048
[c]wR_2	0.0378	0.0554	0.1517	0.0716	0.0914	0.0754	0.1322
[d]R_1	0.0181	0.0238	0.0528	0.0402	0.0437	0.0370	0.0601

[a] $I_o > 2\sigma(I_o)$

[b] GooF = $[\Sigma[w(F_o^2-F_c^2)^2]/(N_o-N_v)]^{1/2}$ (N_o=*number of observations*, N_v=*number of variables*)

[c] $wR_2 = \Sigma||F_o|-|F_c||/\Sigma|F_o|$

[d] $R_1 = [(\Sigma w(F_o^2-F_c^2)/\Sigma|F_o|^2)]^{1/2}$

Table 9. Structure refinement parameters for complexes **9 – 11**.

Compound	**9** • $(CH_3)_2CO$	**10** • 2(pipHCl)• $(CH_3)_2CO$	**11**
CCDC#	2174013	2174014	2174015
Empirical formula	$C_{72}H_{134}Cl_{12}In_{12}N_{30}O_{18}$	$C_{46}H_{85}Cl_{14}In_6N_{17}O_9$	$C_{69}H_{85}Cl_6In_6N_{15}O_8$
Formula weight	3511.32	2205.52	2154.09
Temperature/K	296	296	296
Crystal system	triclinic	monoclinic	hexagonal
Space group	*P*-1 (No. 2)	$P2_1/c$ (No. 14)	$P6_3/m$ (No. 176)
a/Å	18.801(5)	15.299(3)	17.185(2)
b/Å	19.503(5)	15.995(3)	17.185(2)
c/Å	20.281(5)	34.526(6)	18.443(2)
α/°	114.005(2)	90	90
β/°	91.512(3)	93.324(2)	90
γ/°	91.947(3)	90	120
Volume/$Å^3$	6783(3)	8434(3)	4717(1)
Z	2	4	2
$\rho_{calc}g/cm^3$	1.719	1.737	1.517
μ/mm^1	2.294	2.109	1.664
Ref. Coll./Indp. Ref.	65490/24128	80327/14887	45927/2879
R_{int} /R_σ	0.0524/0.0615	0.033/0.0492	0.0303/0.0418
Θ_{max}/ % completn.	25.241/0.984	25.04/0.996	25.016/1.00
T_{min}/T_{max}	0.538/0.746	0.524/0.703	0.629/0.745
Param./[a]Obsv. Ref.	1388/16389	856/11663	171/2260
[b]GooF	1.028	1.067	1.143
[c]wR_2	0.0851	0.0740	0.0744
[d]R_1	0.0361	0.0338	0.0282

[a] $I_o > 2\sigma(I_o)$

[b] GooF = $[\Sigma[w(F_o^2-F_c^2)^2]/(N_o-N_v)]^{1/2}$ (N_o=*number of observations*, N_v=*number of variables*)

[c] $wR_2 = \Sigma||F_o|-|F_c||/\Sigma|F_o|$

[d] $R_1 = [(\Sigma w(F_o^2-F_c^2)^2/\Sigma|F_o|^2)]^{1/2}$

Chapter 3: Synthesis and characterization of heterobimetallic oxide complexes

3. Synthesis of heterobimetallic oxide complexes

3.1. Introduction

Hetero-multinuclear metal complexes are also of interest as they are part of the active site of several biological systems. A common approach to synthesize hetero-multinuclear metal complexes is by direct coordination of ligands and metal ions based on their affinity. However, differentiation of the metal ions, particularly *3d* transition metals, is challenging and alternative synthetic methods are needed.[104]

Recently, Dr. Raptis's group have described in a series of publications the structural, spectroscopic, magnetic, and redox properties of a family of redox-active octanuclear complexes of general formula $[Fe^{III}_8(\mu_4\text{-}O)_4(\mu\text{-}pz^*)_{12}X_4]$, where pz^* = 4-substituted pyrazolato anion and X = Cl, Br and NCS.[41] Main group ions, like Ga^{3+} and In^{3+}, have been shown by the Raptis' group, based on ESI-MS analysis, to form $Fe_{8-x}M_x$ iron heterobimetallic materials whose structural unit models the structures of iron oxide minerals (courtesy of Prof. G. Mezei, Western Michigan University; unpublished results). The $Fe_{8-x}M_x$ materials consist of mixtures of co-crystallized species with x = 0 – 4, not allowing further characterization of individual components. Given that the range of crystal radii of Ga^{3+} (0.76 Å) and In^{3+} (0.94 Å) overlap with the crystal radii of several actinides (in their higher oxidation states), investigation of the formation of Fe/M octanuclear complexes modeling oxide minerals employing pyrazole/pyrazolato ligands is an appropriate strategy. Furthermore, indium in its +3 stable oxidation state might serve as a surrogate for lanthanide chemistry, even if it has a smaller crystal radius -- all lanthanides

have crystal radii between1.17 Å and 1.02 Å[28] -- lanthanides have been established as promising surrogates for actinide chemistry in the literature.

To better characterize the Fe/In-oxo-pyrazolato complexes, a new two-pronged synthetic effort was undertaken: (a) Reactions of iron pyrazole complexes with indium chloride and (b) reactions of indium pyrazole complexes (of sections 2.1) with commercially available ferric and ferrous starting materials (Scheme 10). Both strategies are based on the propensity of iron to form oxide clusters, in which indium ions might be incorporated to a varying extent, depending on reaction stoichiometry and conditions (solvent, temperature, etc.)

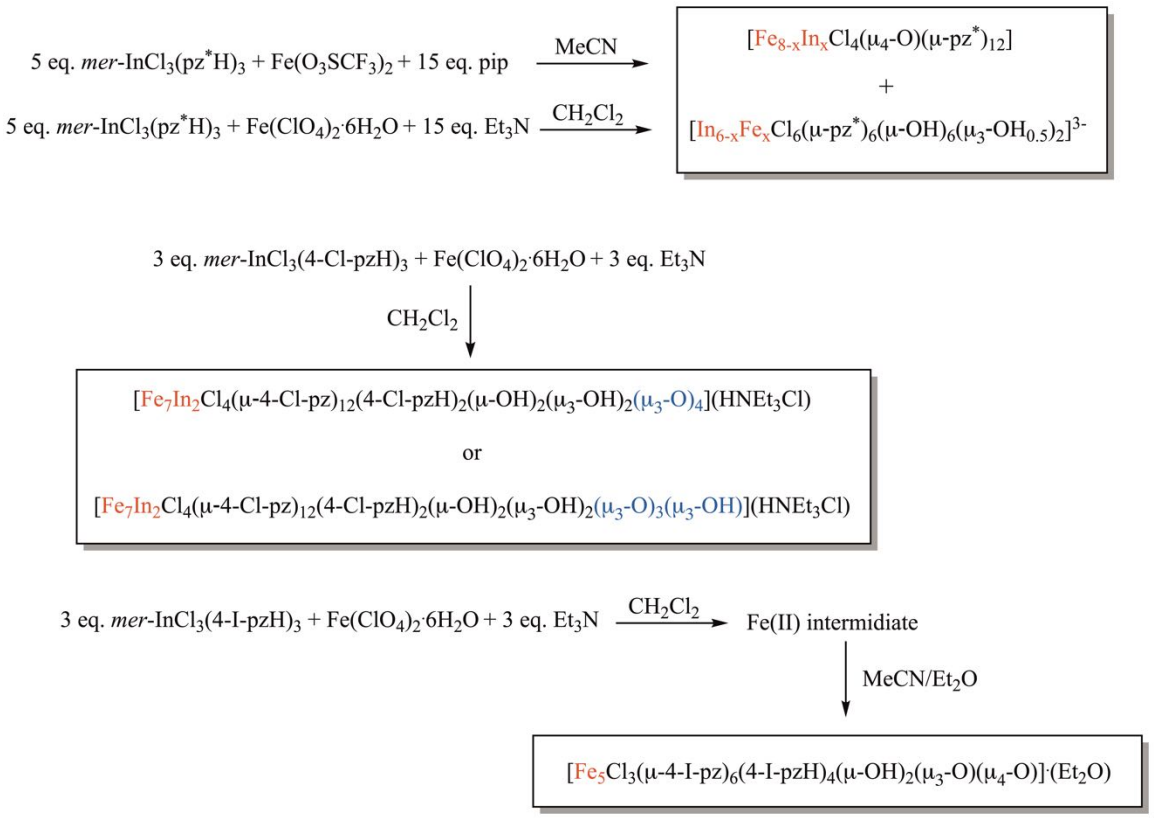

Scheme 10. Synthetic pathway for heterobimetallic Fe/In complexes and homometallic Fe_5 complex starting from *mer*-[$InCl_3(pz^*H)_3$] and an iron salt.

3.2. Results and Discussion

3.2.1. Synthesis of $[Fe_{8-x}In_xCl_4(\mu_4\text{-}O)_4(\mu\text{-}pz^*)_{12}]$

Complexes of general formula $[Fe_{8-x}In_xCl_4(\mu_4\text{-}O)_4(\mu\text{-}pz^*)_{12}]$, where pz^*= pz, 4-Cl-pz, 4-Br-pz, and 4-I-pz, were prepare from a suspension of *mer*-$[InCl_3(pz^*H)_3]$ and anhydrous $Fe(O_3SCF_3)_2$ or $Fe(ClO_4)_2{\cdot}6H_2O$ in MeCN or CH_2Cl_2 upon addition of pip or Et_3N (Scheme 10) and recrystallized as red prism-like crystals. Herein, $[Fe_{6.56}In_{1.44}Cl_4(\mu_4\text{-}O)_4(\mu\text{-}pz)_{12}]$ (**16**), isolated from the reaction *mer*-$[InCl_3(pzH)_3]$ and anhydrous $Fe(O_3SCF_3)_2$ in MeCN upon addition of pip, is reported along with the SCXRD, ESI-MS, and SEM-EDS data. The crystal yield is small; we have not been able to obtain this material in bulk, so far. These reactions produce some bright yellow crystals as byproduct, which correspond to the hexanuclear indium complex with some iron occupancy. Similar reactions with 4-Cl-pz, 4-Br-pz, and 4-I-pz pyrazolato were attempted but good quality crystals for SCXRD were not obtained.

3.2.2. Mass spectrometry of $[Fe_{8-x}In_xCl_4(\mu_4\text{-}O)_4(\mu\text{-}pz)_{12}]$

Quantitative information was obtained from Electrospray Ionisation Mass Spectrometry (ESI-MS) in MeCN performed by collaborators from Purdue University, which also provided some structural understanding. The $[Fe_{8-x}In_xCl_4(\mu_4\text{-}O)_4(\mu\text{-}pz)_{12}]$ fragments can be all found between 1440 m/z and 1700 m/z (Figure 37). $[Fe_7InCl_4(\mu_4\text{-}O)_4(\mu\text{-}pz)_{12}]$ comprises the larger component of the sample, followed by $[Fe_8Cl_4(\mu_4\text{-}O)_4(\mu\text{-}pz)_{12}]$ and $[Fe_6In_2Cl_4(\mu_4\text{-}O)_4(\mu\text{-}pz)_{12}]$. The $[Fe_4In_4Cl_4(\mu_4\text{-}O)_4(\mu\text{-}pz)_{12}]$ species – all outer metal sites substituted by indium – is the smallest component. The ESI-MS shows the coexistence of all species with general formula $[Fe_{8-x}In_xCl_4(\mu_4\text{-}O)_4(\mu\text{-}pz)_{12}]$ where x = 0 –

4. The presence of each molecular ion and fragment in the mixture slightly differs from one batch to the other.

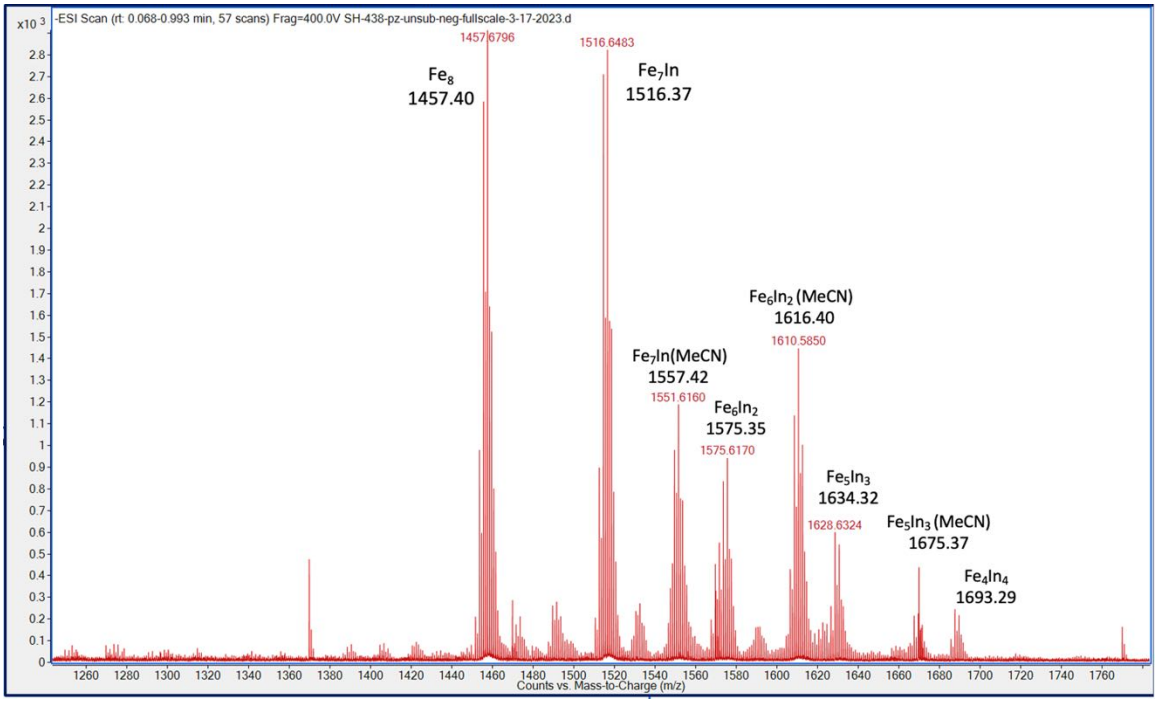

Figure 37. ESI-MS of $[Fe_{8-x}In_xCl_4(\mu_4\text{-}O)_4(\mu\text{-}pz)_{12}]$, where x = 0 – 4. Collected data (red) and calculated molecular weight of the corresponding fragments (black).

3.2.3. Crystallographic description of $[(Fe_{0.64}In_{0.36})_4Fe_4Cl_4(\mu_4\text{-}O)_4(\mu\text{-}pz)_{12}]$ (16)

Crystallographic data collection and refinement parameters for the isolated fragment with formula $[(Fe_{0.64}In_{0.36})_4Fe_4Cl_4(\mu_4\text{-}O)_4(\mu\text{-}pz)_{12}]$ (**16**) are summarized in Table 15. Crystallographically, it was determined that the percent of indium, occupying the outer cluster sites for **16**, was in the 30 – 40 % range. There was no indium in the cubane core sites (Figure 39). The cubane iron sites are all in a 6-coordinate octahedral environment formed by three bridging pyrazolato ligands and three μ_4-O atoms. The outer metal sites are in a 5-coordinate trigonal bipyramidal environment formed by three bridging pyrazolato ligands, a μ_4-O atom, and a terminal chloride. The core metal sites have pseudo-

octahedral geometries with a facial array of three oxides and three nitrogens from the bridging pyrazolato ligands. Same as the analogous $[Fe_8Cl_4(\mu_4\text{-}O)_4(\mu\text{-}pz)_{12}]$, complex **16** crystallizes in the triclinic *P*-1 space group and the unit cell parameters are statistically within error.[49] Complex **16** crystallizes with one interstitial Et_2O solvent molecule in the unit cell.

The bond distances for $In_{0.36}Fe_{0.64}$ – Cl and for the peripheral $In_{0.36}Fe_{0.64}$ – N are 2.281(2) Å - 2.310(3) Å and 2.041(9) Å - 2.086(7) Å, respectively (Table 10). Both are within statistical error of the analogous $[Fe_8Cl_4(\mu_4\text{-}O)_4(\mu\text{-}pz)_{12}]$.[49] However, the bond distances for the peripheral $In_{0.36}Fe_{0.64}$ – O are between 2.025(5) Å - 2.062(5) Å, which are significantly longer than for the corresponding $[Fe_8Cl_4(\mu_4\text{-}O)_4(\mu\text{-}pz)_{12}]$ complex. This is expected since the crystal radius of indium(III) is larger than the crystal radius of iron(III) (Table 10).

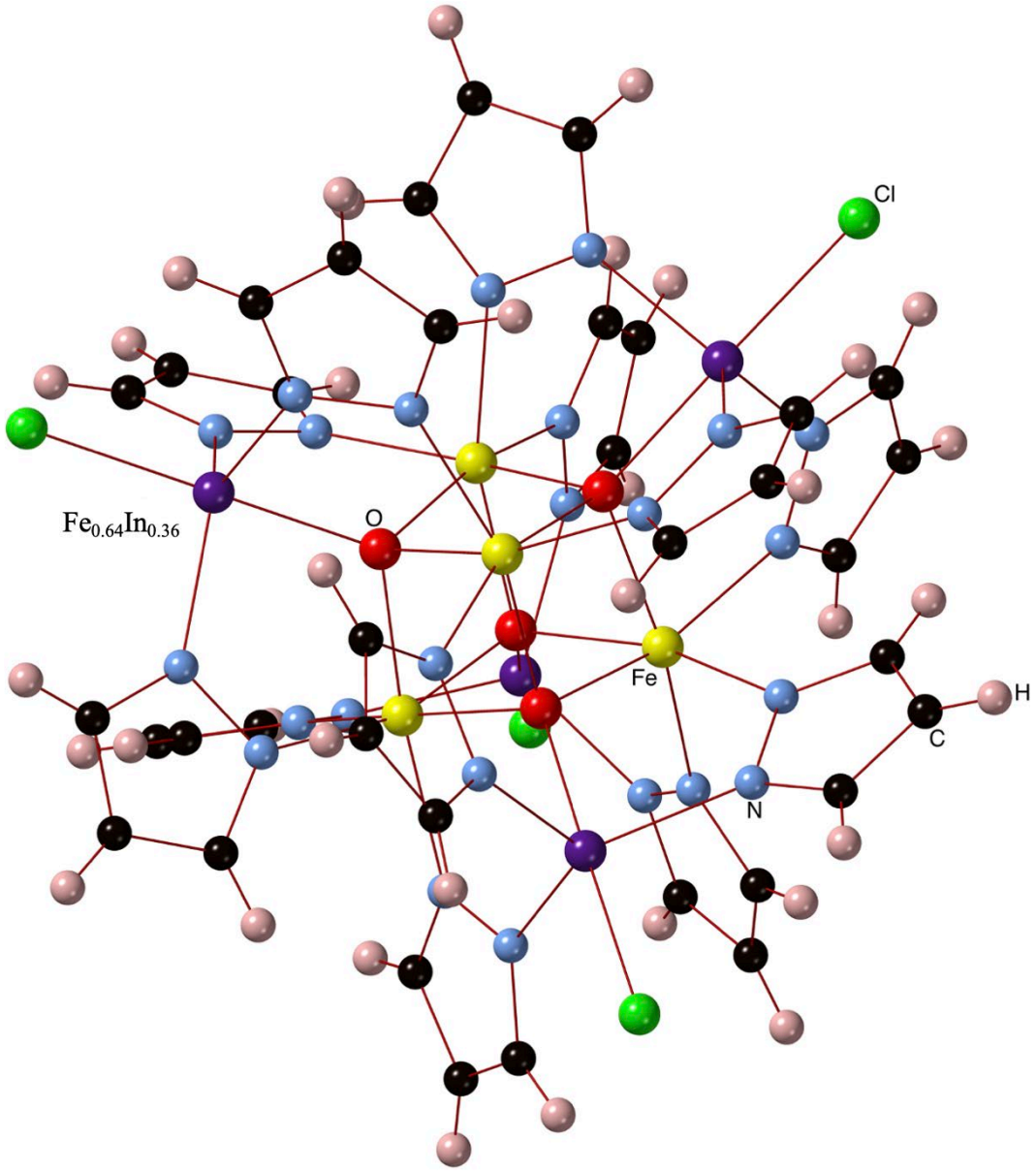

Figure 38. Ball-and-stick representation of [$(Fe_{0.64}In_{0.36})_4Fe_4Cl_4(\mu_4\text{-}O)_4(\mu\text{-}pz)_{12}$] (**16**). Solvent molecules are omitted for simplicity.

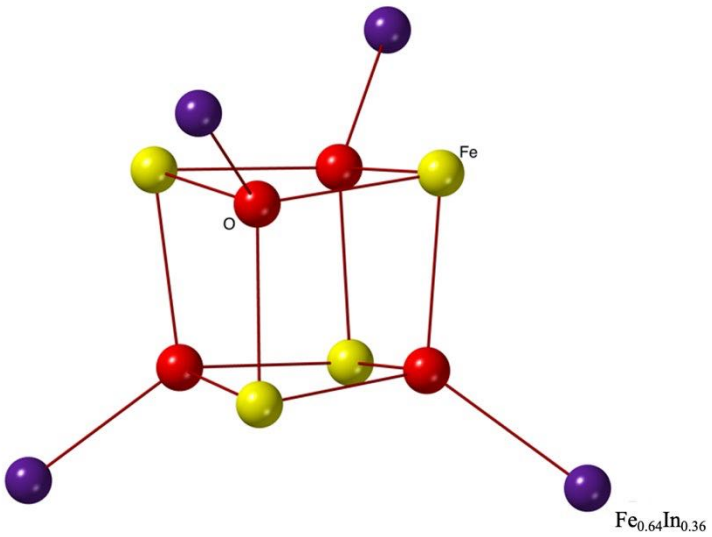

Figure 39. Structure of the $[Fe_{0.64}In_{0.36}O_4]$ core of (**16**).

Table 10. Selected bond lengths (Å) for **16** and analogous $[Fe_8Cl_4O_4(pz)_{12}]$ cluster.

	Compound	
Bond	**16** • Et_2O	**$Fe_8Cl_4O_4(pz)_{12}$** • hexane[105]
Fe_c – O	2.01(3) – 2.04(8)	2.032(6) – 2.066(7)
Fe_c – N	2.06(5) – 2.09(2)	2.044(9) – 2.086(8)
$(In_{0.36}Fe_{0.64})$ – O	2.025(5) – 2.062(5)	1.940(7) – 1.960(6)
$(In_{0.36}Fe_{0.64})$ – N	2.041(9) – 2.086(7)	2.003(9) – 2.038(10)
$(In_{0.36}Fe_{0.64})$ – Cl	2.281(2) – 2.310(3)	2.271(4) – 2.274(4)

3.2.4. SEM-EDS of $[(Fe_{0.64}In_{0.36})_4Fe_4Cl_4(\mu_4\text{-}O)_4(\mu\text{-}pz)_{12}]$ (16)

Single crystals of **16** were analyzed by SEM at 15kV and as a result, the image of the crystals with some solvent residues was obtained (Figure 40 and 41). The sample was subjected to EDS analysis by which the elemental composition (Figure 42) and weight percentage were estimated (Table 11). The assignment of the EDS spectrum accounts for a total of 100% weight of the sample. The results showed that iron is present in larger percentage than indium – approximately 4 to 5 times more – consistent with the single

crystal X-ray diffraction results. The presence of sulfur can only be from some $Fe(O_3SCF_3)_2$ starting material or adventitious impurities.

Figure 40. SEM image representing several crystals of **16** and residual solvent.

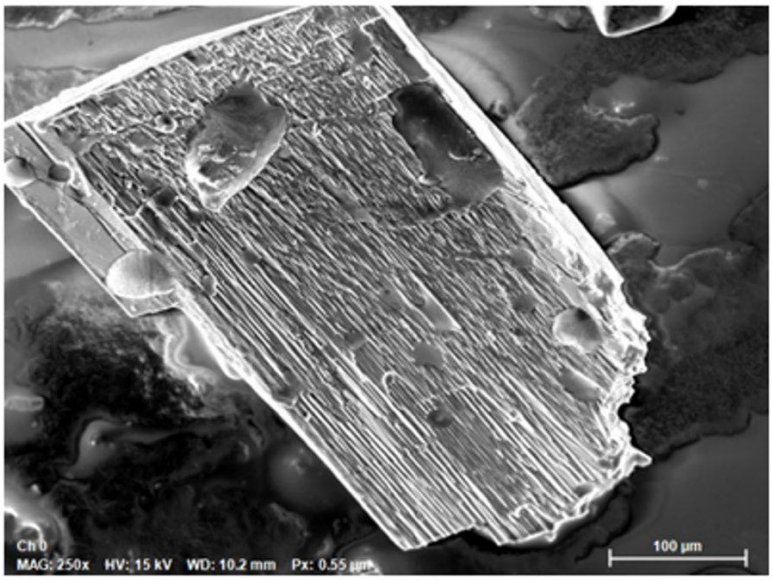

Figure 41. SEM image of one single crystal of **16** and residual solvent.

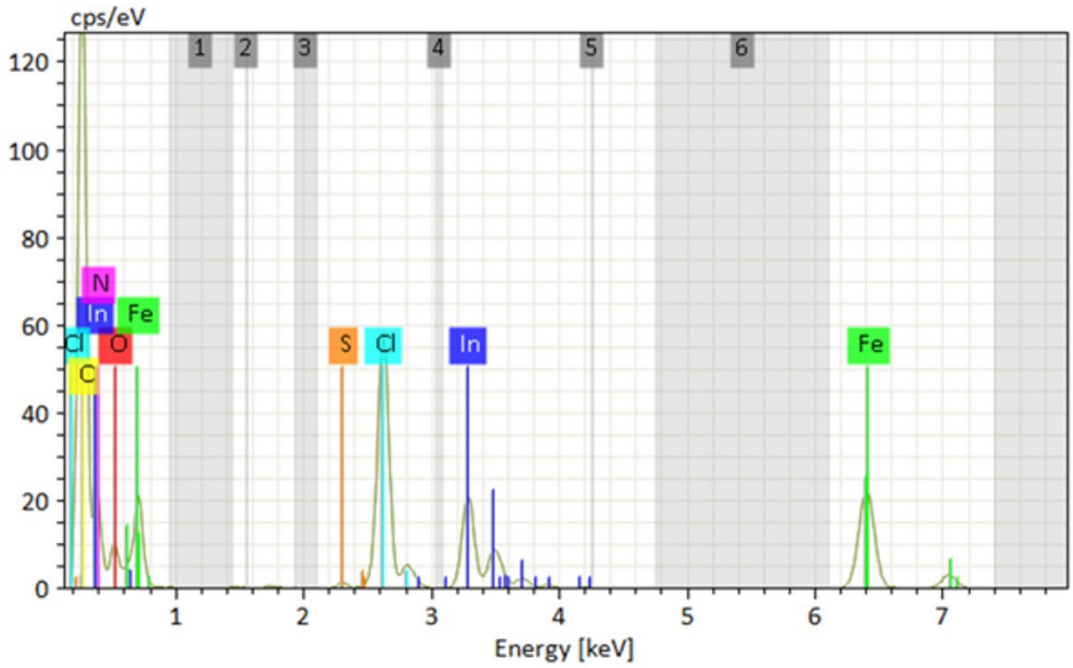

Figure 42. EDS image representing the elemental composition in **16**.

Table 11. EDS showing elemental composition and weight for **16**.

Element Name	Element Symbol	Mass (%)	Atom (%)	abs. error (%) (1σ)
Carbon	C	47.45	65.65	2.32
Nitrogen	N	17.19	20.40	0.91
Oxygen	O	4.73	4.91	0.24
Sulfur	S	0.11	0.06	0.01
Chlorine	Cl	6.67	3.13	0.17
Iron	Fe	15.74	4.68	0.40
Indium	In	8.11	1.17	0.21
	Sum	**100.00**	**100.00**	

3.2.5. UV-vis absorption of $[(Fe_{0.64}In_{0.36})_4Fe_4Cl_4(\mu_4\text{-}O)_4(\mu\text{-}pz)_{12}]$ (16)

The UV-vis spectra were recorded on an Agilent Technologies Cary 6000i Series UV-vis-NIR Spectrophotometer with 1 cm optical path length cuvettes in anhydrous MeCN solution from 200 – 800 nm. The spectra (Figure 43) show absorption maxima at 227 nm, 359 nm, and 683 nm, which have not yet been assigned, however the characteristic peak from previously published $Fe_8Cl_4(\mu_4\text{-}O)_4(\mu\text{-}pz^*)_{12}$ complexes is not observed around

437 nm.[41] The peak observed at 683 nm is in the blue/green visible region of the spectrum, which is not consistent with the observed red color of the crystal and the solution. The calculated extinction coefficients were $\varepsilon_{(227\ nm)}$ = 0.30 $\mu M^{-1}cm^{-1}$, $\varepsilon_{(259\ nm)}$ = 0.317 μM^{-1} cm^{-1}, and $\varepsilon_{(683\ nm)}$ = 0.057 $\mu M^{-1}cm^{-1}$, which are larger than the extinction coefficients of previously reported $Fe_8Cl_4(\mu_4\text{-}O)_4(\mu\text{-}pz^*)_{12}$ complexes.

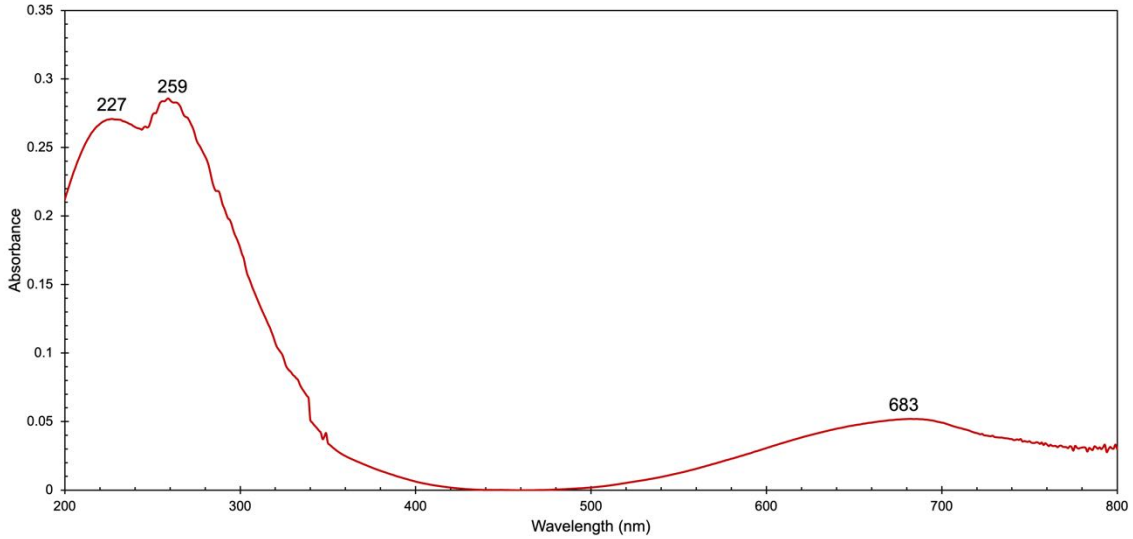

Figure 43. UV-vis spectrum of **16** in MeCN solution.

3.2.6. Synthesis of $[In_{6-x}Fe_xCl_6(\mu_3\text{-}OH_{0.5})_2(\mu\text{-}OH)_6(\mu\text{-}pz^*)_6]^{3-}$

Complexes of general formula $[In_{6-x}Fe_xCl_6(\mu_3\text{-}OH_{0.5})_2(\mu\text{-}OH)_6(\mu\text{-}pz^*)_6]^{3-}$, where pz^*= pz, 4-Cl-pz, 4-Br-pz, and 4-I-pz, were prepare from a suspension of *mer*-$[InCl_3(pz^*H)_3]$ and anhydrous $Fe(O_3SCF_3)_2$ or $Fe(ClO_4)_2{\cdot}6H_2O$ in MeCN or CH_2Cl_2 upon addition of pip or Et_3N (Scheme 10) and recrystallized as yellow crystals. $[In_{6-x}Fe_xCl_6(\mu_3\text{-}OH_{0.5})_2(\mu\text{-}OH)_6(\mu\text{-}pz^*)_6]^{3-}$ complexes are always a byproduct of the reaction of indium monomers deprotonated with piperidine or triethylamine and an iron starting material where octanuclear $[Fe_{8-x}In_x(\mu_4\text{-}O)_4(\mu\text{-}pz)_{12}Cl_4]$ compounds are the major product. Under different conditions, the crystals have a darker yellow color – which indicates a higher

concentration of iron – or paler yellow/almost colorless – which indicates less iron in the fragments. Herein, $(HNEt_3)_3[(In_{0.88}Fe_{0.12})_6Cl_6(\mu_3\text{-}OH_{0.5})_2(\mu\text{-}OH)_6(\mu\text{-}pz)_6]$ (**17**) (Figure 44), and $(HNEt_3)_3[(In_{0.92}Fe_{0.08})_6Cl_6(\mu_3\text{-}OH_{0.5})_2(\mu\text{-}OH)_6(\mu\text{-}4\text{-}I\text{-}pz)_6]$ (**18**) (Figure 45), isolated from the reaction of *mer*-$[InCl_3(pzH)_3]$ and anhydrous $Fe(O_3SCF_3)_2$ in MeCN; and *mer*-$[InCl_3(4\text{-}I\text{-}pzH)_3]$ and $Fe(ClO_4)_2{\cdot}6H_2O$ in CH_2Cl_2 upon addition of Et_3N are reported along with the SCXRD and SEM-EDS.

3.2.7. Crystallographic description of $(HNEt_3)_3[(In_{0.88}Fe_{0.12})_6Cl_6(\mu_3\text{-}OH_{0.5})_2(\mu\text{-}OH)_6(\mu\text{-}pz)_6]$ (17) and $(HNEt_3)_3[(In_{0.92}Fe_{0.08})_6Cl_6(\mu_3\text{-}OH_{0.5})_2(\mu\text{-}OH)_6(\mu\text{-}4\text{-}I\text{-}pz)_6]$ (18)

Crystallographic data collection and structure refinement parameters for complexes **17** and **18** are summarized in Table 15. Crystallographically it was determined that there is about 11.8 % iron occupancy in complex **17**. Complex **17** crystallizes in the monoclinic $P2_1/c$ space group. Interstitial MeCN solvent molecules lower the crystallographic symmetry of **17**. The unit cell shows one full hexanuclear molecule and three Et_3NH^+ counterions. Each $Fe_{0.12}In_{0.88}$-center shows a six-coordinate octahedral environment (Figure 44). The bond distances for $Fe_{0.12}In_{0.88}$– Cl are 2.45(2) Å – 2.46(3) Å (Table 12). The bond distances for $Fe_{0.12}In_{0.88}$– N are 2.19(3) Å - 2.25(4) Å. The - bond distances for $Fe_{0.12}In_{0.88}$– (μ_3-$OH_{0.5}$) are 2.16(4) Å – 2.22(1) Å, and the bond distance for $Fe_{0.12}In_{0.88}$– (μ-OH) are 2.16(1) Å – 2.22(2) Å. The bond distances for **17** are statistically the same as the bond distances for the analogous all-indium complex (**9**).

Crystallographically it was determined that there is a 9% iron occupancy in complex **18**, which crystallized in the trigonal *R*-3 space group with one Et_3NH^+ counter ion per one-third of the hexanuclear molecule per asymmetric unit. Each $Fe_{0.08}In_{0.92}$-center shows a six-coordinate octahedral environment (Figure 45). The packing diagram of the

structure viewed down the *c*-axis shows that trimeric faces [001] are staggered, forming a hexagonal projection (Figure 46). The $Fe_{0.08}In_{0.92}$ – Cl, and $Fe_{0.08}In_{0.92}$ – N bond distances are 2.45(1) Å – 2.45(1) Å and 2.13(9) Å – 2.31(10) Å, respectively (Table 12). The $Fe_{0.08}In_{0.92}$ – (μ_3-$OH_{0.5}$) bond distances are between 2.16(5) Å and 2.19(5) Å, statically indistinguishable from the bond distance for $Fe_{0.08}In_{0.92}$ – (μ-OH) of 2.17(3) Å to 2.19(5) Å.

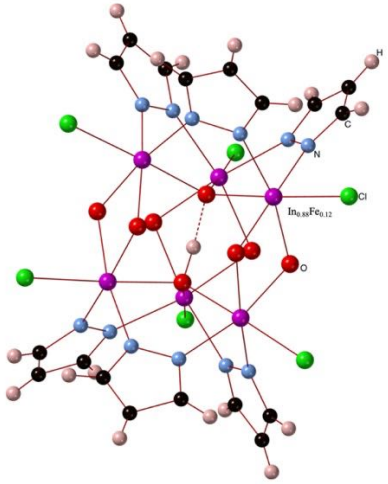

Figure 44. Ball-and-stick representation of $[(In_{0.88}Fe_{0.12})_6Cl_6(\mu_3\text{-}OH_{0.5})(\mu\text{-}OH)_6(\mu\text{-}pz)_6]^{3-}$ (**17**); H's from (μ-OH) and counterions was omitted for simplicity.

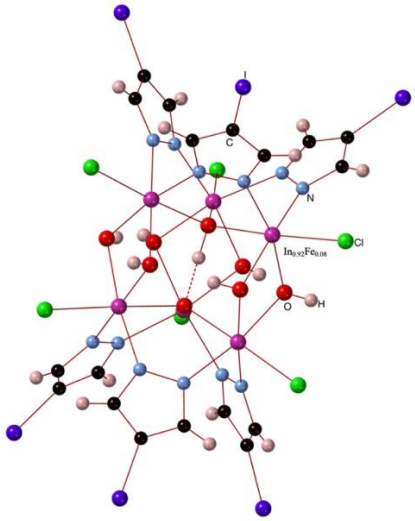

Figure 45. Ball-and-stick representation of $[(In_{0.92}Fe_{0.08})_6Cl_6(\mu_3\text{-}OH_{0.5})(\mu\text{-}OH)_6(\mu\text{-}4\text{-}I\text{-}pz)_6]^{3-}$ (**18**); counterion was omitted for simplicity.

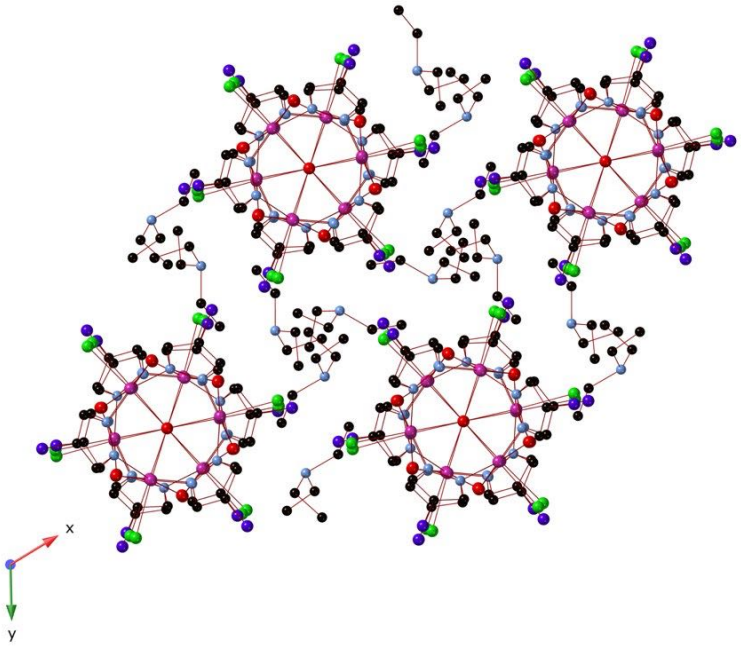

Figure 46. Illustration of crystal packing of **18** shown the *c*-axis showing the $HNEt_3$ counterions; H were omitted for simplicity.

Table 12. Selected bond lengths (Å) for **17** and **18**.

Interatomic Distances	17	18
$(Fe_xIn_{1-x}) - Cl$	2.45(2) – 2.46(3)	2.45(6) – 2.45(1)
$(Fe_xIn_{1-x}) - N$	2.19(3) – 2.25(4)	2.13(9) – 2.31(10)
$(Fe_xIn_{1-x}) - (\mu_3\text{-}OH_{0.5})$	2.16(4) – 2.22(1)	2.16(5) – 2.19(5)
$(Fe_xIn_{1-x}) - (\mu\text{-}OH)$	2.16(1) – 2.22(2)	2.17(3) – 2.19(5)
$Fe_xIn_{1-x} \cdots (Fe_xIn_{1-x})^a$	3.37(1) – 3.41(1)	3.37(1) – 3.41(1)
$Fe_xIn_{1-x} \cdots (Fe_xIn_{1-x})^b$	3.68(3) – 3.76(3)	3.68(1) – 3.73(3)

[a](μ-OH) bridged; [b](μ-pz) bridged

3.2.8. SEM-EDS of $(HNEt_3)_3[(In_{0.88}Fe_{0.12})_6Cl_6(\mu_3\text{-}OH_{0.5})_2(\mu\text{-}OH)_6(\mu\text{-}pz)_6]$ (17)

Single crystals of **17** after isolation were analyzed through SEM at 15kV and as a result, the image of the crystals was obtained (Figure 47). The sample was subjected to EDS for the elemental composition (Figure 48) and weight concentration to be estimated (Table 13) by selecting different areas of the crystals. The assignment of the EDS spectrum account for a total of 16.32% weight of the sample; carbon and nitrogen could not be

accurately quantified. Mapping of the crystal by EDS showed a homogenous distribution of indium, chlorine, and iron throughout the crystals (Figure 49). The results showed that indium is present in larger quantities than iron – 11.18 % iron content -- consistent with the single crystal X-ray diffraction results. The small amount of aluminum and silicone found correspond to the sample mount.

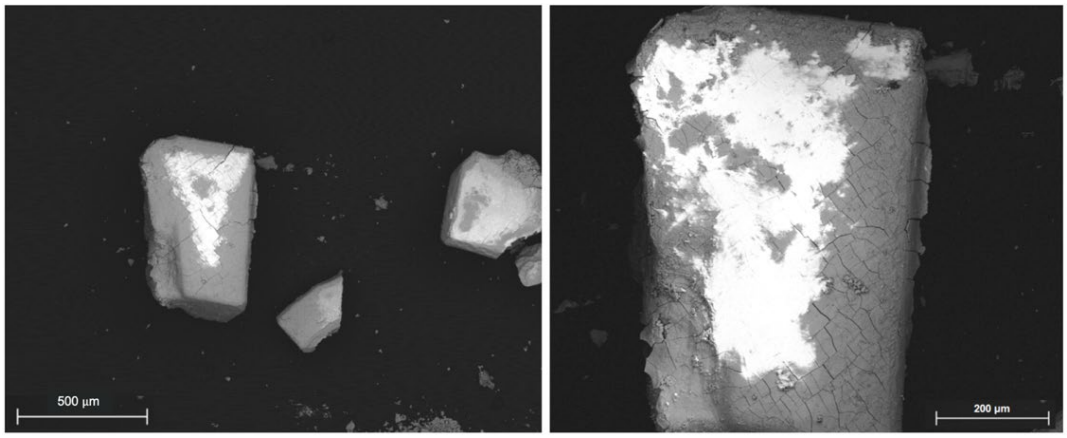

Figure 47. SEM images representing several crystals (left) and one single crystal (right) of **17** at two different scales.

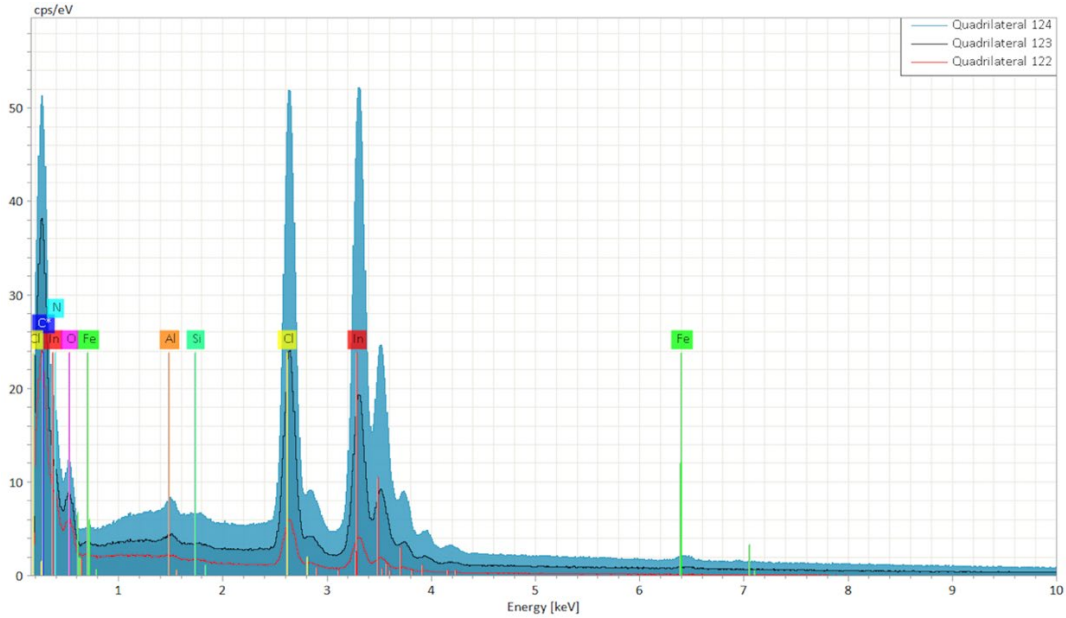

Figure 48. EDS image representing the elemental composition in **17**. (Quadrilateral 122, 123, and 124; three quadrilateral sections sampled for EDS).

Table 13. EDS showing elemental composition and weight for **17**.

Element Name	Element Symbol	Mass (%)	Atom (%)	abs. error (%) (1σ)
Carbon	C			
Nitrogen	N	3.68	38.15	0.44
Oxygen	O	5.03	45.67	0.60
Aluminum	Al	0.31	1.66	0.04
Silicone	Si	0.00	0.02	0.00
Chlorine	Cl	1.76	7.20	0.08
Iron	Fe	0.23	0.60	0.03
Indium	In	5.31	6.71	0.18
	Sum	**16.32**	**100.00**	

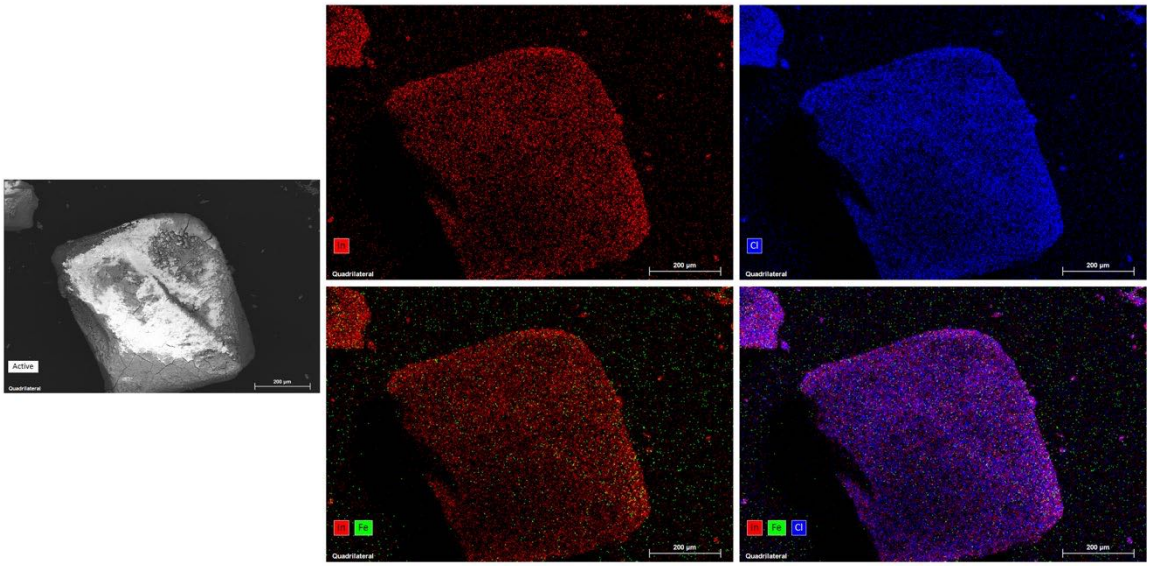

Figure 49. Mapping of complex **17** by EDS showing homogenous distribution of In (red), Cl (blue), and Fe (green).

3.2.9. Synthesis of [$Fe^{III}_7In_2Cl_4(\mu_3\text{-}O)_2(\mu_3\text{-}OH)_2(\mu_3\text{-}OH_{0.5})_2(\mu\text{-}OH)_2(\mu\text{-}4\text{-}Cl\text{-}pz)_{12}(4\text{-}Cl\text{-}pzH)_2$](Et$_3$NHCl) (19)

Complex of formula [$Fe^{III}_7In_2Cl_4(\mu_3\text{-}O)_2(\mu_3\text{-}OH)_2(\mu_3\text{-}OH_{0.5})_2(\mu\text{-}OH)_2(\mu\text{-}4\text{-}Cl\text{-}pz)_{12}(4\text{-}Cl\text{-}pzH)_2$](Et$_3$NHCl) (**19**) (Figure 50) was prepared by adding triethylamine to a mixture of *mer*-[$InCl_3(4\text{-}Cl\text{-}pzH)_3$] and $Fe(ClO_4)_2{\cdot}6H_2O$ in methylene chloride. Crystallization was achieved by slow diffusion of hexane into the reaction filtrate, yield only just a few crystals. However, this reaction has not been reproducible again under the

same conditions. The yield was just a few crystals. Complex **19** can alternatively be interpreted as $[Fe^{III}_6Fe^{IV}In_2Cl_4(\mu_3\text{-}OH)_2(\mu_3\text{-}O)_4(\mu\text{-}OH)_2(\mu\text{-}4\text{-}Cl\text{-}pz)_{12}(4\text{-}Cl\text{-}pzH)_2](Et_3NHCl)$ (Figure 51). More sample is necessary to acquire ^{57}Fe-Mössbauer spectra and to determine the oxidation state of each iron atom and perform additional characterization like UV-vis and ^{1}H NMR, of the complex in solution.

3.2.10. Crystallographic description of $[Fe^{III}_7In_2Cl_4(\mu_3\text{-}O)_2(\mu_3\text{-}OH)_2(\mu_3\text{-}OH_{0.5})_2(\mu\text{-}OH)_2(\mu\text{-}4\text{-}Cl\text{-}pzH)_{12}(4\text{-}Cl\text{-}pzH)_2](Et_3NHCl)$ (19)

$[Fe^{III}_7In_2Cl_4(\mu_3\text{-}O)_2(\mu_3\text{-}OH)_2(\mu_3\text{-}OH_{0.5})_2(\mu\text{-}OH)_2(\mu\text{-}4\text{-}Cl\text{-}pz)_{12}(4\text{-}Cl\text{-}pzH)_2](Et_3NHCl)$ (**19**) crystallizes in the tetragonal $P4_32_12$ space group with half the molecule in the asymmetric unit. The two indium centers have the same 6-coordinate octahedral environment formed by four bridging pyrazolato ligands, a terminal chloride, and a bridging (hydr)oxo. Four iron centers are equivalent and have a 6-coordinate octahedral environment formed by three bridging pyrazolato ligands, and three bridging (hydr)oxo in a *fac*-N_3O_3 arrangement. Two more iron centers are equivalent and in a 6-coordinate octahedral environment formed by two bridging pyrazolato, one pyrazole ligand, one μ_3-O, one μ-OH, and a terminal chloride in a *fac*-N_3O_2Cl arrangement. The last iron center is unique and is in a 4-coordinate tetrahedral environment formed by four bridging hydroxides. One Et_3NHCl is co-crystallized with **19**, with its chloride ion H-bonded to two μ-OH, while the triethylammonium cation is occupying a position of no chemical significance.

Crystallographic structure refinement parameters and selected metric parameters for **19** are shown in Table 15. The bond distance for Fe_o – Cl is 2.33(2) Å and for In – Cl is 2.47(2) Å, with the indium bond distance being longer due to indium having a larger

atomic radii than iron. The In – (μ_3-$OH_{0.5}$) distance is 2.10(2) Å and the In – Npz^* bond lengths are between 2.21(1) Å and 2.27(1) Å. The Fe_o – (Npz^*H) bond distance of 2.17(3) Å is longer than the Fe_o – (Npz^*) bond distances of 2.11(6) Å - 2.13(5) Å. The Fe_o – (μ_3-$OH_{0.5}$) bond distances are between 2.08(2) Å and 2.09(5) Å. The Fe_o – (μ_3-O) distances are between 1.89(2) Å and 2.01(4) Å. The Fe_o – (μ-OH) bond distance is 2.04(1) Å and the Fe_t – (μ-OH) distance is 1.92(1) Å, shorter than for the iron atoms in an octahedral environment, as expected. Likewise, the Fe_o – (μ_3-OH) bond distance is 1.99(4) Å and the Fe_t – (μ_3-OH) distance is 1.84(4) Å. The torsion angle for In – $OH_{0.5}$ – Fe_o – Fe_o is 129.5(4)° (Figure 52). The torsion angle for Fe_t – (μ_3-OH) – Fe_o – Fe_o is 135.6(4)° and the torsion angle for Fe_o – (μ_3-O) – Fe_o – Fe_o is 4.50(19)°.

The Fe_t – (μ-OH) and Fe_t – (μ_3-OH) average bond distances are statically shorter than the Fe_o – (μ-OH) and Fe_o– (μ_3-OH) average bond distances which can be due to the coordination geometry. On the other hand, the torsion angle of In – $OH_{0.5}$ – Fe_o – Fe_o is 129.5(4)° (Figure 52), which suggests a hydroxo bridge; as well as the O – H ··· O intramolecular bond length of 2.49(4) Å, which is shorter than the O – H ··· O bond length of several previously studied structures,[106] it is most likely that the correct formula for complex **19** is $[Fe^{III}_7In_2Cl_4(\mu_3\text{-}O)_2(\mu_3\text{-}OH)_2(\mu_3\text{-}OH_{0.5})_2(\mu\text{-}OH)_2(\mu\text{-}4\text{-}Cl\text{-}pz)_{12}(4\text{-}Cl\text{-}pzH)_2](Et_3NHCl)$.

An alternative interpretation of the chemical formula of **19**, with a $\{Fe^{III}_6Fe^{IV}In_2\}$ metal core, in which the tetrahedrally coordinated Fe-center in the +4 oxidation state, requires the absence of a (invisible to X-rays) proton. A proton can possibly be absent, in which case due to structural symmetry, would be most likely from the $OH_{0.5}$ ion, whose geometry, however, argues against this possibility. Yet, a firm assignment of oxidation

states can only be made once magnetic susceptibility and ^{57}Fe-Mössbauer data become available.

Table 14. Selected bond lengths (Å) for **19**.

Bond	19	Bond	19
In – Cl	2.47(2)	Fe_o – (Npz^*H)	2.17(3)
In – Npz^*	2.21(1) – 2.27(1)	Fe_o – (Npz^*)	2.11(6) – 2.13(5)
In - (μ_3-$OH_{0.5}$)	2.10(2)	Fe_o – (μ_3-$OH_{0.5}$)	2.08(2) – 2.09(5)
Fe_t – (μ-OH)	1.92(1)	Fe_o – (μ-OH)	2.04(1)
Fe_t – (μ_3-OH)	1.84(4)	Fe_o – (μ_3-O)	1.89(2) – 2.01(4)
Fe_o – Cl	2.33(2)	Fe_o – (μ_3-OH)	1.99(4)

Npz^*H = 4-Cl-pzH; Npz^* = 4-Cl-pz; Fe_t = tetragonal Fe; Fe_o = octahedral Fe

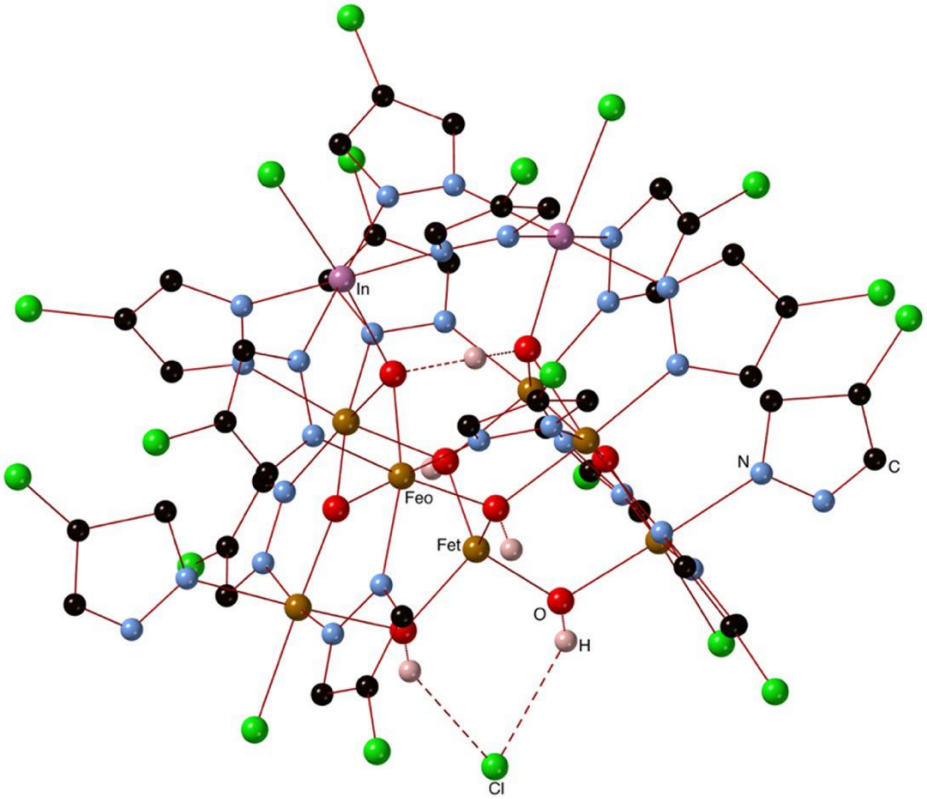

Figure 50. Ball-and-stick representation of $[Fe^{III}_7In_2Cl_4(\mu_3\text{-}OH)_2(\mu_3\text{-}O)_2(\mu_3\text{-}OH_{0.5})_2(\mu\text{-}OH)_2(\mu\text{-}4\text{-}Cl\text{-}pz)_{12}(4\text{-}Cl\text{-}pzH)_2](Et_3NHCl)$ of **19** viewed perpendicularly to the 2-fold symmetry axis; Et_3NH^+ and H atoms except (μ-OH) and (μ_3-OH) were omitted for simplicity. Fe_o, octahedral Fe; Fe_t, tetrahedral Fe.

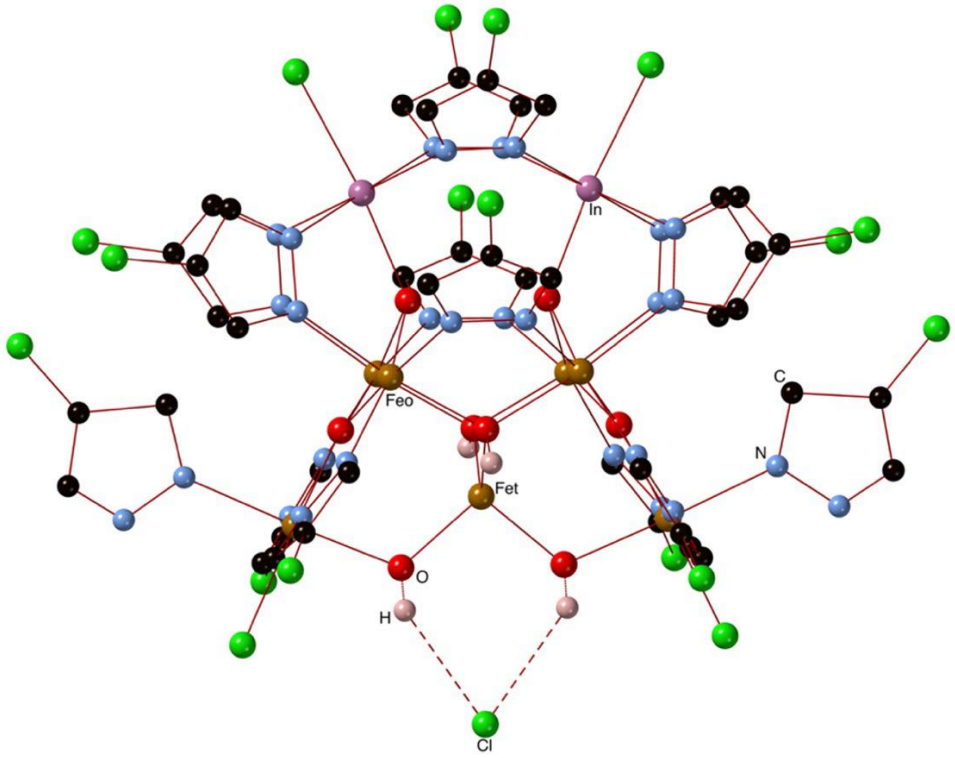

Figure 51. Alternative ball-and-stick representation of $[Fe^{III}_6Fe^{IV}In_2Cl_4(\mu_3\text{-}O)_4(\mu_3\text{-}OH)_2(\mu\text{-}OH)_2(\mu\text{-}4\text{-}Cl\text{-}pz)_{12}(4\text{-}Cl\text{-}pzH)_2](Et_3NHCl)$ (**19**) viewed with the 2-fold symmetry axis tilted counterclockwise; Et_3NH^+ and H atoms except (μ-OH) and (μ_3-OH) and (μ_3-$OH_{0.5}$) were omitted for simplicity. Fe_o, octahedral Fe; Fe_t, tetrahedral Fe.

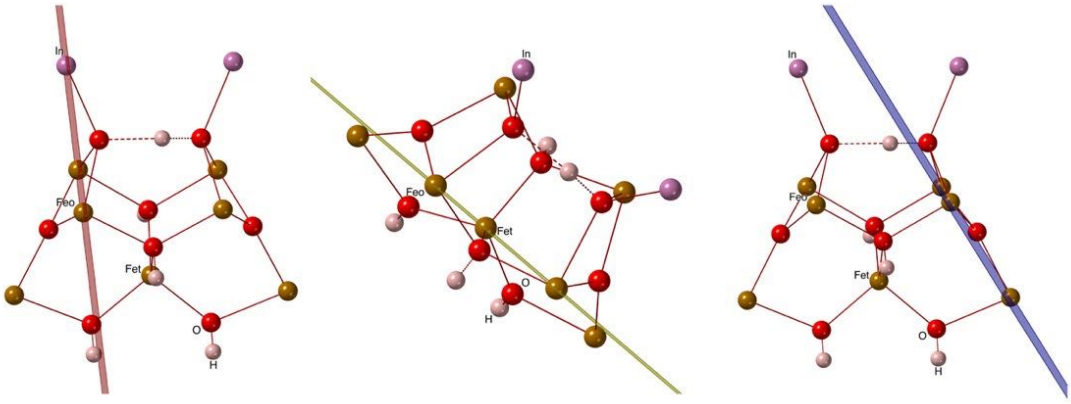

Figure 52. Ball-and-stick representation of torsion angles for (μ_3-$OH_{0.5}$), (μ_3-OH) and (μ_3-O) with respect to the corresponding plane where they sit (**19**).

3.3. Conclusions

Heterobimetallic pyrazolato oxide complexes of iron and indium with different nuclearities and properties can be achieved by reacting *mer*-[$InCl_3$(4-R-pzH)$_3$] (R = H, Cl, Br, I, Ph) and anhydrous $Fe(O_3SCF_3)_2$ or $Fe(ClO_4)_2{\cdot}6H_2O$ in MeCN or CH_2Cl_2 upon addition of piperidine or triethylamine. The hydrolysis of Fe^{3+} ions in these reactions is not controlled and several products can be formed. The average bulk composition of the reaction leading to complex **16** was analyzed by ESI-MS showing a mixture of different fragments of general form [$Fe_{8-x}In_xCl_4(\mu_4\text{-}O)_4(\mu\text{-}pz)_{12}$] where x = 0 – 4. Complex **16** with general formula [$(Fe_{0.64}In_{0.36})_4Fe_4Cl_4(\mu_4\text{-}O)_4(\mu\text{-}pz)_{12}$] was isolated and characterized by SCXRD and SEM-EDS. The percent of iron and indium in the mixture can be slightly different in each reaction product, with indium occupying only the outer sites. The fragments cannot be separated by chromatography of the filtrate; however, centrifuging the reaction bulk at 4500 rpm for 10 minutes have shown some separation of the precipitate form from the reaction into layers that can be distinguished by different shades of orange/red. The differently shaded precipitates have not been characterized, yet. Chemical separation of the fragments is to be explored. Complexes of general formula [$(In_{0.88}Fe_{0.12})_6Cl_6(\mu_3\text{-}OH_{0.5})(\mu\text{-}OH)_6(\mu\text{-}pz)_6]^{3-}$ (**17**) and [$(In_{0.92}Fe_{0.08})_6Cl_6(\mu_3\text{-}OH_{0.5})(\mu\text{-}OH)_6(\mu\text{-}4\text{-}I\text{-}pz)_6]^{3-}$ (**18**) were isolated. Complex **17** was characterized by SCXRD and SEM-EDS and complex **18** was characterized by SCXRD. The percent of iron in the clusters will vary slightly from batch to batch. Electrochemistry of complexes **17** and **18** is to be studied to measure any redox processes from the iron occupancy in the complexes, but first changing the counterion is necessary. The bond distances and angles of **17** and **18** are statistically indistinguishable from the analogous all-indium hexanuclear complexes.

The only heterobimetallic complex showing full occupancy of the metal sites $[Fe^{III}_7In_2Cl_4(\mu_3\text{-}O)_2(\mu_3\text{-}OH)_2(\mu_3\text{-}OH_{0.5})_2(\mu\text{-}OH)_2(\mu\text{-}4\text{-}Cl\text{-}pz)_{12}(4\text{-}Cl\text{-}pzH)_2](Et_3NH^+Cl^-)$ (**19**). The synthesis of complex **19** needs to be reproduced and optimized. ^{57}Fe-Mössbauer spectroscopy, magnetic susceptibility studies and additional characterization like UV-vis and ^{1}H NMR of the complex in solution needs to be performed.

3.4. Experimental section

3.4.1. Materials

Reagent grade chemicals were obtained from commercial sources and used as received. All solvents were stored over 4 Å molecular sieves. Anhydrous $InCl_3$ and anhydrous $Fe(O_3SCF_3)_2$ were stored and weighed in a glove box compartment under argon. $Fe(ClO_4)_2{\cdot}6H_2O$ was stored in a desiccator.

3.4.2. Instrumentation and X-ray crystallography

SEM-EDS were measured on JEOL JSM 5900LV with EDS-UTW detector at Florida International University. Mass spectrometry was measured by collaborators at Purdue University. The UV-vis spectra were recorded on an Agilent Technologies Cary 6000i Series UV-vis-NIR Spectrophotometer with 1 cm optical path length cuvettes in anhydrous MeCN solution. One single crystal was dissolved in 1mL MeCN, from which 200 µL were then diluted to a 2 mL MeCN solution.

Refer to section 2.7.4 for single crystal X-ray diffraction details.

3.4.3. Synthesis and characterization

3.4.3.1. Synthesis of $[(Fe_{0.64}In_{0.36})_4Fe_4Cl_4(\mu_4\text{-}O)_4(\mu\text{-}pz)_{12}]$ (16)

Piperidine (148.3 µL, 1.5 mmol) was added to a mixture of *mer*-$[InCl_3(pzH)_3]$ (211.9 mg, 0.5 mmol) and anhydrous $Fe(SO_3CF_3)_2$ (36.1 mg, 0.1 mmol) in 3 mL CH_2Cl_2.

The mixture was allowed to react for 24 hours. The mixture was filtered through celite and cotton. The filtrate was set to crystallize by slow diffusion with hexane. After 2 days, large slightly yellow X-ray quality crystals (not characterized here) and a red oil were obtained. The red oil was redissolved in MeCN and was allowed to slowly evaporate. Red X-ray quality crystals grew after 3 days. Yield: ~ 70%.

3.4.3.2. Synthesis of $(HNEt_3)_3[(In_{0.88}Fe_{0.12})_6Cl_6(\mu_3\text{-}OH_{0.5})(\mu\text{-}OH)_6(\mu\text{-}pz)_6]$ (17)

mer-$[InCl_3(pzH)_3]$ (127.14 mg, 0.3 mmol) was suspended in 3 mL MeCN under stirring. Anhydrous $Fe(SO_3CF_3)_2$ (35.4 mg, 0.1 mmol) were added to the suspension as well as triethylamine (41.7 µL, 0.3 mmol) and the mixture was allowed to react for 24 hours under stirring. A red precipitate formed and a red filtrate. The mixture was centrifuged at 4500 rpm for 10 min. The filtrate was left for crystallization by slow evaporation of the reaction solvent. Yellow X-ray quality crystals were obtained after 3 days. Some remaining red filtrate was separated from the crystals, and these were washed with MeOH, quickly decanting the methanolic washes, so there was no further reaction. Yield: ~ 25%.

3.4.3.3. Synthesis of $(HNEt_3)_3[(In_{0.92}Fe_{0.08})_6Cl_6(\mu_3\text{-}OH_{0.5})(\mu\text{-}OH)_6(\mu\text{-}4\text{-}I\text{-}pz)_6]$ (18)

Triethylamine (208.5 µL, 1.5 mmol) was added to a suspension of *mer*-$[InCl_3(4\text{-}I\text{-}pzH)_3]$ (400.9 mg, 0.5 mmol) and $Fe(ClO_4)_2{\cdot}6H_2O$ (46.38 mg, 0.17 mmol) in 3 mL CH_2Cl_2 under stirring. The mixture was allowed to react for 24 h. A red precipitate was formed and a red filtrate. The filtrate was left for crystallization by slow diffusion of Et_2O vapors. Slightly yellow X-ray quality crystals were obtained after 4 days. The crystals were washed with acetonitrile and Et_2O and air-dried. Yield: ~ 20%.

3.4.3.4. Synthesis of $[Fe^{III}_7In_2Cl_4(\mu_3\text{-}O)_2(\mu_3\text{-}OH)_2(\mu_3\text{-}OH_{0.5})_2(\mu\text{-}OH)_2(\mu\text{-}4\text{-}Cl\text{-}pz)_{12}(4\text{-}Cl\text{-}pzH)_2](Et_3NHCl)$ (19)

Triethylamine (208.5 µL, 1.5 mmol) was added to a mixture of *mer*-[$InCl_3$(4-Cl-pzH)$_3$] (792.2 mg, 1.5 mmol) and $Fe(ClO_4)_2{\cdot}6H_2O$ (136.4 mg, 0.5 mmol) in 6 mL CH_2Cl_2 under stirring. The reaction was allowed to stir for 5 days, and a clear red solution was obtained. The solution was filtered through cotton/celite and crystallized by slow diffusion of hexane was done. Dark red X-ray grade crystals were obtained after 9 days. (Not reproducible yet). Yield: < 5%.

Table 15. Structure refinement parameters for complexes **16 – 19**.

Compound	**16**	**17**	**18**	**19**
Empirical formula	$C_{36}H_{36}Cl_4Fe_{6.57}In_{1.44}N_{24}O_4$	$C_{41}H_{74}Cl_6Fe_{0.7}In_{5.3}N_{15}O_8$	$C_{36}H_{73}Cl_6Fe_{0.5}I_6In_{5.5}N_{15}O_8$	$C_{54}H_{66}Cl_{18}Fe_7In_2N_{30}O_8$
Formula weight	1542.11	1803.5	2468.46	2522.05
Temperature/K	296	296	299	170
Crystal system	triclinic	Monoclinic	trigonal	tetragonal
Space group	*P*-1 (No. 2)	$P2_1/c$ (No. 14)	*R*-3 (No. 148)	$P4_32_12$ (No. 96)
a/Å	12.4514(4)	19.8363(11)	20.3811(3)	15.1365(8)
b/Å	12.5773(4)	19.3424(11)	20.3811(3)	15.1365(8)
c/Å	20.9797(8)	17.7967(10)	32.2936(8)	48.278(4)
α/°	77.8280(10)	90	90	90
β/°	81.5020(10)	90	90	90
γ/°	70.6360(10)	90	120	90
Volume/Å^3	3019.17(18)	6828.3(7)	11617.2(4)	11061.2(14)
Z	2	4	3	4
ρ_{calc}g/cm^3	1.696	1.754	2.116	1.514
μ/mm^1	2.301	2.199	4.346	1.787
Ref. Coll./Indp. Ref.	56823/12244	68821/8353	70355/5295	293153/13810
R_{int} /R_σ	0.038/0.1066	0.0623/0.1261	0.0304/0.0474	0.0827/0.610
Θ_{max}/ % completn.	27.843/0.998	25.375/0.665	26.396/0.999	28.356/0.998
T_{min}/T_{max}	0.548/0.797		0.517/0.658	0.747/0.808
Param./[a]Obsv. Ref.	690/8300	817/6003	487/4586	537/13399
[b]GooF	1.066	1.079	1.043	1.092
[c]wR_2	0.1278	0.2444	0.0864	0.1397
[d]R_1	0.0592	0.0851	0.0391	0.0570
Flack Parameter				0.089(5)

[a] $I_o > 2\sigma(I_o)$

[b] GooF = $[\Sigma[w(F_o^2-F_c^2)^2]/(N_o-N_v)]^{1/2}$ (N_o=*number of observations*, N_v=*number of variables*)

[c] wR_2 = $\Sigma||F_o|-|F_c||/\Sigma|F_o|$

[d] R_1 = $[(\Sigma w(F_o^2-F_c^2)^2/\Sigma|F_o|^2)]^{1/2}$

Chapter 4: Synthesis and characterization of homometallic oxide complexes

4. Synthesis of homometallic oxide complexes

4.1. Introduction

Multinuclear metal complexes are of interest as building blocks for magnetic molecular materials and models of metalloproteins.[107] Multinuclear metal models provide an insight into the metalloproteins active site geometries, electronic structures, and reaction mechanisms, including catalytic activity.[108]

In Nature, water oxidation is catalyzed by the oxygen evolving complex (OEC) with a Mn_4CaO_5– cluster in the active site (Figure 3). Water oxidation is regarded as the main strategy for production and storage of energy. Iron plays a critical role in biological systems, shows low toxicity and clusters are promising for redox reactions.[109] Iron-based water oxidation catalysts remain of interest. However, improving the synthetic methods to prepare high nuclearity Fe^{3+} containing clusters that can be studied in solution and act as efficient catalyst remains a challenge. Several pentanuclear iron clusters that act as catalysts for water oxidation have been reported but are either not stable during the catalytic process or exhibit low turnover frequency.[109–111]

Additionally, lanthanide – iron clusters have potential applications in optics, magnetism, catalysis, and chirality.[112] These clusters usually show interesting magnetic properties including single molecule magnetism and spin-crossover.[113,114] Controlling the hydrolysis of Fe^{3+} ions is a key step in the preparation of such complexes. It is also difficult to prepare *3d – 4f* complexes due to the different coordination preferences of *3d* and *4f* metal ions.[113]

4.2. Results and Discussion

4.2.1. Synthesis of $[Fe_5Cl_3(\mu_4\text{-}O)(\mu_3\text{-}O)(\mu\text{-}OH)_2(\mu\text{-}4\text{-}I\text{-}pz)_6(4\text{-}I\text{-}pzH)_4]\cdot(Et_2O)$ (20)

Complex **20** of formula $[Fe_5Cl_3(\mu_4\text{-}O)(\mu_3\text{-}O)(\mu\text{-}OH)_2(\mu\text{-}4\text{-}I\text{-}pz)_6(4\text{-}I\text{-}pzH)_4]\cdot(Et_2O)$ was prepared by adding triethylamine to a suspension of *mer*-$[InCl_3(4\text{-}I\text{-}pzH)_3]$ and $Fe(ClO_4)_2\cdot 6H_2O$ in CH_2Cl_2 (Scheme 10). A precipitate formed after 48 hours, and it was thoroughly washed with CH_2Cl_2 to reveal an off-white color. The precipitate was collected and dried in a desiccator. Once dry, the precipitate was redissolved in MeCN and a red solution developed gradually over 72 h, along with a small amount of red precipitate. The solution was filtered and left for crystallization by slow diffusion of diethyl ether vapors. Dark red crystals grew after 7 days. The crystals were washed with ether and were collected. Several efforts to improve the reaction yield showed that this reaction only worked using *mer*-$[InCl_3(4\text{-}I\text{-}pzH)_3]$ as pyrazole source and crystallization was only successful with $MeCN/Et_2O$.

4.2.2. Crystallographic description of $[Fe^{III}_5Cl_3(\mu_4\text{-}O)(\mu_3\text{-}O)(\mu\text{-}OH)_2(\mu\text{-}4\text{-}I\text{-}pz)_6(4\text{-}I\text{-}pzH)_4]\cdot(Et_2O)$ (20)

Complex **20** of general formula $[Fe_5Cl_3(\mu_4\text{-}O)(\mu_3\text{-}O)(\mu\text{-}OH)_2(\mu\text{-}4\text{-}I\text{-}pz)_6(4\text{-}I\text{-}pzH)_4]\cdot(Et_2O)$ crystallizes in the orthorhombic $P2_12_12_1$ space group (Figure 53). Two iron centers have the same six-coordinate pseudooctahedral environment consisting of two bridging pyrazolato ligands, one pyrazole ligand, one μ-OH, one μ_3-O, and one μ_4-O in a *fac*-N_3O_3 arrangement. The other three iron centers are all in different pseudooctahedral coordination environments; one is coordinating to a terminal chloride ligand, a μ_3-O, two bridging pyrazolato ligands, and two pyrazoles in a *trans*-N_4OCl arrangement, a second one to two bridging pyrazolato ligands, one terminal chloride, two μ-OH, and a μ_4-O in a

fac-O_3N_2Cl arrangement, and the third one is coordinating to four bridging pyrazolato ligands, one terminal chloride ligand, and a μ_4-O in a *trans*-N_4OCl arrangement. There is one Et_2O molecule in the unit cell H-bonded to a pyrazole ligand. The pyrazole ligands are free to rotate and form intramolecular H-bonding with chlorine and oxygen atoms (Figure 54). The molecule is chiral and crystallizes as a racemic twin with a Flack parameter of 0.510(9) (Table 22). The crystal structure is unique and shows not only an 'incomplete' Fe – O cubane core (Fe1, Fe2, and Fe3) but also an iron trimer (Fe2, Fe3, and Fe4) bridged by two pyrazolato ligands, a μ_3-O, and a μ_4-O (Figure 54), and two bridging hydroxo groups, which is different from previously reported pentanuclear iron clusters including some with pyrazolato-based ligands[107,109–111,115] (Figure 55).

The structure has crystallographic disorder of the hydrogen atoms and the pyrazoles and needs to be collected at low temperature. The bond distance for Fe1 – Cl is 2.23(3) Å, and the average bond distances for Fe_p – Cl are 2.30(3) – 2.34(2) Å which are larger than for the core iron atom (Table 16). The average bond distances for Fe_c – (Npz^*) (pz^* = 4-I-pz), are between 2.04(2) – 2.21(1) Å and for Fe_p – (Npz^*) are between 1.91(1) – 2.23(3) Å, which are statistically shorter than for the iron atoms in the 'incomplete' cubane core. The average bond distances for Fe_c – (Npz^*H) (pz^* = 4-I-pzH), are between 2.04(5) – 2.17(3) Å and for Fe_p – (Npz^*H) are between 2.07(1) – 2.24(5) Å. Only the iron in the core of the 'incomplete' cubane structure (Fe1, Fe2, and Fe3) are bridged by μ-OH and the average bond distance for Fe_c – (μ-OH) are between 2.11(3) – 2.23(3) Å. The average bond distances for Fe_c – (μ_3-O) are 1.91(1) Å and 2.01(2) Å, which are statistically longer than for the Fe4 – (μ_3-O) bond distance of 1.86(3) Å. Lastly, the average bond distances for Fe_c

– (μ_4-O) are between 2.02(2) Å – 2.08(3) Å, which are statistically longer than for the Fe5 – (μ_4-O) bond distance of 1.94(3) Å.

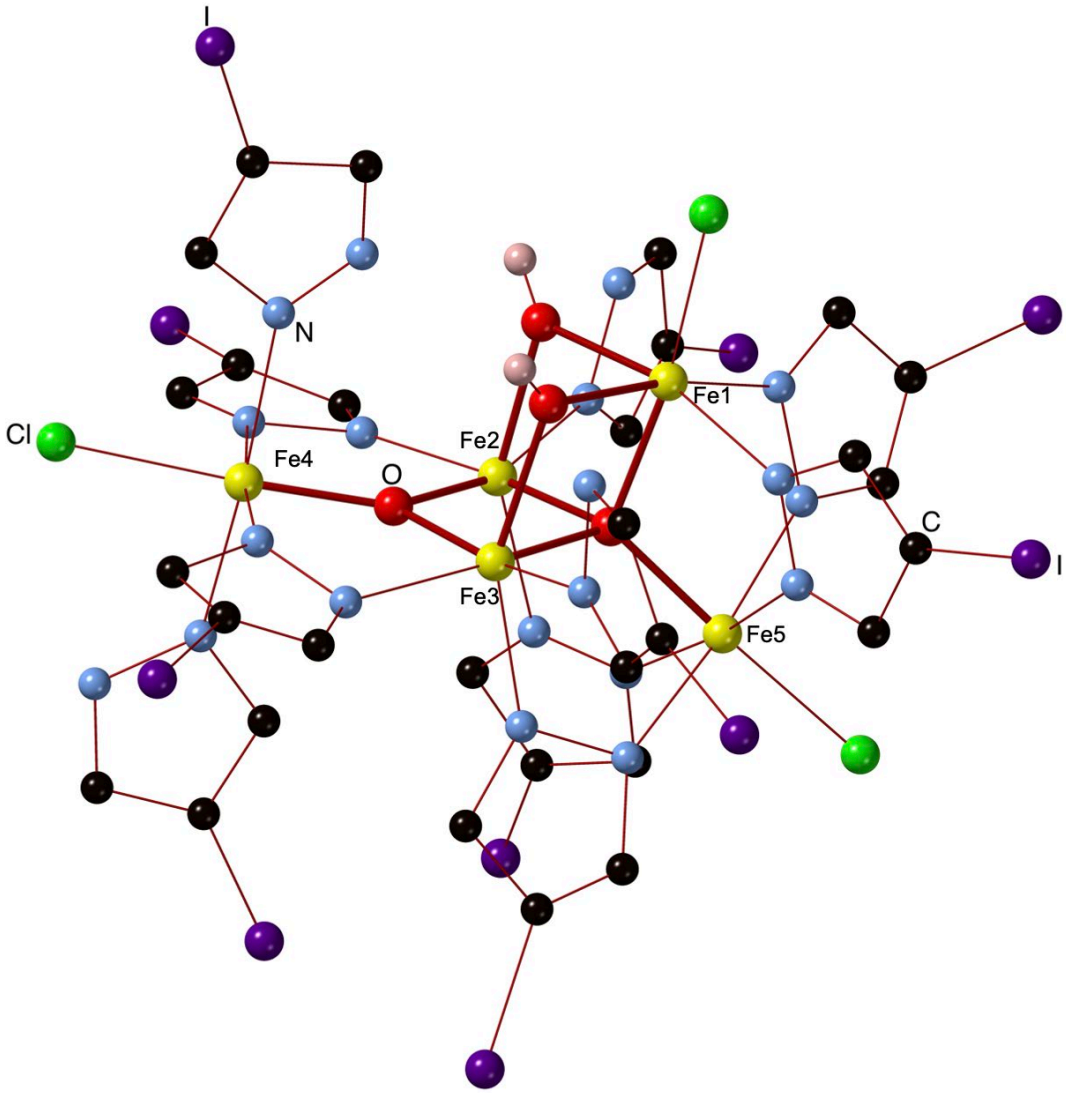

Figure 53. Ball-and-stick representation of [$Fe_5Cl_3(\mu_4\text{-}O)(\mu_3\text{-}O)(\mu\text{-}OH)_2(\mu\text{-}4\text{-}I\text{-}pz)_6(4\text{-}I\text{-}pzH)_4$] (**20**) with labeled Fe centers (Fe1, Fe2, and Fe3 = Fe_c; Fe4 and Fe5 = Fe_p). Solvent molecules and H's atoms have been omitted for simplicity except for the (μ-OH).

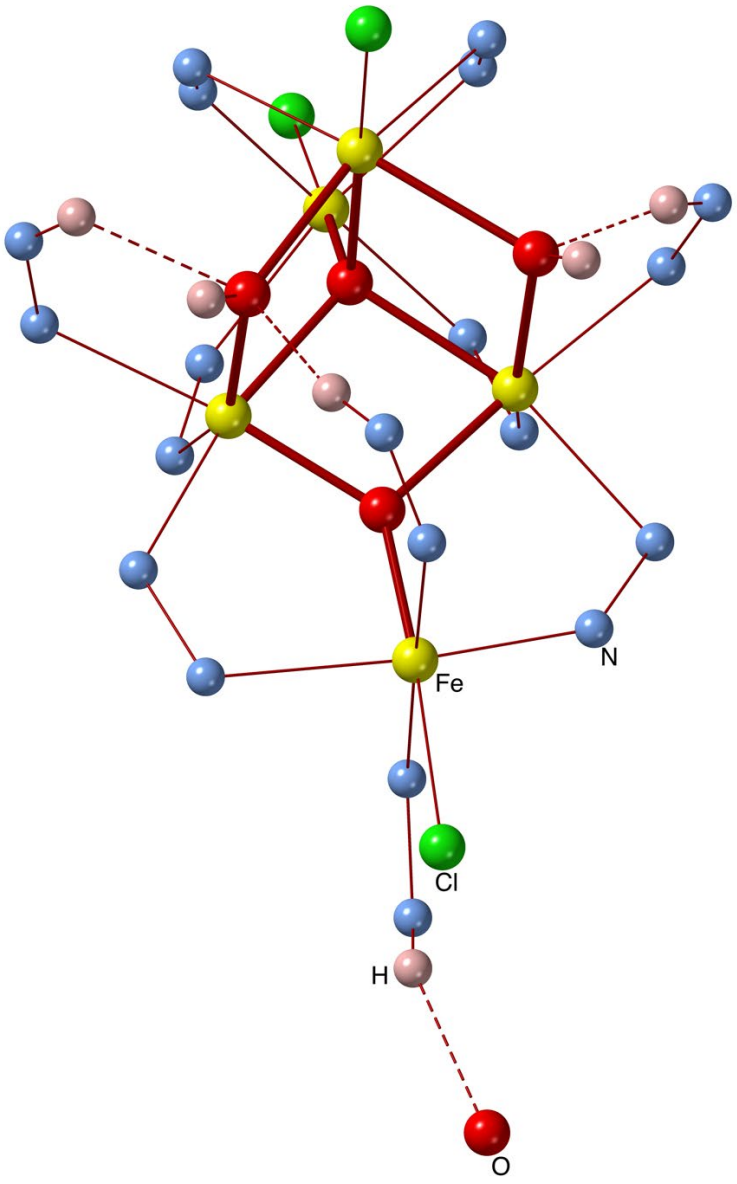

Figure 54. Ball-and-stick representation of the core structure of [$Fe_5Cl_3(\mu_4\text{-}O)(\mu_3\text{-}O)(\mu\text{-}OH)_2(\mu\text{-}4\text{-}I\text{-}pz)_6(4\text{-}I\text{-}pzH)_4$] (**20**), showing the 'incomplete' cubane and iron trimer, as well as the hydrogen bonding interactions.

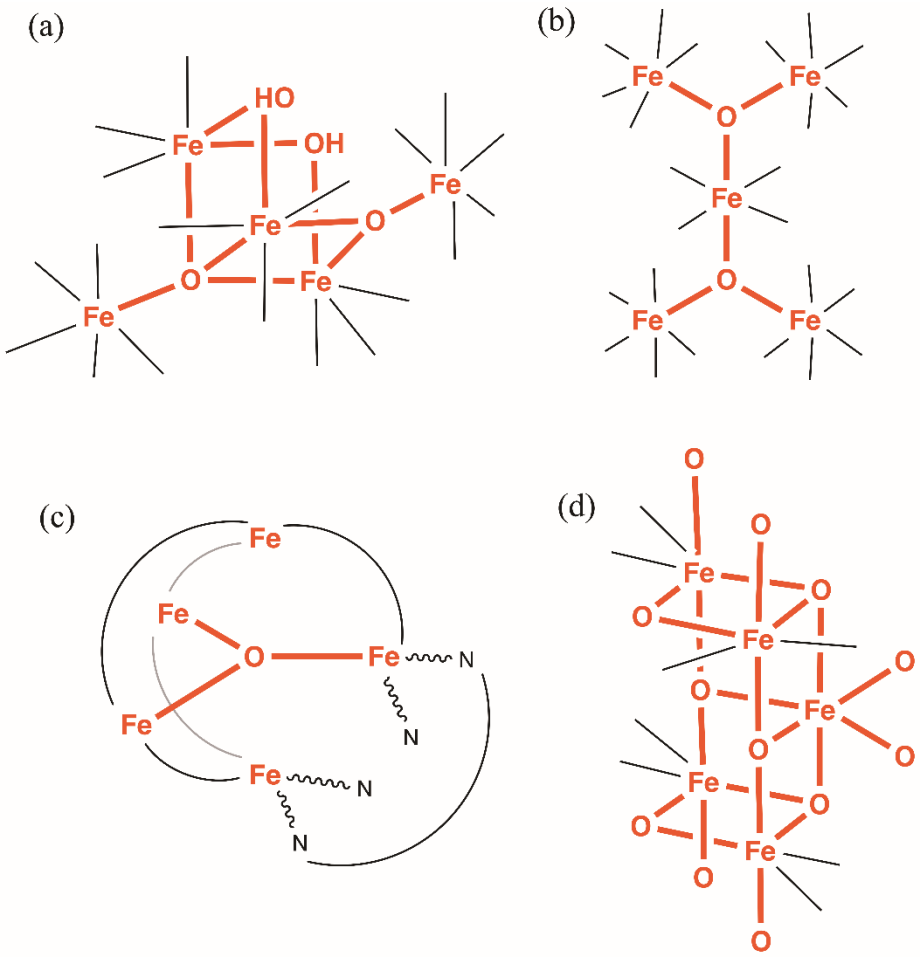

Figure 55. Schematic representation of pentanuclear iron clusters; (a) **20**, (b) ionic pentanuclear iron cluster[115], (c) clusters with pyrazolato-based ligands showing water catalysis,[109–111] and (d) pentanuclear iron cluster with defective double cubane[107].

Table 16. Selected bond lengths (Å) for **20**.

Interatomic Distances	**20**	**Interatomic Distances**	**20**
Fe_p – Cl	2.30(3) – 2.34(2)	Fe1 – Cl	2.23(3)
Fe_p – (Npz^*)	1.91(1) – 2.23(3)	Fe_c – (Npz^*)	2.04(2) – 2.21(1)
Fe_p – (Npz^*H)	2.07(1) – 2.24(5)	Fe_c – (Npz^*H)	2.04(5) – 2.17(3)
Fe4 – (μ_3-O)	1.86(3)	Fe_c – (μ_3-O)	1.91(1) – 2.01(2)
Fe5 – (μ_4-O)	1.94(3)	Fe_c – (μ_4-O)	2.02(2) – 2.08(3)
(Fe_p ··· Fe_c)[a]	3.35(1) – 3.47(1)	Fe_c – (μ-OH)	2.11(3) – 2.23(3)
(Fe4 ··· Fe1)	5.34(1)	Fe_c ··· Fe_c	3.00(1) – 3.15(1)

Fe_c = Fe cubane core, Fe_p = Fe peripheral sites
pz^*H = 4-I-pzH, [a]Fe_p – O – Fe_c (short)

Table 17. Selected bond angles (°) for **20**.

Angle	20
Fe_c – (μ-OH) – Fe_c	90.72(5) – 96.22(2)
Fe_c – (μ_3-O) – Fe_c	99.75(1)
Fe_p – (μ_3-O) – Fe_c	126.34(1) – 133.66(2)
Fe_c – (μ_4-O) – Fe_c	99.40(1) – 102.02(4)
Fe_p – (μ_4-O) – Fe_c	114.96(1) – 122.38(4)

Fe_c = Fe cubane core, Fe_p = Fe peripheral sites

Halogen ··· halogen interactions give rise to tight packing for **20**, exhibiting a type II, R – X ···Y – R contact interaction (X, Y = halogen atoms) (Table 18 and Figure 56). Complex **20** shows I1 ··· I2 average bond distance, C – I1 ··· I2 bond angle, and I1 ··· I2 – C bond angle equal to 3.14(4) – 3.38(3) Å, 176.88(5) – 178.38(4)°, and 88.16(1) – 94.32(5)°, respectively. Additionally, there is halogen ··· halogen interaction from I3 ··· I4 with average bond distance, C – I4 ··· I3 bond angle, and I4 ··· I3 – C bond angle equal to 3.20(1) – 3.45(2) Å, 169.24(4) – 177.19(4)°, and 87.89(5) – 93.23(3)°, respectively from a bridging 4-I-pyrazolato ligand to another pyrazolato ligand in the adjacent cluster, resulting in a 3D network depicted in the crystal packing diagram in Figure 56.

Table 18. Halogen ··· halogen bond geometry for **20** *vs.* sum of van der Waals radii.

Sum van der Waals radii/Å[58]	A – X – Y	d(X – Y)/Å	A – X – Y/°
3.96	C – I2 ··· I1 (θ_1)	3.14(4) – 3.37(3)	88.16(1) – 94.32(5)
	I2 ··· I1 – C (θ_2)		176.88(5) – 178.38(4)
	C – I3 ··· I4 (θ_1)	3.20(1) – 3.45(2)	87.89(5) – 93.23(3)
	I3 ··· I4 – C(θ_2)		169.24(4) – 177.19(4)

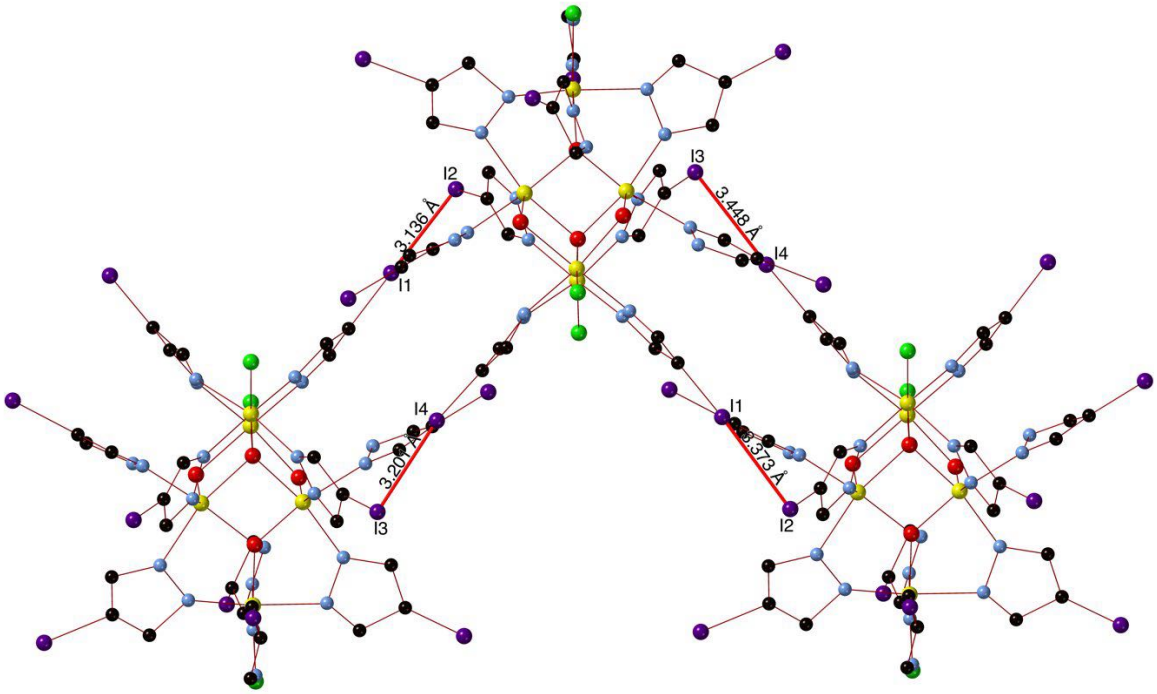

Figure 56. Illustration of crystal packing for **20**, showing a 3D chain linked by intermolecular halogen bonding.

4.2.3. ^{1}H NMR of $[Fe_5Cl_3(\mu_4\text{-}O)(\mu_3\text{-}O)(\mu\text{-}OH)_2(\mu\text{-}4\text{-}I\text{-}pz)_6(4\text{-}I\text{-}pzH)_4]\cdot(Et_2O)$ (20)

The ^{1}H NMR was done using the Evans method in DMSO-*d*$_6$ at ambient temperature at 400 MHz. There are six different pyrazole/pyrazolato ligands environments in complex **20** (Figure 57). The expected ^{1}H NMR should show resonances corresponding to six different magnetic environments of the μ-4-I-pz and 4-I-pzH groups. However, the ^{1}H NMR of complex **20** is paramagnetic, therefore some of the pyrazole/pyrazolato resonances are broadened/flattened and not observed (Figure 58). The ^{1}H NMR shows a small broad singlet at 13.2039 ppm corresponding to the NH peak, a singlet at 7.9693 ppm and a singlet at 7.5827 corresponding to $H^{3,5}$ all with the same integration. No firm assignment of these resonances can be made without additional data.

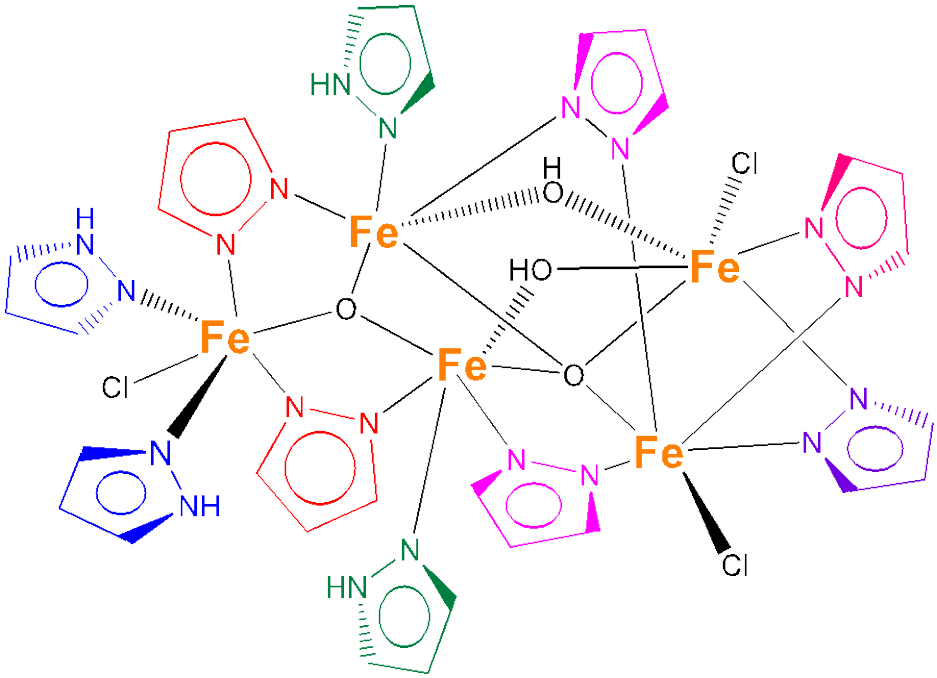

Figure 57. Schematic representation of **20** highlighting in different colors the six different pyrazole/pyrazolato environments.

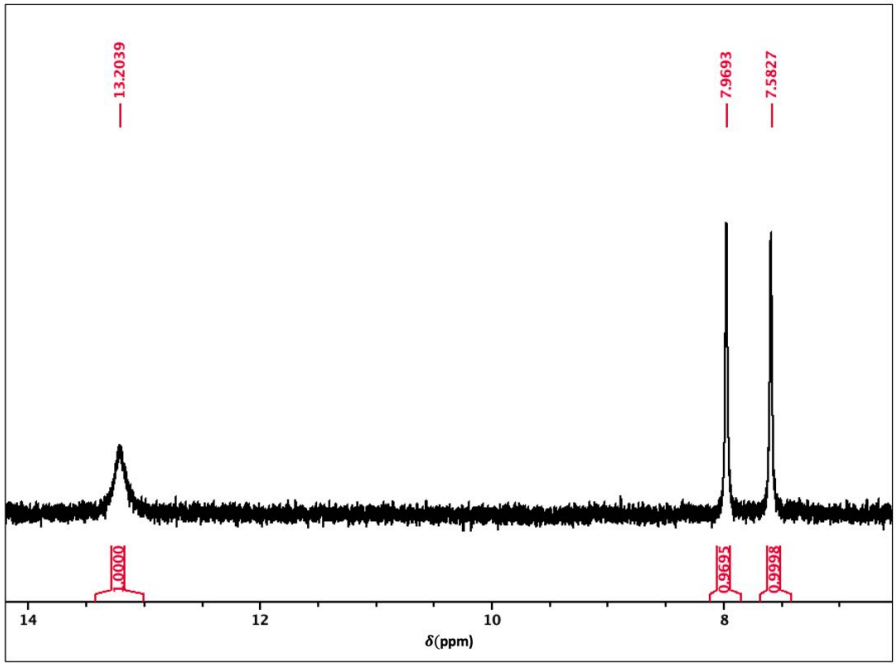

Figure 58. ^{1}H NMR of **20** in DMSO-d_6 at 400 MHz and ambient temperature.

4.2.4. Electrochemistry of $[Fe_5Cl_3(\mu_4\text{-}O)(\mu_3\text{-}O)(\mu\text{-}OH)_2(\mu\text{-}4\text{-}I\text{-}pz)_6(4\text{-}I\text{-}pzH)_4]\cdot(Et_2O)$ (20)

The previously reported pentanuclear iron catalysts for water oxidation have $[Fe^{II}_4Fe^{III}]$ oxidation states and show four reversible one-electron oxidations and one reduction or have $[Fe^{III}_5]$ showing five reversible one-electron oxidations.[109–111] The cyclic voltammogram (CV) of complex **20** (0.1 mM) in a tetrahydrofuran (THF) containing Et_4NClO_4 (0.1 M) at a scan rate of 50 mV s^{-1} (Figure 59) shows two reversible (Table 19) reduction waves at $E_{1/2}$ = -0.55 V and -0.83 V (corrected *vs*. Fc^+/Fc), assigned to two sequentially occurring reductions involving Fe^{III}/Fe^{II} and one reversible oxidation wave at $E_{1/2}$ = -0.04 V (corrected *vs*. Fc^+/Fc) on involving in turn an iron ion Fe^{IV}/Fe^{III} couple. There is an additional small signal at -0.04 V, but it cannot be assigned with certainty. Thus, complex **20** possesses high redox flexibility, with at least three different redox states that are accessible under electrochemical conditions.

Table 19. Electrochemical properties of complex **20** taken from CV displayed in Figure 59 (corrected *vs.* Fc^+/Fc)

Redox process	E_{ox} (V)	E_{red} (V)	$E_{1/2}$ (V)	ΔE (V)
I	0.01	-0.07	-0.04	0.06
II	-0.50	-0.59	-0.55	0.09
III	-0.77	-0.88	-0.83	0.11

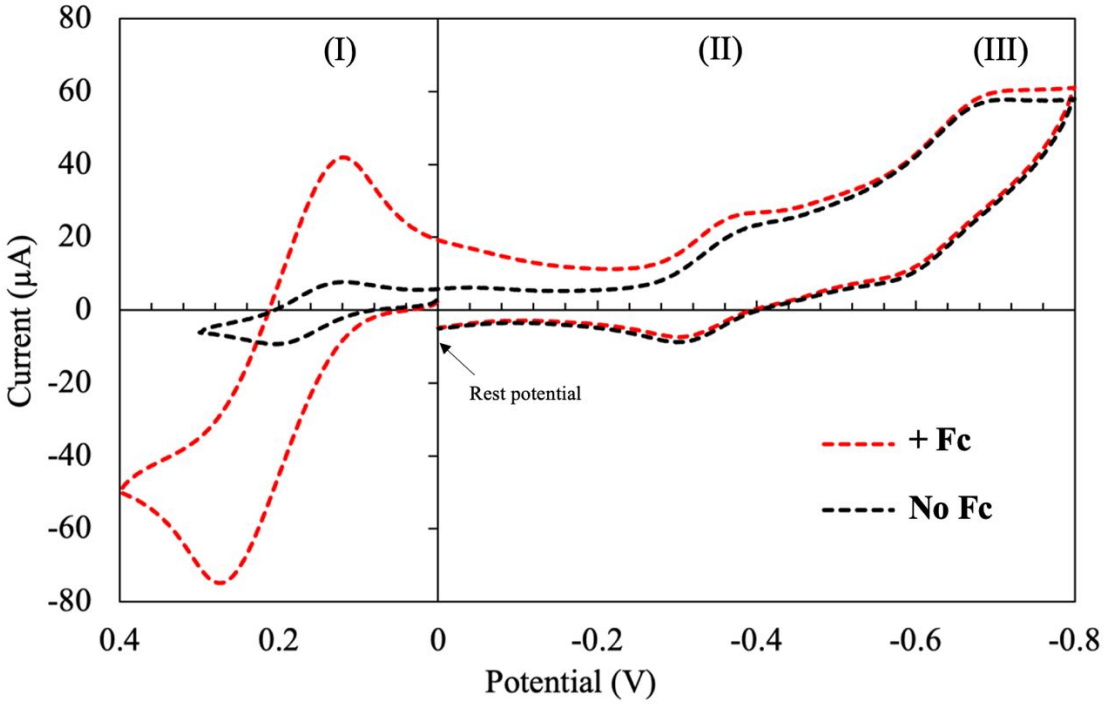

Figure 59. CV of **20** (0.1 mM) with and without Fc in THF solution with Et_4NClO_4 (0.1 M) swept to negative (right) and positive (left) potentials from the open circuit potential at a scan rate of 50 mV s^{-1}. Redox processes are number: I, II, and III.

Cyclic voltammogram at increasing scan rates was collected as well (Figure 60), where the current is increasing linearly as a function of the square of the scan rate (Figure 61) for all three reversible electron transfer processes. The differential pulse voltammogram (DPV) was measured to minimize the effect of the charging current and achieve higher sensitivity (Figure 62). The DPV shows symmetric peaks characteristic of reversible reactions and E_p = 0.18 V, -0.33 V, and -0.62 V, respectively for redox process I, II, and III. The square wave voltammogram (SWV) was also measured for higher sensitivity results showing the reversible, irreversible, and net current redox processes consistent with the results from CV and DPV (Figure 63). Since complex **20** contains five redox active iron centers, it is of interest to distinguish whether the redox events are a one-

electron process taking place at a single Fe-center, or a two-electron process occurring at two electronically uncoupled Fe-centers undergoing a reversible Fe(III/II) reduction. However, the number of electrons involved in the redox processes is not evident from the electrochemical data collected. Further electrochemical analysis needs to be performed.

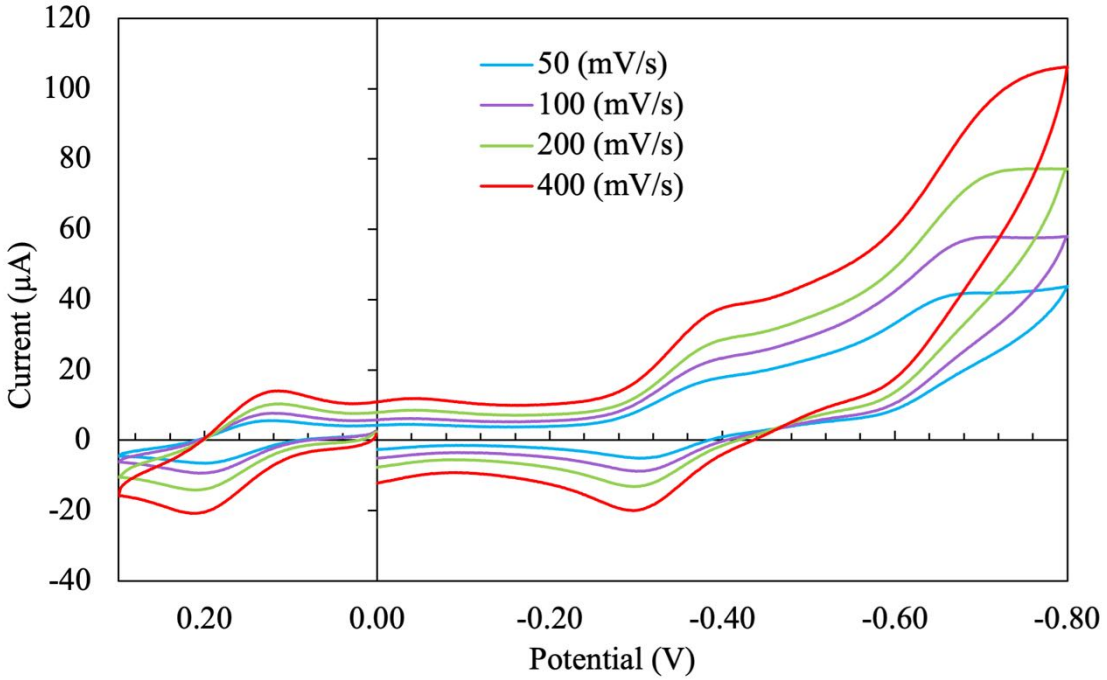

Figure 60. CV of **20** (0.1 mM) in a THF solution with Et_4NClO_4 (0.1 M) at scan rates of 50 – 400 mV s^{-1}.

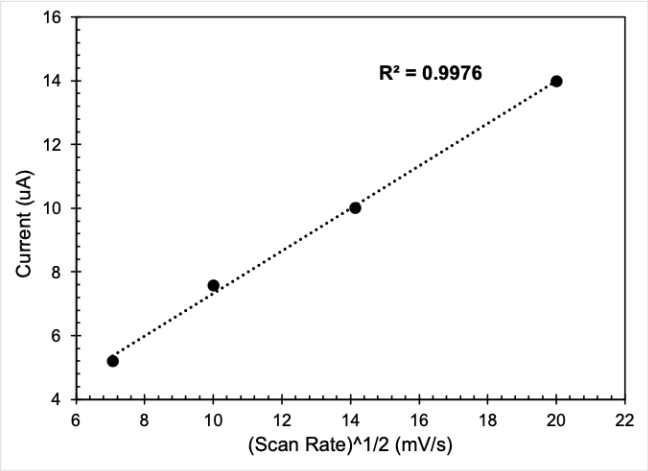

(I)

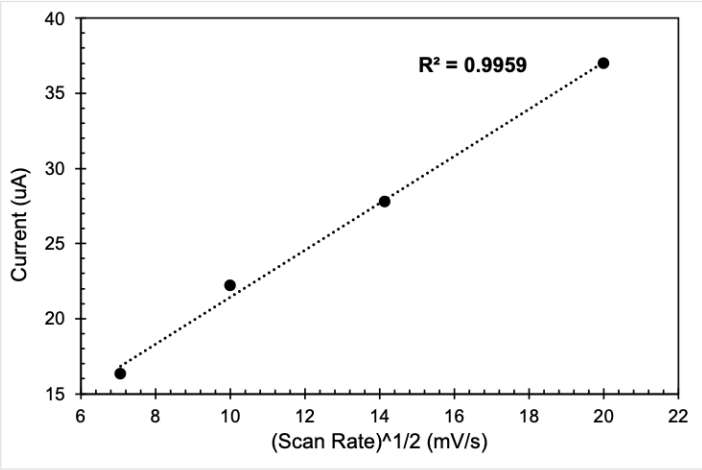

(II)

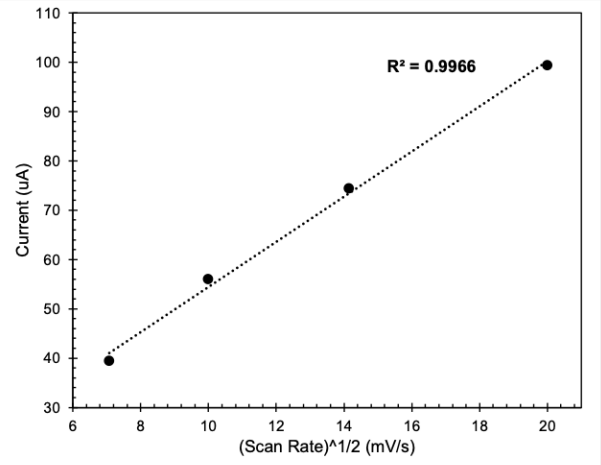

(III)

Figure 61. Current as a function of the square of the scan rate for all redox processes observed for **20** taken from Figure 60.

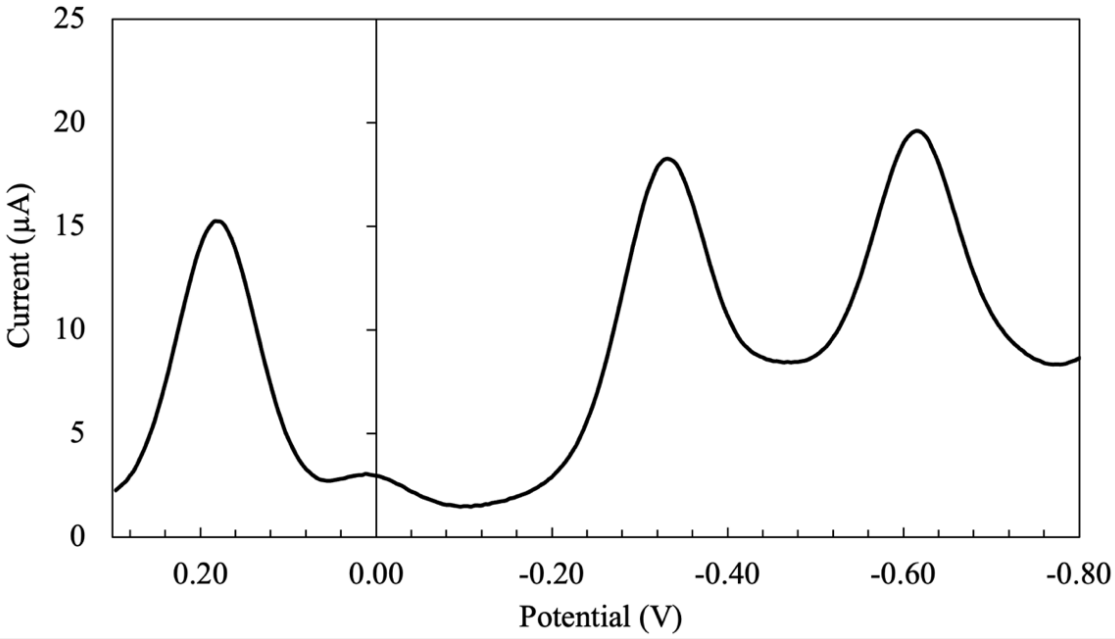

Figure 62. DPV of **20** (0.1 mM) in a THF solution with Et_4NClO_4 (0.1 M).

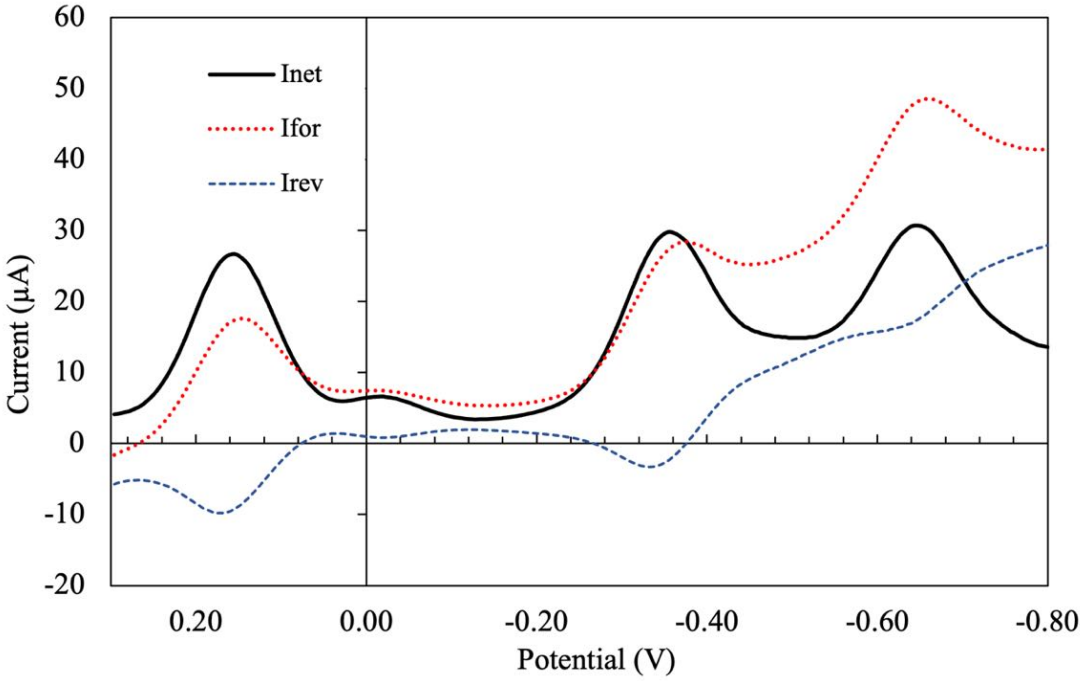

Figure 63. SWV of **20** (0.1 mM) in a THF solution with Et_4NClO_4 (0.1 M) swept forward to negative (red) and reverse to positive (blue) potentials.

4.2.5. UV-vis absorption of $[Fe_5Cl_3(\mu_4\text{-}O)(\mu_3\text{-}O)(\mu\text{-}OH)_2(\mu\text{-}4\text{-}I\text{-}pz)_6(4\text{-}I\text{-}pzH)_4]\cdot(Et_2O)$ (20)

The UV-vis spectra were recorded on an Agilent Technologies Cary 6000i Series UV-vis-NIR Spectrophotometer with 1 cm optical path length cuvettes in a dry THF solution from 200 – 800 nm. The UV-visible absorption spectra of complex **20** (Figure 64) consists of overlapping bands in the whole 200 – 600 nm range with absorption maxima at 220 nm, 318 nm, and 428 nm, which have not been assigned yet. Unstructured absorption around 420 nm is characteristic for the formation of [FeS]-clusters and corresponds to the LMCT from cysteine to Fe^{2+} in ferredoxins.[9,116]

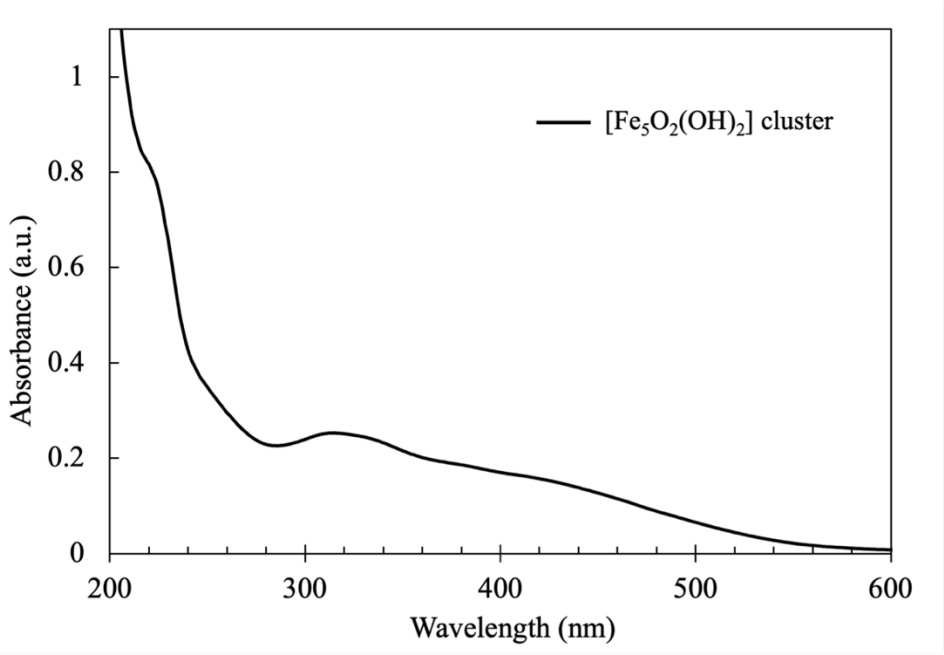

Figure 64. UV-visible spectrum of **20** in THF solution from 200 – 600 nm.

4.2.6. Synthesis of Fe(II)-intermediate (21)

An off-white powder (**21**) is formed as an intermediate in the synthesis of complex **20** (Scheme 10). The powder was thoroughly washed with CH_2Cl_2 until no color came off in the filtrate. The powder was left to dry in a desiccator. The powder must be kept under

vacuum or argon to store -- if left exposed to air, it turns orange after a couple of weeks -- oxidation is occurring. When the powder is introduced to any organic solvent, except for CH_2Cl_2, it immediately dissolves and solutions turns red or orange signaling the formation of other complexes as indicated by the ^1H NMR (Figure A13 -Figure A15). However, attempts at crystallization of the solutions with other solvents have not been successful. The off-white color of the powder, color change in open atmosphere, and rapid color change in solution suggests that there is a Fe^{2+} low-spin species.

4.2.7. SEM-EDS of Fe(II)-intermediate (21)

The off-white Fe(II)-intermediate powder (**21**) obtained from the reaction of **20** was analyzed through SEM at 15kV (Figure 65). The powder was homogenous around 100 µm in size. The sample was subjected to EDS measurement where the elemental composition (Figure 66) and weight concentration was determined (Table 20). The assignment of the EDS spectrum account to a total of 100% weight of the sample. The results showed that indium was not present in the sample -- all indium stayed in the CH_2Cl_2 solution. The Fe-intermediate consists of Fe, Cl, I, O, C, and N. Given the amount of iodide present in complex **20** which can only be from 4-I-pzH, we can assume some iron-chloride species forms and stays in solution after crystallization and isolation of **20**.

Table 20. EDS showing elemental composition and weight of **21**.

Element Name	Element Symbol	Mass (%)	Atom (%)	abs. error (%) (1σ)
Carbon	C	29.21	45.84	1.42
Nitrogen	N	23.61	31.77	1.20
Oxygen	O	10.28	12.11	0.52
Chlorine	Cl	4.56	2.42	0.12
Iron	Fe	16.10	5.43	0.41
Iodine	I	16.24	2.41	0.42
	Sum	**100.00**	**100.00**	

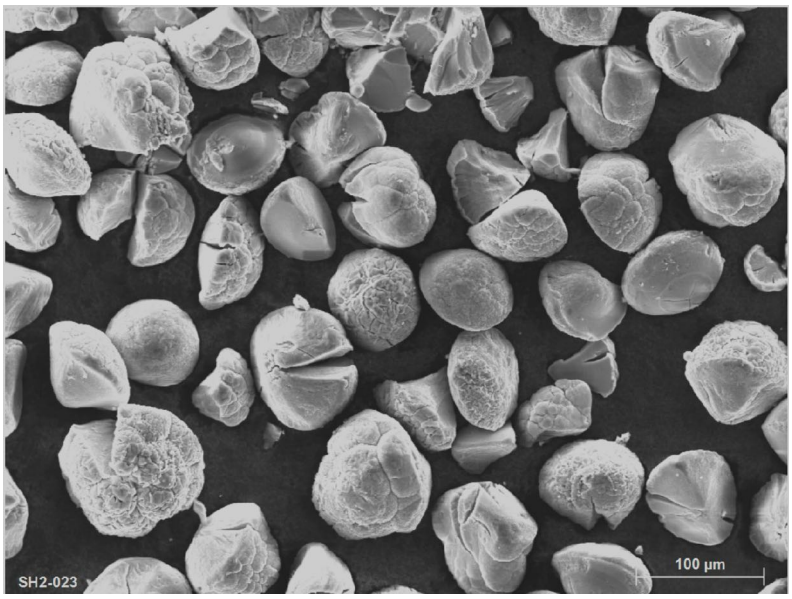

Figure 65. SEM image of **21**.

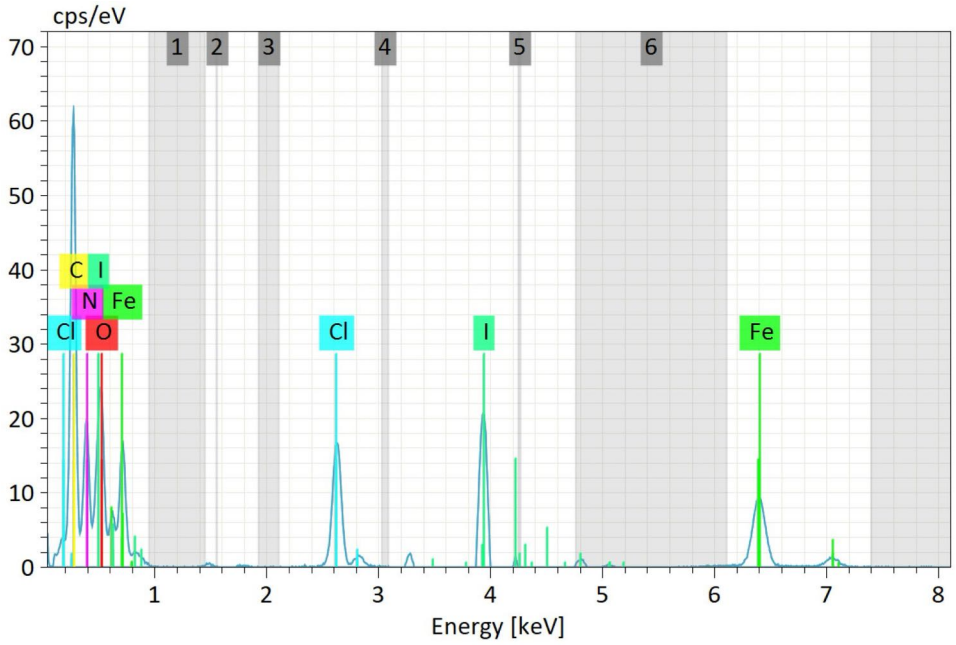

Figure 66. EDS image representing the elemental composition of **21**.

4.2.8. FTIR of Fe(II)-intermediate (21)

The FTIR spectrum of **21** was collected in the 4000 – 400 cm^{-1} range (Figure 67). Most peaks in the spectrum are conserved from the free 4-I-pzH (Figure A11) but have slightly shifted. The peaks at 3471 cm^{-1}, 3398 cm^{-1} correspond to O – H stretching

frequencies and the medium broad peaks at 3280 cm^{-1}, and 3118 cm^{-1} correspond to N – H stretching, which are higher than for free 4-I-pzH. The pyrazole ring overtones are observed at 1626 cm^{-1} and 1512 cm^{-1}, which is also consistent with the free 4-I-pzH spectrum. The ring stretching modes shifts to slightly higher wavenumbers in **21** to 1458 cm^{-1}, 1373 cm^{-1}, and 1334 cm^{-1}, while the C – H bending mode are observed at the lower wavenumbers of 1259 cm^{-1} and 1128 cm^{-1}. Ring bending modes are observed at 1178 cm^{-1}, and the shoulders under the sharp peaks at 1043 cm^{-1} and 935 cm^{-1}. The out-of-plane C – H bending mode at 729 cm^{-1} and 698 cm^{-1} and C – I bond at 600 cm^{-1} have shifted slightly to lower wavenumbers compare to free 4-I-pzH. Both strong peaks at 1043 cm^{-1} and 935 cm^{-1} do not show in the spectrum for free 4-I-pzH. The approximate frequency of bands for coordinated C_{2v} bidentate ClO_4 are observed at 930 cm^{-1} and 1100 cm^{-1}.[117]

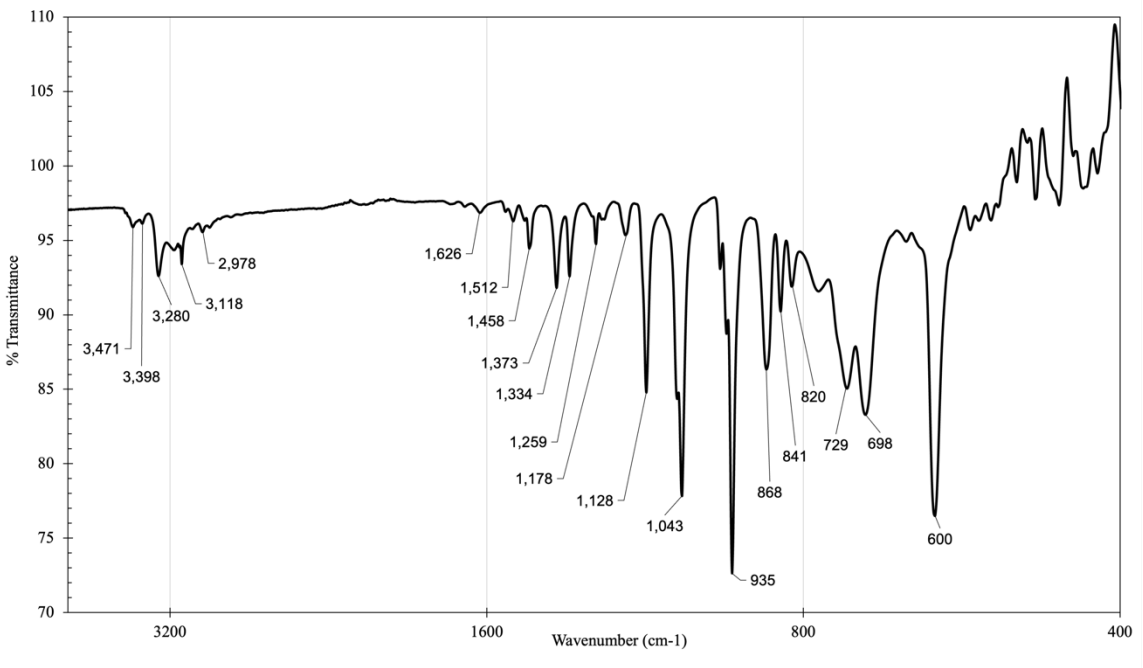

Figure 67. FTIR spectrum of **21**.

4.2.9. Synthesis and crystallographic description of $(HNEt_3)_2[Fe_6Cl_2(\mu_3\text{-}O)_2(\mu\text{-}OH)_4(\mu\text{-}4\text{-}Cl\text{-}pz)_{10}]$ (22)

Lanthanide – iron clusters are of interest due to the potential applications in various research field and based on the crystal radii of lanthanide ions, $[Fe_{8-x}Ln_xO_4]$ – clusters should be possible to obtain by similar synthetic methods employed to obtained $[Fe_{8-x}In_xO_4]$ – clusters. However, controlling the nuclearity of *3d – 4f* clusters and their coordination preferences is a challenge.

Complex **22** with formula $(HNEt_3)_2[Fe_6Cl_2(\mu_3\text{-}O)_2(\mu\text{-}OH)_4(\mu\text{-}4\text{-}Cl\text{-}pz)_{10}]$ was obtained in a very small crystal yield from a reaction of $FeCl_2{\cdot}4H_2O$, 4-Cl-pzH, $Ce(NO_3)_3{\cdot}6H_2O$, and Et_3N in CH_2Cl_2 and MeCN (Scheme 11). Crystals of a minor reaction product grew from slow evaporation of the reaction filtrate. This product has not been reproducible under the same conditions. Synthesis and optimization are still in progress. The major product of the reaction is a dark red precipitate insoluble in all organic solvents tested and has not been characterized yet.

Complex **22** crystallizes in the orthorhombic *Immm* space group (Figure 68) with the asymmetric unit showing one third of the molecular unit cell. Crystallographic data and refinement parameters are shown in Table 22. All iron centers are in the +3 oxidation state and are coordinated in a distorted octahedral fashion. Two iron centers have the same six-coordinate environment consisting of four bridging pyrazolato ligands, one μ_3-O, and one terminal chloride ligand. The other four iron centers are all in the same coordination environments with three bridging pyrazolato ligands, two μ-OH, and one μ_3-O. There is thermal disorder of the pyrazolato ligands and the Et_3NH^+ counterions – a new set of diffraction data needs to be collected at low temperature. The conformation and topology

of Fe^{III}_6 cores have been categorized in the literature[118] -- complex **22** is categorized as planar (Figure 69).

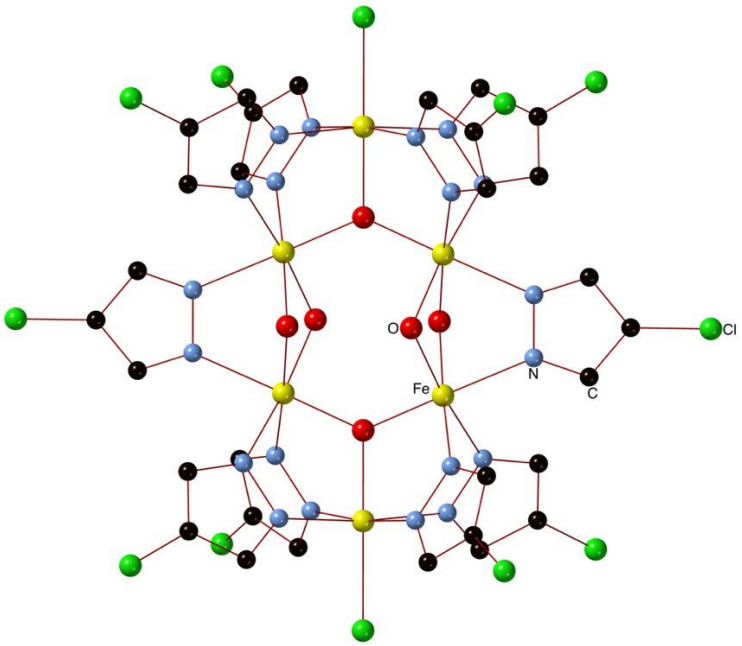

Figure 68. Ball-and-stick representation of $[Fe_6Cl_2(\mu_3\text{-}O)_2(\mu\text{-}OH)_4(\mu\text{-}4\text{-}Cl\text{-}pz)_{10}]^{2-}$ (**22**), counterions and H's atoms have been omitted for simplicity.

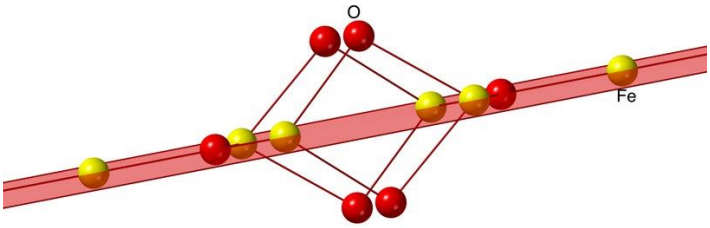

Figure 69. Ball-and-stick representation of $[Fe^{III}_6O_6]^{+10}$ (**22**) with plane passing through all six iron centers.

Complex **22** might be viewed as two asymmetric triangular Fe_3-(μ_3-oxo) subunits bridged together by hydroxo groups. The three iron centers form an isosceles triangle with side lengths of 3.21(2) Å, 3.21(2) Å, and 3.49(4) Å (Table 21). The bond distances for Fe – (μ_3-O) are 1.90(3) Å for the inside iron centers and 1.93(3) Å for the iron centers on the

outsides. The bond distance for Fe – (μ-OH) is 2.02(5) Å. The O ··· O distances from the (μ-OH) pointing inward towards each other is 2.71(2) Å indicating the presence of H-bonds. The Fe – Cl bond distance is 2.34(4) Å and the bond distances for Fe – N for the pyrazolato bridging the (μ_3-O) bridged iron centers are 2.09(2) Å and 2.10(3) Å, while the Fe – N bond distance for the pyrazolato ligand bridging two (μ-OH) bridged iron centers is 2.15(1) Å.

Table 21. Selected bond lengths (Å) for **22**.

Interatomic bond distances	**22**	**Interatomic bond distances**	**22**
(Fe … Fe)[a]	3.21(2), 3.49(4)	Fe – Cl	2.34(4)
(Fe … Fe)[b]	3.01(1)	(Fe – N)[a]	2.09(2), 2.10(3)
Fe – (μ_3-O)	1.90(3), 1.93(3)	(Fe – N)[b]	2.15(1)
Fe – (μ-OH)	2.02(5)	(O ··· O)[c]	2.71(2)

[a](μ_3-O) bridged; [b](μ-OH) bridged; [c](μ-OH) to (μ-OH) pointing inwards.

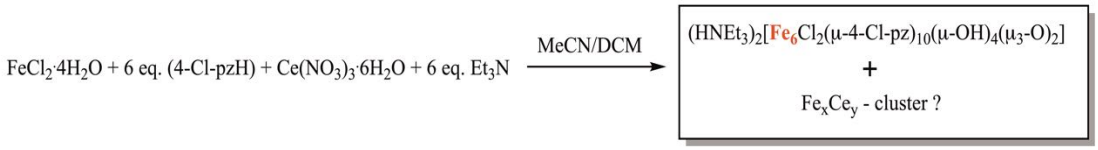

Scheme 11. Synthetic pathway for $(HNEt_3)_2[Fe_6Cl_2(\mu_3\text{-}O)_2(\mu\text{-}OH)_4(\mu\text{-}4\text{-}Cl\text{-}pz)_{10}]$ (**22**).

4.3. Conclusions

Homometallic pyrazolato complexes with different nuclearities were obtained by reacting *mer*-$[InCl_3(4\text{-}I\text{-}pzH)_3]$ and $Fe(ClO_4)_2{\cdot}6H_2O$ in CH_2Cl_2 upon addition of triethylamine (**20**) or by reacting $FeCl_2{\cdot}4H_2O$, 4-Cl-pzH, $Ce(NO_3)_3{\cdot}6H_2O$, and triethylamine in $MeCN/CH_2Cl_2$. The attempt to isolate a heterobimetallic complex was unsuccessful in the above reactions, however, some polynuclear iron complexes were obtained and characterized by SCXRD.

Complex **20** of formula $[Fe_5Cl_3(\mu_4\text{-}O)(\mu_3\text{-}O)(\mu\text{-}OH)_2(\mu\text{-}4\text{-}I\text{-}pz)_6(4\text{-}I\text{-}pzH)_4]\cdot(Et_2O)$ is of particular interest due to its topological similarity to the oxygen evolving complex (OEC) with a Mn_4CaO_5– cluster in the active site of Photosystem II and to the $[Fe_3S_4]$-core of some ferredoxins. Complex **20** was characterized by ^{1}H NMR, UV-visible absorption, and electrochemistry. The cluster is paramagnetic, but the study and analysis of its magnetic properties have not been explored in this project. The electrochemical measurements showed that there were two reversible reduction waves at $E_{1/2}$ = -0.55 V and -0.83 V and one reversible oxidation wave at $E_{1/2}$ = -0.03 V, which is different from previously published $[Fe^{III}_5]$ clusters. The Fe(II)-intermediate (**21**) formed during the synthesis of complex **20** was only partially characterized by SEM-EDS and FTIR. FTIR. Elemental analyses and full spectroscopic studies of both complexes **20** and **21** are still pending. Complex **20** needs to be reproduced and its synthesis optimized. Future studies include ^{57}Fe-Mössbauer spectroscopy measurements, magnetic susceptibility studies and catalytic studies.

Complex **22** of formula $(HNEt_3)_2[Fe_6Cl_2(\mu_3\text{-}O)_2(\mu\text{-}OH)_4(\mu\text{-}4\text{-}Cl\text{-}pz)_{10}]$ needs to be reproduced and additional characterization needs to be performed, including Mössbauer spectroscopy, magnetic susceptibility studies, UV-vis absorption, ^{1}H NMR, and electrochemistry. Polynuclear iron oxo – hydroxo complexes could have large number of unpaired electrons and work as building blocks for magnetic materials. One way to obtain high number of unpaired electrons in polynuclear iron complexes is by incorporating spin frustration due to topology.[118] Previous studies have shown similar $[Fe^{III}_6]$ clusters with S_T = 5 ground state resulting from spin frustration.[118] Complex **22** is an ideal candidate for spin frustration due to topology which can be determined by variable temperature magnetic

susceptibility studies, variable field magnetization studies, and spin-state ordering calculations.

4.4. Experimental section

4.4.1. Materials

Reagent grade chemicals were obtained from commercial sources and used as received. All solvents were stored over 4 Å molecular sieves. Anhydrous $InCl_3$ was stored and weighed in a glove box compartment under argon, while $FeCl_2 \cdot 4H_2O$, $Fe(ClO_4)_2 \cdot 6H_2O$ and $Ce(NO_3)_3 \cdot 6H_2O$ were stored in a desiccator.

4.4.2. Instrumentation and X-ray crystallography

SEM-EDS were measured on JEOL JSM 5900LV with EDS-UTW detector at Florida International University and at Lawrence Livermore National Laboratory. ^1H NMR spectra were recorded on a 400 MHz Bruker Avance NMR spectrometer and were referenced, using the residual solvent proton resonances. Infrared spectra (FTIR) were recorded on an Agilent Avance Cary-660 FT-IR spectrometer at room temperature. CV, DPV, and SWV were measured from 0.1 mM of material in a dry THF (degassed and stored under argon gas) solution containing 0.1 M Et_4NClO_4. The UV-vis spectra were recorded on an Agilent Technologies Cary 6000i Series UV-vis-NIR Spectrophotometer with 1 cm optical path length cuvettes in a dry THF solution.

Refer to section 2.7.4 for single crystal X-ray diffraction details.

4.4.3. Synthesis and characterization

4.4.3.1. Synthesis of $[Fe_5Cl_3(\mu_4\text{-}O)(\mu_3\text{-}O)(\mu\text{-}OH)_2(\mu\text{-}4\text{-}I\text{-}pz)_6(4\text{-}I\text{-}pzH)_4]\cdot(Et_2O)$ (20) and Fe(II)-intermediate (21)

Triethylamine (42 µL, 0.3 mmol) were added to a mixture of *mer*-$[InCl_3(4\text{-}I\text{-}pzH)_3]$ (242.6 mg, 0.3 mmol) and $Fe(ClO_4)_2\cdot 6H_2O$ (25.74 mg, 0.1 mmol) in 3 mL CH_2Cl_2 and the mixture was stirred for 48 h resulting in a precipitate and yellow filtrate. The precipitate was washed thoroughly with CH_2Cl_2 until no color came off in the filtrate and was dried in a desiccator. The precipitate was redissolved in MeCN, filtered, and layered with Et_2O. Dark red X-ray grade crystals, grown after 7 days, were washed with MeOH and Et_2O and air-dried. Yield: 63%.

4.4.3.2. Synthesis of $(HNEt_3)_2[Fe_6Cl_2(\mu_3\text{-}O)_2(\mu\text{-}OH)_4(\mu\text{-}4\text{-}Cl\text{-}pz)_{10}]$ (22)

$FeCl_2\cdot 4H_2O$ (99.4 mg, 0.5 mmol) and 4-Cl-pzH (307.56 mg, 3 mmol) were added to a solution of Et_3N (417 µL, 3 mmol) in 3 mL CH_2Cl_2. A solution of $Ce(NO_3)_3\cdot 6H_2O$ (217.5 mg, 0.5 mmol) in 3 mL acetonitrile was added to the CH_2Cl_2 solution under stirring. The mixture was allowed to react for 4 days. An orange filtrate and a dark red precipitate formed. The filtrate was allowed to slowly evaporate, resulting in X-ray quality crystals after 9 days. (Not reproducible yet). Yield: ~ 1%.

Table 22. Structure refinement parameters for complexes **20** and **22**.

Compound	**20**	**22**
Empirical formula	$C_{34}H_{33}Cl_3Fe_5I_{10}N_{20}O_5$	$C_{38}H_{44}Cl_{12}Fe_6N_{22}O_6$
Formula weight	2438.34	1667.47
Temperature/K	273.15	299
Crystal system	orthorhombic	orthorhombic
Space group	$P2_12_12_1$ (No. 19)	*Immm* (No. 71)
a/Å	17.4853(15)	12.4798(4)
b/Å	19.3327(16)	16.8022(5)
c/Å	26.126(2)	22.1455(7)
α/°	90	90
β/°	90	90
γ/°	90	90
Volume/Å^3	8831.7(13)	4643.6(3)
Z	4	2
ρ_{calc}g/cm^3	1.834	1.193
μ/mm^1	4.427	1.299
Ref. Coll./Indp. Ref.	106221/16174	53419/3205
R_{int}	0.0934	0.1113
Param./[a]Obsv. Ref.	628/7443	120/2778
[b]GooF	1.273	1.195
[c]wR_2	0.4055	0.2972
[d]R_1	0.1240	0.1177
Flack Parameter	0.510(9)	

[a] $I_o > 2\sigma(I_o)$

[b] GooF = $[\Sigma[w(F_o^2-F_c^2)^2]/(N_o-N_v)]^{1/2}$ (N_o=*number of observations*, N_v=*number of variables*)

[c] wR_2 = $\Sigma||F_o|-|F_c||/\Sigma|F_o|$

[d] R_1 = $[(\Sigma w(F_o^2-F_c^2)^2/\Sigma|F_o|^2)]^{1/2}$

5. Conclusions and future work

Indium pyrazole/pyrazolato

To develop new well-defined heterobimetallic pyrazolato complexes as models of mixed-metal oxide minerals, the synthesis and study of indium pyrazole/pyrazolato chemistry was in order since it has not been developed elsewhere. Results are summarized in Scheme 12. Mononuclear complexes of general formula *mer*-$[InCl_3(pz^*H)_3]$ (pz^*H = pzH, 4-Cl-pzH, 4-Br-pzH, 4-I-pzH, 4-Ph-pzH, 4-Me-pzH, 3,5-Me_2-pzH) and [*trans*-$InCl_2(4\text{-Me-pzH})_4]^+$ formed from the use of anhydrous indium chloride salt. Variable temperature ^1H NMR revealed the complex interplay of simultaneous coordinative flexibility, dissociation, and tautomerization processes due to the labile nature of indium, which can make it difficult to control in solution chemistry.

Analogous to iron and chromium pyrazolato chemistry, where the reactions of mononuclear complexes with base yields dinuclear, trinuclear, and octanuclear species, monomers of indium reacted with base resulted in hexanuclear and polymeric clusters. Hexanuclear complexes of form $[In_6Cl_6(\mu_3\text{-}OH_{0.5})(\mu\text{-}OH)_6(\mu\text{-}pz^*)_6]^{3-}$ (pz^* = pz, 4-Cl-pz, 4-Ph-pz) and polymeric species of form $[In(\mu\text{-}pz^*)_3]_n$ (pz^* = pz, 4-Cl-pz, 4-I-pz, 4-Ph-pz) were isolated. The new family of hexanuclear complexes represent a new motif of indium(III)-oxo/hydroxo species. The polymeric $[In(\mu\text{-}pz^*)_3]_n$ complexes showed luminescence properties and promising emission lifetimes. The results show the versatility of indium to form monomers and high nuclearity clusters. However, the results can be somehow unpredictable and can differ greatly based on the reaction conditions.

Polynuclear heterobimetallic and homometallic complexes

Upon deprotonation of mononuclear pyrazole complexes and the reaction with iron (II) perchlorate hexahydrate or anhydrous iron (II) trifluoromethanesulfonate, polynuclear complexes, both heterobimetallic and homometallic, were isolated. Results are summarized in Scheme 12. Complexes of general form $[Fe_{8-x}In_xCl_4(\mu_4\text{-}O)_4(\mu\text{-}pz)_{12}]$ and $[In_{6-x}Fe_xCl_6(\mu_3\text{-}OH_{0.5})(\mu\text{-}OH)_6(\mu\text{-}pz^*)_6]^{3-}$ are formed showing partial occupancy of the metal sites. Complex $[Fe_{6.56}In_{1.44}(\mu_4\text{-}O)_4(\mu\text{-}pz)_{12}Cl_4]$ was isolated from the reaction and showed indium can only occupy the outer metal sites. However, the individual components for both products could not be separated and the uncontrolled hydrolysis of iron in the reactions yields different average bulk composition from batch to batch as well as other polynuclear complexes. Complex of form $[Fe^{III}_7In_2Cl_4(\mu_3\text{-}O)_2(\mu_3\text{-}OH)_2(\mu_3\text{-}OH_{0.5})_2(\mu\text{-}OH)_2(\mu\text{-}4\text{-}Cl\text{-}pz)_{12}(4\text{-}Cl\text{-}pzH)_2](Et_3NH^+Cl^-)$ was the only heterobimetallic complex isolated showing full occupancy of the metal sites but they yield was only a couple of crystals and the reaction was not reproducible.

The polynuclear homometallic complex of form $[Fe_5Cl_3(\mu_4\text{-}O)(\mu_3\text{-}O)(\mu\text{-}OH)_2(\mu\text{-}4\text{-}I\text{-}pz)_6(4\text{-}I\text{-}pz)_4]\cdot(Et_2O)$ was isolated from the reaction of iron(II) perchlorate hexahydrate and *mer*-$[InCl_3(4\text{-}I\text{-}pzH)_3]$ upon deprotonation with base. This pentanuclear iron complex shows a novel motif with bridging (μ-OH) different from what has previously been seen in the literature. This cluster opens new research avenues due to its specific topology and potential for water splitting catalysis. The iron species that forms as an intermediate during the synthesis of $[Fe_5Cl_3(\mu_4\text{-}O)(\mu_3\text{-}O)(\mu\text{-}OH)_2(\mu\text{-}4\text{-}I\text{-}pz)_6(4\text{-}I\text{-}pz)_4]\cdot(Et_2O)$ is a rare example of a colorless Fe(II) low spin species, which could show some interesting properties.

Another polynuclear complexes of form $(HNEt_3)_2[Fe_6Cl_2(\mu_3\text{-}O)_2(\mu\text{-}OH)_4(\mu\text{-}4\text{-}Cl\text{-}pz)_{10}]$ was isolated from the reactions of ferrous chloride tetrahydrate with 4-Cl-pzH and cerium(III) nitrate hexahydrate upon addition of base. This complex has not been reproducible, yet. The topology of $(HNEt_3)_2[Fe_6Cl_2(\mu\text{-}4\text{-}Cl\text{-}pz)_{10}(\mu\text{-}OH)_4(\mu_3\text{-}O)_2]$ makes it a good candidate for spin frustration which is of interest for fuel cells.

Future work

- The structural characterization of the polymeric indium complexes by synchrotron techniques. – XRPD followed by Rietveld refinement, or structure determination by EXAFS -- is to follow. The structural insight of the complexes should help to understand the luminescence properties of the polymeric indium species and narrow the scope of work to synthesize desired materials with long emission lifetimes.
- Future research will investigate whether the hexanuclear complexes described might show efficient photocatalytic activity for the reduction of substrates, such as CO_2.
- Indium(III)-coordination polymers with high proton conductivity properties will be investigated by employing pyrazoles with acidic functional groups, which could provide novel supramolecular indium materials.
- Further studies of indium(III) complexes showing antipseudomonal and antituberculosis potential.
- Synthesis optimization of heterobimetallic species both with partial occupancy and full occupancy of the metal sites and chemical separation studies of the clusters herein reported is to follow. This will allow their magnetic susceptibility analysis and spectroscopic characterization.
- Calcination of Fe/In species to search for new Fe/In-oxides.

- Further characterization of the pentanuclear iron complex and the Fe(II)-intermediate is to follow, including ^{57}Fe-Mössbauer spectroscopy and magnetic susceptibility studies.
- The three redox-modified pentanuclear complexes identified by voltametric studies ($Fe^{III}_4Fe^{IV}$, $Fe^{III}_4Fe^{II}$ and $Fe^{III}_3Fe^{II}_2$) should be isolated and spectroscopically studied in order to determine the redox-active site involved in its process and probe their valence localization/delocalization.
- The introduction of a heterometal at the vacant site of the incomplete cubane will open up a new research direction.
- Following up the full characterization of the pentanuclear iron cluster, water splitting catalytic activity will be investigated.
- The hexanuclear iron complex needs to be reproduced and additional characterization needs to be performed, including variable temperature magnetic susceptibility studies, variable field magnetization studies, and spin-state ordering calculations of the [Fe^{III}_6] species to determine if spin frustration is present.

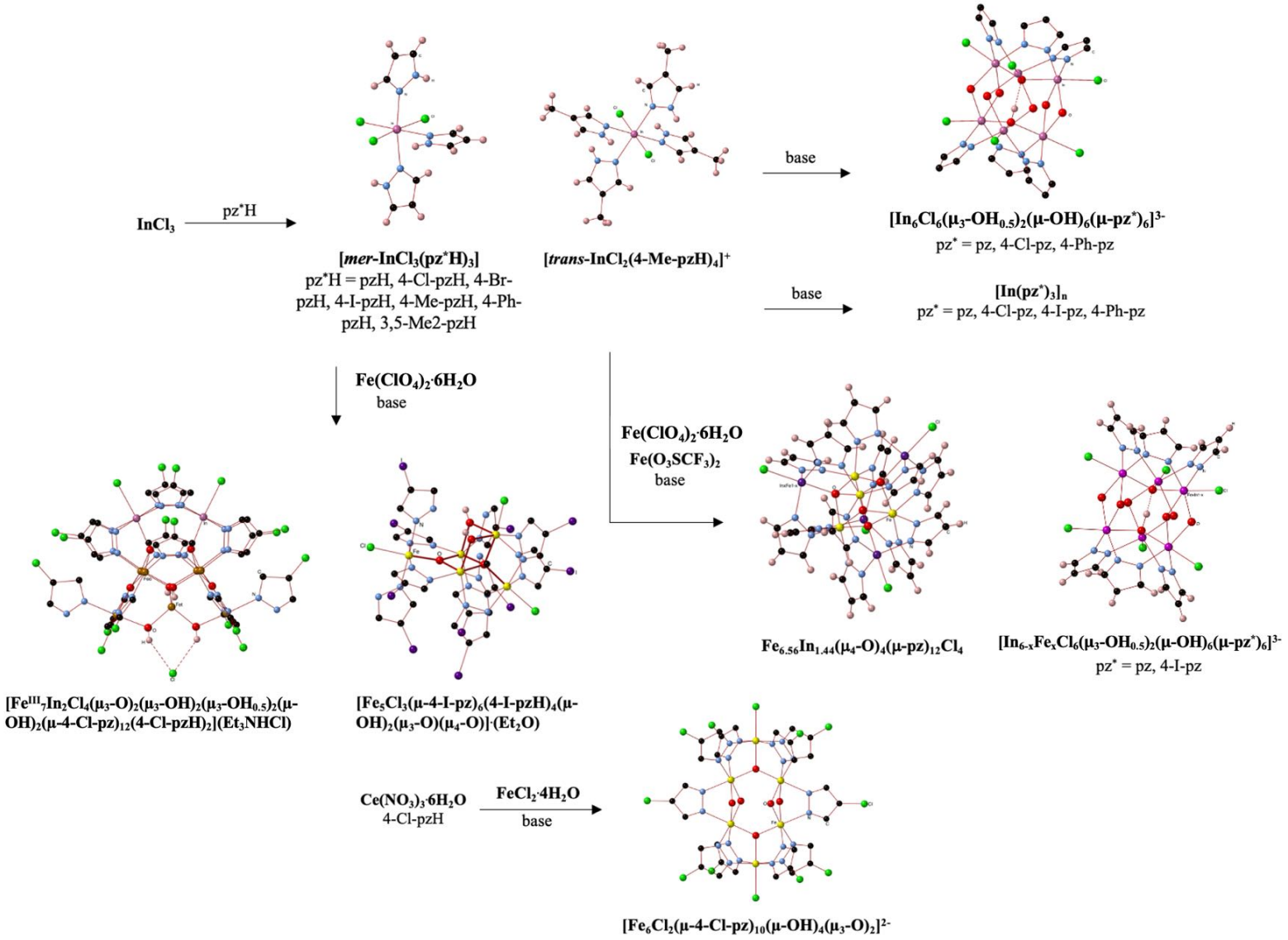

Scheme 12. Summary of In and Fe pyrazole/pyrazolato chemistry.

References

(1) Farooq, U.; Ahmad, T.; Naaz, F.; Islam, S. ul. Review on Metals and Metal Oxides in Sustainable Energy Production: Progress and Perspectives. *Energy Fuels* **2023**, *37* (3), 1577–1632. https://doi.org/10.1021/acs.energyfuels.2c03396.

(2) Zeng, X.; Peng, J.; Zhu, H.; Gong, Y.; Huang, X. Cr-Doped Li2ZnTi3O8 as a High Performance Anode Material for Lithium-Ion Batteries. *Front. Chem.* **2021**, *8*, 600204. https://doi.org/10.3389/fchem.2020.600204.

(3) Dubey, M.; Bhan, U.; Kumar, R. Catalytic Remediation of Chlorinated Organic Compounds (COCs) in Wastewater. In *Emerging Trends to Approaching Zero Waste*; Elsevier, 2022; pp 133–151. https://doi.org/10.1016/B978-0-323-85403-0.00005-0.

(4) Mitra, J.; Mitra, J. Exploring the Potential of Metal Oxides for Biomedical Applications. In *Metal Oxides for Biomedical and Biosensor Applications*; Elsevier, 2022; pp 183–203. https://doi.org/10.1016/B978-0-12-823033-6.00006-5.

(5) Murthy, S.; Effiong, P.; Fei, C. C. Metal Oxide Nanoparticles in Biomedical Applications. In *Metal Oxide Powder Technologies*; Elsevier, 2020; pp 233–251. https://doi.org/10.1016/B978-0-12-817505-7.00011-7.

(6) Danish, M. S. S.; Bhattacharya, A.; Stepanova, D.; Mikhaylov, A.; Grilli, M. L.; Khosravy, M.; Senjyu, T. A Systematic Review of Metal Oxide Applications for Energy and Environmental Sustainability. *Metals* **2020**, *10* (12), 1604. https://doi.org/10.3390/met10121604.

(7) Dey, A.; Jenney, F. E.; Adams, M. W. W.; Babini, E.; Takahashi, Y.; Fukuyama, K.; Hodgson, K. O.; Hedman, B.; Solomon, E. I. Solvent Tuning of Electrochemical Potentials in the Active Sites of HiPIP Versus Ferredoxin. *Science* **2007**, *318* (5855), 1464–1468. https://doi.org/10.1126/science.1147753.

(8) Banci, L.; Bertini, I.; Ciurli, S.; Ferretti, S.; Luchinat, C.; Piccioli, M. The Electronic Structure of Iron-Sulfur [Fe4S4]3+ Clusters in Proteins. An Investigation of the Oxidized High-Potential Iron-Sulfur Protein II from Ectothiorhodospira Vacuolata. *Biochemistry* **1993**, *32* (36), 9387–9397. https://doi.org/10.1021/bi00087a018.

(9) Hoppe, A.; Pandelia, M.-E.; Gärtner, W.; Lubitz, W. [Fe4S4]- and [Fe3S4]-Cluster Formation in Synthetic Peptides. *Biochim. Biophys. Acta BBA - Bioenerg.* **2011**, *1807* (11), 1414–1422. https://doi.org/10.1016/j.bbabio.2011.06.017.

(10) Robertazzi, A.; Galstyan, A.; Knapp, E. W. PSII Manganese Cluster: Protonation of W2, O5, O4 and His337 in the S1 State Explored by Combined Quantum Chemical and Electrostatic Energy Computations. *Biochim. Biophys. Acta BBA - Bioenerg.* **2014**, *1837* (8), 1316–1321. https://doi.org/10.1016/j.bbabio.2014.03.018.

(11) Najafpour, M. M.; Isaloo, M. A.; Eaton-Rye, J. J.; Tomo, T.; Nishihara, H.; Satoh, K.; Carpentier, R.; Shen, J.-R.; Allakhverdiev, S. I. Water Exchange in Manganese-Based Water-Oxidizing Catalysts in Photosynthetic Systems: From the Water-Oxidizing Complex in Photosystem II to Nano-Sized Manganese Oxides. *Biochim. Biophys. Acta* **1837**.

(12) Suga, M.; Akita, F.; Hirata, K.; Ueno, G.; Murakami, H.; Nakajima, Y.; Shimizu, T.; Yamashita, K.; Yamamoto, M.; Ago, H.; Shen, J.-R. Native Structure of Photosystem II at 1.95 Å Resolution Viewed by Femtosecond X-Ray Pulses. *Nature* **2015**, *517* (7532), 99–103. https://doi.org/10.1038/nature13991.

(13) Pilania, G.; Kocevski, V.; Valdez, J. A.; Kreller, C. R.; Uberuaga, B. P. Prediction of Structure and Cation Ordering in an Ordered Normal-Inverse Double Spinel. *Commun. Mater.* **2020**, *1* (1), 84. https://doi.org/10.1038/s43246-020-00082-2.

(14) Lack, J. G.; Chaudhuri, S. K.; Kelly, S. D.; Kemner, K. M.; O'Connor, S. M.; Coates, J. D. Immobilization of Radionuclides and Heavy Metals through Anaerobic Bio-Oxidation of Fe(II). *Appl. Environ. Microbiol.* **2002**, *68* (6), 2704–2710. https://doi.org/10.1128/AEM.68.6.2704-2710.2002.

(15) Dodge, C. J.; Francis, A. J.; Gillow, J. B.; Halada, G. P.; Eng, C.; Clayton, C. R. Association of Uranium with Iron Oxides Typically Formed on Corroding Steel Surfaces. *Environ. Sci. Technol.* **2002**, *36* (16), 3504–3511. https://doi.org/10.1021/es011450+.

(16) Payne, T. E.; Davis, J. A.; Waite, T. D. Uranium Retention by Weathered Schists - The Role of Iron Minerals. *Radiochim. Acta* **1994**, *66–67* (s1), 297–304. https://doi.org/10.1524/ract.1994.6667.s1.297.

(17) Massey, M. S.; Lezama-Pacheco, J. S.; Jones, M. E.; Ilton, E. S.; Cerrato, J. M.; Bargar, J. R.; Fendorf, S. Competing Retention Pathways of Uranium upon Reaction with Fe(II). *Geochim. Cosmochim. Acta* **2014**, *142*, 166–185. https://doi.org/10.1016/j.gca.2014.07.016.

(18) Firsching, F. H.; Brune, S. N. Solubility Products of the Trivalent Rare-Earth Phosphates. *J. Chem. Eng. Data* **1991**, *36* (1), 93–95. https://doi.org/10.1021/je00001a028.

(19) Cotruvo, J. A. The Chemistry of Lanthanides in Biology: Recent Discoveries, Emerging Principles, and Technological Applications. *ACS Cent. Sci.* **2019**, *5* (9), 1496–1506. https://doi.org/10.1021/acscentsci.9b00642.

(20) Dey, A.; Kalita, P.; Chandrasekhar, V. Lanthanide(III)-Based Single-Ion Magnets. *ACS Omega* **2018**, *3* (8), 9462–9475. https://doi.org/10.1021/acsomega.8b01204.

(21) Luzon, J.; Sessoli, R. Lanthanides in Molecular Magnetism: So Fascinating, so Challenging. *Dalton Trans.* **2012**, *41* (44), 13556. https://doi.org/10.1039/c2dt31388j.

(22) Woodruff, D. N.; Winpenny, R. E. P.; Layfield, R. A. Lanthanide Single-Molecule Magnets. *Chem. Rev.* **2013**, *113* (7), 5110–5148. https://doi.org/10.1021/cr400018q.

(23) Bünzli, J.-C. G. Lanthanide Luminescence for Biomedical Analyses and Imaging. *Chem. Rev.* **2010**, *110* (5), 2729–2755. https://doi.org/10.1021/cr900362e.

(24) Lacerda, S.; Tóth, É. Lanthanide Complexes in Molecular Magnetic Resonance Imaging and Theranostics. *ChemMedChem* **2017**, *12* (12), 883–894. https://doi.org/10.1002/cmdc.201700210.

(25) Zhang, Q.; O'Brien, S.; Grimm, J. Biomedical Applications of Lanthanide Nanomaterials, for Imaging, Sensing and Therapy. *Nanotheranostics* **2022**, *6* (2), 184–194. https://doi.org/10.7150/ntno.65530.

(26) Fan, J. H.; Omura, A.; Roca, E. Geopolitics and Rare Earth Metals. *Eur. J. Polit. Econ.* **2022**, 102356. https://doi.org/10.1016/j.ejpoleco.2022.102356.

(27) Terminello, L. J. Challenges in Plutonium and Actinide Materials Science. *MRS Bull.* **2001**, *26* (9), 667–671. https://doi.org/10.1557/mrs2001.175.

(28) Shannon, R. D. Revised Effective Ionic Radii and Systematic Studies of Interatomic Distances in Halides and Chalcogenides. *Acta Crystallogr. Sect. A* **1976**, *32* (5), 751–767. https://doi.org/10.1107/S0567739476001551.

(29) Janczak, J.; Kubiak, R.; Jezierski, A. Synthesis, Crystal Structure and Magnetic Properties of Indium(III) Diphthalocyanine. *Inorg. Chem.* **1995**, *34* (13), 3505–3508. https://doi.org/10.1021/ic00117a020.

(30) Mihaly, J. J.; Zeller, M.; Genna, D. T. Ion-Directed Synthesis of Indium-Derived 2,5-Thiophenedicarboxylate Metal–Organic Frameworks: Tuning Framework Dimensionality. *Cryst. Growth Des.* **2016**, *16* (3), 1550–1558. https://doi.org/10.1021/acs.cgd.5b01680.

(31) Czaja, A. U.; Trukhan, N.; Müller, U. Industrial Applications of Metal–Organic Frameworks. *Chem. Soc. Rev.* **2009**, *38* (5), 1284. https://doi.org/10.1039/b804680h.

(32) Papakyriakou, A.; Katsaros, N. NMR and Molecular Modelling Studies on the Solution Structure of the In^{III} −Bleomycin A2 Complex. *Eur. J. Inorg. Chem.* **2003**, *2003* (16), 3001–3006. https://doi.org/10.1002/ejic.200300072.

(33) Brinkmann, K. O.; Becker, T.; Zimmermann, F.; Kreusel, C.; Gahlmann, T.; Theisen, M.; Haeger, T.; Olthof, S.; Tückmantel, C.; Günster, M.; Maschwitz, T.; Göbelsmann, F.; Koch, C.; Hertel, D.; Caprioglio, P.; Peña-Camargo, F.; Perdigón-

Toro, L.; Al-Ashouri, A.; Merten, L.; Hinderhofer, A.; Gomell, L.; Zhang, S.; Schreiber, F.; Albrecht, S.; Meerholz, K.; Neher, D.; Stolterfoht, M.; Riedl, T. Perovskite–Organic Tandem Solar Cells with Indium Oxide Interconnect. *Nature* **2022**, *604* (7905), 280–286. https://doi.org/10.1038/s41586-022-04455-0.

(34) Martin, O.; Martín, A. J.; Mondelli, C.; Mitchell, S.; Segawa, T. F.; Hauert, R.; Drouilly, C.; Curulla-Ferré, D.; Pérez-Ramírez, J. Indium Oxide as a Superior Catalyst for Methanol Synthesis by CO_2 Hydrogenation. *Angew. Chem. Int. Ed.* **2016**, *55* (21), 6261–6265. https://doi.org/10.1002/anie.201600943.

(35) Friedmann, D.; Caruso, R. A. Indium Oxides and Related Indium-based Photocatalysts for Water Treatment: Materials Studied, Photocatalytic Performance, and Special Highlights. *Sol. RRL* **2021**, *5* (7), 2100086. https://doi.org/10.1002/solr.202100086.

(36) Hussain, I.; Hussain, T.; Lamiel, C.; Zhang, K. Turning Indium Oxide into High-Performing Electrode Materials via Cation Substitution Strategy: Preserving Single Crystalline Cubic Structure of 2D Nanoflakes towards Energy Storage Devices. *J. Power Sources* **2020**, *480*, 228873. https://doi.org/10.1016/j.jpowsour.2020.228873.

(37) Mani, F. Model Systems Containing Pyrazole Chelates and Related Groups: Recent Developments and Perspectives. *Coord. Chem. Rev.* **1992**, *120*, 325–359. https://doi.org/10.1016/0010-8545(92)80058-Y.

(38) Halcrow, M. A. Pyrazoles and Pyrazolides—Flexible Synthons in Self-Assembly. *Dalton Trans.* **2009**, No. 12, 2059. https://doi.org/10.1039/b815577a.

(39) Viciano-Chumillas, M.; Tanase, S.; de Jongh, L. J.; Reedijk, J. Coordination Versatility of Pyrazole-Based Ligands towards High-Nuclearity Transition-Metal and Rare-Earth Clusters. *Eur. J. Inorg. Chem.* **2010**, *2010* (22), 3403–3418. https://doi.org/10.1002/ejic.201000412.

(40) Govor, E. V.; Chakraborty, I.; Piñero, D. M.; Baran, P.; Sanakis, Y.; Raptis, R. G. Structural and 57Fe-Mössbauer Characterization of Mononuclear Ferrous and Ferric Pyrazole Complexes. *Polyhedron* **2012**, *45* (1), 55–60. https://doi.org/10.1016/j.poly.2012.07.052.

(41) Baran, P.; Boča, R.; Chakraborty, I.; Giapintzakis, J.; Herchel, R.; Huang, Q.; McGrady, J. E.; Raptis, R. G.; Sanakis, Y.; Simopoulos, A. Synthesis, Characterization, and Study of Octanuclear Iron-Oxo Clusters Containing a Redox-Active Fe_4O_4-Cubane Core. *Inorg. Chem.* **2008**, *47* (2), 645–655. https://doi.org/10.1021/ic7020337.

(42) Enhessari, M. FeAl2O4 Nanopowders; Structural Analysis and Band Gap Energy. *High Temp. Mater. Process.* **2017**, *36* (8), 789–793. https://doi.org/10.1515/htmp-2015-0229.

(43) Mukhtar, F.; Riaz, S.; Awan, A.; Rubab, F.; Kayani, Z. N.; Naseem, S. Structural and Magnetization Crossover in Electrodeposited $FeAl_2O_4$ – Effect of *in Situ* Oxidation. *RSC Adv.* **2019**, *9* (65), 38183–38194. https://doi.org/10.1039/C9RA04455H.

(44) Kalita, L.; Walawalkar, M. G.; Murugavel, R. Synthesis and Structural Characterization of Dinuclear Complexes of Trivalent Aluminum, Gallium, Indium and Chromium Derived from Pyrazole-2-Ethanol. *Inorganica Chim. Acta* **2011**, *377* (1), 105–110. https://doi.org/10.1016/j.ica.2011.07.047.

(45) López Plá, J. M.; Boudalis, A. K.; Telser, J.; Raptis, R. G. Chromium(III)-Pyrazole Complexes. X-Ray Crystal Structures, 1H NMR Investigation of Ligand Fluxional Behavior and EPR Studies. *Inorganica Chim. Acta* **2020**, *502*, 119299. https://doi.org/10.1016/j.ica.2019.119299.

(46) Cotton, S. A.; Franckevicius, V.; Fawcett, J. Syntheses and Structures of Iron(III) Complexes of Simple N-Donor Ligands. *Polyhedron* **2002**, *21* (20), 2055–2061. https://doi.org/10.1016/S0277-5387(02)01137-3.

(47) Abrahams, M. M.; Cushing, G. W.; Pickett, Z. N.; Howard, W. A.; Wheeler, K. A. Structural and Spectroscopic Characterization of Mer-[RhBr3(Me2pzH)3] (Me2pzH = 3, 5-Dimethylpyrazole); Interpreting the Results with Density Functional Theory Calculations. *J. Chem. Crystallogr.* **2010**, *40* (7), 583–590. https://doi.org/10.1007/s10870-010-9701-2.

(48) Machura, B.; Jaworska, M.; Kruszynski, R. DFT Calculation and X-Ray Structure of the [ReCl3(pzH)3] Complex. *Polyhedron* **2004**, *23* (11), 2005–2011. https://doi.org/10.1016/j.poly.2004.05.003.

(49) Piñero, D.; Baran, P.; Boca, R.; Herchel, R.; Klein, M.; Raptis, R. G.; Renz, F.; Sanakis, Y. A Pyrazolate-Supported Fe_3 (μ_3-O) Core: Structural, Spectroscopic, Electrochemical, and Magnetic Study. *Inorg. Chem.* **2007**, *46* (26), 10981–10989. https://doi.org/10.1021/ic0701460.

(50) Herrera, S.; Rivero, K. I.; Guzmán, A.; Cedeño, J.; Miksovska, J.; Raptis, R. G. Mononuclear, Hexanuclear and Polymeric Indium(III) Pyrazolido Complexes; Structural Characterization, Dynamic Solution Studies and Luminescent Properties. *Dalton Trans.* **2022**, *51* (37), 14277–14286. https://doi.org/10.1039/D2DT01901A.

(51) Vynohradov, O. S.; Davydenko, Y. M.; Pavlenko, V. A.; Naumova, D. D.; Shova, S.; Petlovanyi, D. Crystal Structure and Hirshfeld Surface Analysis of Dichloridotetrakis(4-Methyl-1 *H* -Pyrazole-κ N^2)Nickel(II) Acetonitrile Disolvate.

Acta Crystallogr. Sect. E Crystallogr. Commun. **2022**, *78* (12), 1156–1160. https://doi.org/10.1107/S2056989022010362.

(52) Stepanenko, I. N.; Krokhin, A. A.; John, R. O.; Roller, A.; Arion, V. B.; Jakupec, M. A.; Keppler, B. K. Synthesis, Structure, Spectroscopic Properties, and Antiproliferative Activity In Vitro of Novel Osmium(III) Complexes with Azole Heterocycles. *Inorg. Chem.* **2008**, *47* (16), 7338–7347. https://doi.org/10.1021/ic8006958.

(53) Stepanenko, I.; Mizetskyi, P.; Orlowska, E.; Bučinský, L.; Zalibera, M.; Vénosová, B.; Clémancey, M.; Blondin, G.; Rapta, P.; Novitchi, G.; Schrader, W.; Schaniel, D.; Chen, Y.-S.; Lutz, M.; Kožíšek, J.; Telser, J.; Arion, V. B. The Ruthenium Nitrosyl Moiety in Clusters: Trinuclear Linear μ-Hydroxido Magnesium(II)-Diruthenium(II), μ_3 -Oxido Trinuclear Diiron(III)–Ruthenium(II), and Tetranuclear μ_4 -Oxido Trigallium(III)-Ruthenium(II) Complexes. *Inorg. Chem.* **2022**, *61* (2), 950–967. https://doi.org/10.1021/acs.inorgchem.1c03011.

(54) Peck, M. A.; Hearne, G. R.; Obuah, C.; Darkwa, J. Electron-Density Distributions in Selected Ferrocenyl-Pyrazolyl Late Transition-Metal Complexes. *Phys. Chem. Chem. Phys.* **2018**, *20* (17), 11682–11691. https://doi.org/10.1039/C8CP01135D.

(55) Pruchnik, F. P.; Jakimowicz, P.; Ciunik, Z.; Zakrzewska-Czerwińska, J.; Opolski, A.; Wietrzyk, J.; Wojdat, E. Rhodium(III) Complexes with Polypyridyls and Pyrazole and Their Antitumor Activity. *Inorganica Chim. Acta* **2002**, *334*, 59–66. https://doi.org/10.1016/S0020-1693(02)00776-4.

(56) Sabounchei, S. J.; Shahriary, P.; Salehzadeh, S.; Gholiee, Y.; Khavasi, H. R. Mercury(II) Complexes with 5-Methyl-5-(4-Pyridyl)-2,4-Imidazolidenedione: Synthesis, Structural Characterization, and Theoretical Studies. *J. Mol. Struct.* **2013**, *1051*, 15–22. https://doi.org/10.1016/j.molstruc.2013.07.044.

(57) Kratz, F.; Nuber, B.; Weiß, J.; Keppler, B. K. Synthesis and Characterization of Potential Antitumour and Antiviral Gallium(III) Complexes of N-Heterocycles. *Polyhedron* **1992**, *11* (4), 487–498. https://doi.org/10.1016/S0277-5387(00)83206-4.

(58) Desiraju, G. R.; Parthasarathy, R. The Nature of Halogen.Cntdot..Cntdot..Cntdot.Halogen Interactions: Are Short Halogen Contacts Due to Specific Attractive Forces or Due to Close Packing of Nonspherical Atoms? *J. Am. Chem. Soc.* **1989**, *111* (23), 8725–8726. https://doi.org/10.1021/ja00205a027.

(59) Ibrahim, M. A. A.; Saeed, R. R. A.; Shehata, M. N. I.; Ahmed, M. N.; Shawky, A. M.; Khowdiary, M. M.; Elkaeed, E. B.; Soliman, M. E. S.; Moussa, N. A. M. Type I–IV Halogen···Halogen Interactions: A Comparative Theoretical Study in Halobenzene···Halobenzene Homodimers. *Int. J. Mol. Sci.* **2022**, *23* (6), 3114. https://doi.org/10.3390/ijms23063114.

(60) Deeming, A. J.; Doherty, S.; Marshall, J. E. Rotational Isomerism in Octahedral D6-Iridium(III) Complexes Trans,Mer-[IrCl2(PMe3)3L]+ Where L = PMe3, PMe2Ph or PMePh2; X-Ray Crystal Structure of [IrCl2(PMe3)3(PMe2Ph)]ClO4·CH2Cl2. *Polyhedron* **1991**, *10* (16), 1857–1864. https://doi.org/10.1016/S0277-5387(00)86046-5.

(61) Mastrorilli, P.; Nobile, C. F.; Latronico, M.; Gallo, V.; Englert, U.; Fanizzi, F. P.; Sciacovelli, O. Multinuclear and Dynamic NMR Study of *Trans* -[Pt(Cl)(PHCy $_2$) $_2$ (PCy $_2$)], [Pt(Cl)(PHCy $_2$) $_3$][BF $_4$], [Pt(Cl)(PHCy $_2$) $_3$][Cl], *Trans* -[Pt(Cl)(PHCy $_2$) $_2$ {P(S)Cy $_2$ }], and *Trans* -[Pt(Cl)(PHCy $_2$) $_2$ {P(O)Cy $_2$ }]. Influence of Intramolecular PO···H−P and Cl···H−P Interactions on Restricted Rotation about Pt−P Bond. X-Ray Structure of *Trans* -[Pt(Cl)(PHCy $_2$) $_2$ {P(O)Cy $_2$ }]. *Inorg. Chem.* **2005**, *44* (24), 9097–9104. https://doi.org/10.1021/ic051198x.

(62) Secrieru, A.; O'Neill, P. M.; Cristiano, M. L. S. Revisiting the Structure and Chemistry of 3(5)-Substituted Pyrazoles. *Molecules* **2019**, *25* (1), 42. https://doi.org/10.3390/molecules25010042.

(63) Liu, Y.; Eubank, J. F.; Cairns, A. J.; Eckert, J.; Kravtsov, V. Ch.; Luebke, R.; Eddaoudi, M. Assembly of Metal–Organic Frameworks (MOFs) Based on Indium-Trimer Building Blocks: A Porous MOF with Soc Topology and High Hydrogen Storage. *Angew. Chem. Int. Ed.* **2007**, *46* (18), 3278–3283. https://doi.org/10.1002/anie.200604306.

(64) Hegetschweiler, K.; Ghisletta, M.; Fässler, T. F.; Nesper, R. Hydrolysis to a Complex with a Central, Octahedral (μ $_6$ -O)In $_6$ Unit. *Angew. Chem. Int. Ed. Engl.* **1993**, *32* (10), 1426–1428. https://doi.org/10.1002/anie.199314261.

(65) Yuan, Y.; Li, J.; Sun, X.; Li, G.; Liu, Y.; Verma, G.; Ma, S. Indium–Organic Frameworks Based on Dual Secondary Building Units Featuring Halogen-Decorated Channels for Highly Effective CO $_2$ Fixation. *Chem. Mater.* **2019**, *31* (3), 1084–1091. https://doi.org/10.1021/acs.chemmater.8b04792.

(66) Wieghardt, K.; Kleine-Boymann, M.; Nuber, B.; Weiss, J. Macrocyclic Complexes of Indium(III): Novel .Mu.-Hydroxo- and .Mu.-Oxo-Bridged Complexes. Crystal Structures of [L4In4(.Mu.-OH)6](S2O6)3.4H2O and [L2In2(CH3CO2)4(.Mu.-O)].2NaClO4 (L = 1,4,7-Triazacyclononane). *Inorg. Chem.* **1986**, *25* (10), 1654–1659. https://doi.org/10.1021/ic00230a026.

(67) Okamoto, H. In-O (Indium-Oxygen). *J. Phase Equilibria Diffus.* **2007**, *28* (6), 591–592. https://doi.org/10.1007/s11669-007-9191-x.

(68) Umakoshi, K.; Yamauchi, Y.; Nakamiya, K.; Kojima, T.; Yamasaki, M.; Kawano, H.; Onishi, M. Pyrazolato-Bridged Polynuclear Palladium and Platinum Complexes. Synthesis, Structure, and Reactivity. *Inorg. Chem.* **2003**, *42* (12), 3907–3916. https://doi.org/10.1021/ic026196g.

(69) Deng, X.; Li, C.; Pan, Y.; Deng, D. Indium(III)-Coordination Polymer Based on a C 3 -Symmetric Ligand: Crystal Structure and Anticancer Activity on Neuroblastoma. *Inorg. Nano-Met. Chem.* **2020**, *50* (7), 555–561. https://doi.org/10.1080/24701556.2020.1721022.

(70) Guo, X.; Li, Z.; Chen, X.; Liang, D.; Li, C.; Li, G.; Wang, L.; Shi, Z.; Feng, S. Stable Isomeric Layered Indium Coordination Polymers for High Proton Conduction. *CrystEngComm* **2022**, *24* (2), 294–299. https://doi.org/10.1039/D1CE01107C.

(71) Benson, N.; Suleiman, O.; Odoh, S. O.; Woydziak, Z. R. Pyrazole, Imidazole, and Isoindolone Dipyrrinone Analogues: pH-Dependent Fluorophores That Red-Shift Emission Frequencies in a Basic Solution. *J. Org. Chem.* **2019**, *84* (18), 11856–11862. https://doi.org/10.1021/acs.joc.9b01708.

(72) Schäfer, T. C.; Becker, J.; Sedykh, A. E.; Müller-Buschbaum, K. 2D-Coordination Polymers Constituted from Indium Halides and Dipyridyl N-Donor Ligands. *Z. Für Anorg. Allg. Chem.* **2021**, *647* (11), 1227–1233. https://doi.org/10.1002/zaac.202100047.

(73) Chen, D.; Zhong, Y.; Zhang, C.; Xu, D.; Lin, Z. Dual-Ligand Approach for the Solvent-Free Synthesis of Indium-Based Coordination Polymers. *Inorg. Chem. Commun.* **2018**, *92*, 74–77. https://doi.org/10.1016/j.inoche.2018.04.009.

(74) Omary, M. A.; Rawashdeh-Omary, M. A.; Diyabalanage, H. V. K.; Dias, H. V. R. Blue Phosphors of Dinuclear and Mononuclear Copper(I) and Silver(I) Complexes of 3,5-Bis(Trifluoromethyl)Pyrazolate and the Related Bis(Pyrazolyl)Borate. *Inorg. Chem.* **2003**, *42* (26), 8612–8614. https://doi.org/10.1021/ic0347586.

(75) Yam, V. W.-W.; Lo, K. K.-W. Luminescent Polynuclear D10 Metal Complexes. *Chem. Soc. Rev.* **1999**, *28* (5), 323–334. https://doi.org/10.1039/a804249g.

(76) Swaminathan, M.; Dogra, S. K. A Study on the Phosphorescence Spectra of Pyrazoles at 77 K. *Spectrochim. Acta Part Mol. Spectrosc.* **1983**, *39* (11), 973–977. https://doi.org/10.1016/0584-8539(83)80087-7.

(77) Catalan, J.; Fabero, F.; Claramunt, R. M.; Santa Maria, M. D.; Foces-Foces, M. de la C.; Hernandez Cano, F.; Martinez-Ripoll, M.; Elguero, J.; Sastre, R. New Ultraviolet Stabilizers: 3- and 5-(2'-Hydroxyphenyl)Pyrazoles. *J. Am. Chem. Soc.* **1992**, *114* (13), 5039–5048. https://doi.org/10.1021/ja00039a014.

(78) Lee, S. H.; Shin, N.; Kwak, S. W.; Hyun, K.; Woo, W. H.; Lee, J. H.; Hwang, H.; Kim, M.; Lee, J.; Kim, Y.; Lee, K. M.; Park, M. H. Intriguing Indium-Salen Complexes as Multicolor Luminophores. *Inorg. Chem.* **2017**, *56* (5), 2621–2626. https://doi.org/10.1021/acs.inorgchem.6b02797.

(79) Crystal Structures of Two 4-Bromopyrazole Derivatives. *Z. Für Krist. - Cryst. Mater.* **1999**, *214* (4), 237–241. https://doi.org/10.1524/zkri.1999.214.4.237.

(80) Goddard, R.; Claramunt, R. M.; Escolástico, C.; Elguero, J. Structures of NH-Pyrazoles Bearing Only C-Methyl Substituents: 4-Methylpyrazole Is a Hydrogen-Bonded Trimer in the Solid (100 K). *New J. Chem.* **1999**, *23* (2), 237–240. https://doi.org/10.1039/a808186g.

(81) Raptis, R. G.; Staples, R. J.; King, C.; Fackler Jnr, J. P. Structure of [3,5-(C6H5)2C3H2N2]4. A 3,5-Diphenylpyrazole Tetramer Linked by Hydrogen Bonds. *Acta Crystallogr. C* **1993**, *49* (10), 1716–1719. https://doi.org/10.1107/S0108270193005980.

(82) Rue, K.; Raptis, R. G. Low-Temperature Crystal Structure of 4-Chloro-1 *H* -Pyrazole. *Acta Crystallogr. Sect. E Crystallogr. Commun.* **2021**, *77* (9), 955–957. https://doi.org/10.1107/S2056989021008604.

(83) Reedijk, J.; Windhorst, J. C. A.; van Ham, N. H. M.; Groeneveld, W. L. Pyrazoles and Imidazoles as Ligands. Part IX: Some Adducts Formed between Cu(II) Salts and Substituted Pyrazoles. *Recl. Trav. Chim. Pays-Bas* **2010**, *90* (3), 234–251. https://doi.org/10.1002/recl.19710900302.

(84) Reedijk, J. Pyrazoles and Imidazoles as Ligands: Part I. Some Simple Metal(II) Perchlorates and Tetrafluoroborates Solvated by Neutral Pyrazole and Imidazole. *Recl. Trav. Chim. Pays-Bas* **2010**, *88* (12), 1451–1470. https://doi.org/10.1002/recl.19690881210.

(85) Zecchina, A.; Cerruti, L.; Coluccia, S.; Borello, E. A Vibrational Assignment for Pyrazole. *J. Chem. Soc. B Phys. Org.* **1967**, 1363. https://doi.org/10.1039/j29670001363.

(86) Vos, J. G.; Groeneveld, W. L. Pyrazolato and Related Anions. Part III. Vibrational Assignments of Salts and Neutral Ligands. *Inorganica Chim. Acta* **1978**, *27*, 173–180. https://doi.org/10.1016/S0020-1693(00)87280-1.

(87) Rosenkranz, A. A.; Slastnikova, T. A.; Karmakova, T. A.; Vorontsova, M. S.; Morozova, N. B.; Petriev, V. M.; Abrosimov, A. S.; Khramtsov, Y. V.; Lupanova, T. N.; Ulasov, A. V.; Yakubovskaya, R. I.; Georgiev, G. P.; Sobolev, A. S. Antitumor Activity of Auger Electron Emitter 111In Delivered by Modular Nanotransporter for Treatment of Bladder Cancer With EGFR Overexpression. *Front. Pharmacol.* **2018**, *9*, 1331. https://doi.org/10.3389/fphar.2018.01331.

(88) Blower, P. J. A Nuclear Chocolate Box: The Periodic Table of Nuclear Medicine. *Dalton Trans.* **2015**, *44* (11), 4819–4844. https://doi.org/10.1039/C4DT02846E.

(89) *The Chemistry of Molecular Imaging*; Long, N. J., Wong, W.-T., Eds.; Wiley: Hoboken, New Jersey, 2015.

(90) Husain, Z. A.; Majeed, A. A.; Rasheed, R. T.; Mansoor, H. S.; Hussein, N. N. Antibacterial Activity of In2O3 Nanopowders Prepared by Hydrothermal Method. *Mater. Today Proc.* **2021**, *42*, 1816–1821. https://doi.org/10.1016/j.matpr.2020.12.189.

(91) Tajbakhsh, S.; Mohammadi, K.; Deilami, I.; Zandi, K.; Ramedani, E.; Asayesh, G. Antibacterial Activity of Indium Curcumin and Indium Diacetylcurcumin.

(92) David, S.; Barros, V.; Cruz, C.; Delgado, R. In Vitro Effect of Free and Complexed Indium(III) against *Mycobacterium Tuberculosis*. *FEMS Microbiol. Lett.* **2005**, *251* (1), 119–124. https://doi.org/10.1016/j.femsle.2005.07.044.

(93) Asadi, M.; Savaripoor, N.; Asadi, Z.; Ghatee, M. H.; Moosavi, F.; Yousefi, R.; Jamshidi, M. Synthesis and Characterization of Some New Schiff Base Complexes of Group 13 Elements, Ab Initio Studies, Cytotoxicity and Reaction with Hydrogen Peroxide. *Spectrochim. Acta. A. Mol. Biomol. Spectrosc.* **2013**, *101*, 394–399. https://doi.org/10.1016/j.saa.2012.09.007.

(94) Oliveira, A. A.; Perdigão, G. M. C.; Rodrigues, L. E.; da Silva, J. G.; Souza-Fagundes, E. M.; Takahashi, J. A.; Rocha, W. R.; Beraldo, H. Cytotoxic and Antimicrobial Effects of Indium(III) Complexes with 2-Acetylpyridine-Derived Thiosemicarbazones. *Dalton Trans.* **2017**, *46* (3), 918–932. https://doi.org/10.1039/C6DT03657K.

(95) Talbot, G. H.; Jezek, A.; Murray, B. E.; Jones, R. N.; Ebright, R. H.; Nau, G. J.; Rodvold, K. A.; Newland, J. G.; Boucher, H. W.; The Infectious Diseases Society of America. The Infectious Diseases Society of America's 10 × '20 Initiative (10 New Systemic Antibacterial Agents US Food and Drug Administration Approved by 2020): Is 20 × '20 a Possibility? *Clin. Infect. Dis.* **2019**, *69* (1), 1–11. https://doi.org/10.1093/cid/ciz089.

(96) Tacconelli, E.; Carrara, E.; Savoldi, A.; Harbarth, S.; Mendelson, M.; Monnet, D. L.; Pulcini, C.; Kahlmeter, G.; Kluytmans, J.; Carmeli, Y.; Ouellette, M.; Outterson, K.; Patel, J.; Cavaleri, M.; Cox, E. M.; Houchens, C. R.; Grayson, M. L.; Hansen, P.; Singh, N.; Theuretzbacher, U.; Magrini, N.; Aboderin, A. O.; Al-Abri, S. S.; Awang Jalil, N.; Benzonana, N.; Bhattacharya, S.; Brink, A. J.; Burkert, F. R.; Cars, O.; Cornaglia, G.; Dyar, O. J.; Friedrich, A. W.; Gales, A. C.; Gandra, S.; Giske, C. G.; Goff, D. A.; Goossens, H.; Gottlieb, T.; Guzman Blanco, M.; Hryniewicz, W.; Kattula, D.; Jinks, T.; Kanj, S. S.; Kerr, L.; Kieny, M.-P.; Kim, Y. S.; Kozlov, R. S.; Labarca, J.; Laxminarayan, R.; Leder, K.; Leibovici, L.; Levy-Hara, G.; Littman, J.; Malhotra-Kumar, S.; Manchanda, V.; Moja, L.; Ndoye, B.; Pan, A.; Paterson, D. L.; Paul, M.; Qiu, H.; Ramon-Pardo, P.; Rodríguez-Baño, J.; Sanguinetti, M.; Sengupta, S.; Sharland, M.; Si-Mehand, M.; Silver, L. L.; Song, W.; Steinbakk, M.; Thomsen,

J.; Thwaites, G. E.; van der Meer, J. W.; Van Kinh, N.; Vega, S.; Villegas, M. V.; Wechsler-Fördös, A.; Wertheim, H. F. L.; Wesangula, E.; Woodford, N.; Yilmaz, F. O.; Zorzet, A. Discovery, Research, and Development of New Antibiotics: The WHO Priority List of Antibiotic-Resistant Bacteria and Tuberculosis. *Lancet Infect. Dis.* **2018**, *18* (3), 318–327. https://doi.org/10.1016/S1473-3099(17)30753-3.

(97) Ghuman, K. K.; Hoch, L. B.; Szymanski, P.; Loh, J. Y. Y.; Kherani, N. P.; El-Sayed, M. A.; Ozin, G. A.; Singh, C. V. Photoexcited Surface Frustrated Lewis Pairs for Heterogeneous Photocatalytic CO $_2$ Reduction. *J. Am. Chem. Soc.* **2016**, *138* (4), 1206–1214. https://doi.org/10.1021/jacs.5b10179.

(98) Andreu, N.; Zelmer, A.; Fletcher, T.; Elkington, P. T.; Ward, T. H.; Ripoll, J.; Parish, T.; Bancroft, G. J.; Schaible, U.; Robertson, B. D.; Wiles, S. Optimisation of Bioluminescent Reporters for Use with Mycobacteria. *PLoS ONE* **2010**, *5* (5), e10777. https://doi.org/10.1371/journal.pone.0010777.

(99) Andreu, N.; Fletcher, T.; Krishnan, N.; Wiles, S.; Robertson, B. D. Rapid Measurement of Antituberculosis Drug Activity in Vitro and in Macrophages Using Bioluminescence. *J. Antimicrob. Chemother.* **2012**, *67* (2), 404–414. https://doi.org/10.1093/jac/dkr472.

(100) Sheldrick, G. M. *SHELXT* – Integrated Space-Group and Crystal-Structure Determination. *Acta Crystallogr. Sect. Found. Adv.* **2015**, *71* (1), 3–8. https://doi.org/10.1107/S2053273314026370.

(101) Dolomanov, O. V.; Bourhis, L. J.; Gildea, R. J.; Howard, J. A. K.; Puschmann, H. *OLEX2* : A Complete Structure Solution, Refinement and Analysis Program. *J. Appl. Crystallogr.* **2009**, *42* (2), 339–341. https://doi.org/10.1107/S0021889808042726.

(102) Sheldrick, G. M. Crystal Structure Refinement with *SHELXL*. *Acta Crystallogr. Sect. C Struct. Chem.* **2015**, *71* (1), 3–8. https://doi.org/10.1107/S2053229614024218.

(103) Spek, A. L. Structure Validation in Chemical Crystallography. *Acta Crystallogr. D Biol. Crystallogr.* **2009**, *65* (2), 148–155. https://doi.org/10.1107/S090744490804362X.

(104) Ube, H.; Endo, K.; Sato, H.; Shionoya, M. Synthesis of Hetero-Multinuclear Metal Complexes by Site-Selective Redox Switching and Transmetalation on a Homo-Multinuclear Complex. *J. Am. Chem. Soc.* **2019**, *141* (26), 10384–10389. https://doi.org/10.1021/jacs.9b04123.

(105) Zueva, E. M.; Sameera, W. M. C.; Piñero, D. M.; Chakraborty, I.; Devlin, E.; Baran, P.; Lebruskova, K.; Sanakis, Y.; McGrady, J. E.; Raptis, R. G. Experimental and Theoretical Mössbauer Study of an Extended Family of [Fe $_8$ (μ $_4$ -O) $_4$ (μ-4-R-Px)

$_{12}$ X $_{4}$] Clusters. *Inorg. Chem.* **2011**, *50* (3), 1021–1029. https://doi.org/10.1021/ic101691q.

(106) Siskos, M.; Choudhary, M.; Gerothanassis, I. Hydrogen Atomic Positions of O–H···O Hydrogen Bonds in Solution and in the Solid State: The Synergy of Quantum Chemical Calculations with 1H-NMR Chemical Shifts and X-Ray Diffraction Methods. *Molecules* **2017**, *22* (3), 415. https://doi.org/10.3390/molecules22030415.

(107) Mikuriya, M.; Hashimoto, Y.; Nakashima, S. A Novel Pentanuclear Iron(III) Complex with a Defective Double-Cubane Core. *Chem. Commun.* **1996**, No. 3, 295. https://doi.org/10.1039/cc9960000295.

(108) Groves, J. T. Synthetic Models of Metalloenzymes. *Inorganica Chim. Acta* **1983**, *79*, 64. https://doi.org/10.1016/S0020-1693(00)95090-4.

(109) Mehrabani, S.; Bikas, R.; Zand, Z.; Mousazade, Y.; Allakhverdiev, S. I.; Najafpour, M. M. Water Splitting by a Pentanuclear Iron Complex. *Int. J. Hydrog. Energy* **2020**, *45* (35), 17434–17443. https://doi.org/10.1016/j.ijhydene.2020.04.249.

(110) Okamura, M.; Kondo, M.; Kuga, R.; Kurashige, Y.; Yanai, T.; Hayami, S.; Praneeth, V. K. K.; Yoshida, M.; Yoneda, K.; Kawata, S.; Masaoka, S. A Pentanuclear Iron Catalyst Designed for Water Oxidation. *Nature* **2016**, *530* (7591), 465–468. https://doi.org/10.1038/nature16529.

(111) Praneeth, V. K. K.; Kondo, M.; Okamura, M.; Akai, T.; Izu, H.; Masaoka, S. Pentanuclear Iron Catalysts for Water Oxidation: Substituents Provide Two Routes to Control Onset Potentials. *Chem. Sci.* **2019**, *10* (17), 4628–4639. https://doi.org/10.1039/C9SC00678H.

(112) Chen, S.-S.; Zheng, X.-Y.; Tian, H.; Long, L.-S.; Zheng, L.-S.; Kong, X.-J. Aminopolyol-Dependent Assembly of Heterometallic Lanthanide–Iron–Oxo Clusters. *Inorg. Chem.* **2022**, *61* (50), 20365–20372. https://doi.org/10.1021/acs.inorgchem.2c03007.

(113) Peng, Y.; Powell, A. K. What Do 3d-4f Butterflies Tell Us? *Coord. Chem. Rev.* **2021**, *426*, 213490. https://doi.org/10.1016/j.ccr.2020.213490.

(114) Feng, M.; Ruan, Z.-Y.; Chen, Y.-C.; Tong, M.-L. Physical Stimulus and Chemical Modulations of Bistable Molecular Magnetic Materials. *Chem. Commun.* **2020**, *56* (89), 13702–13718. https://doi.org/10.1039/D0CC04202A.

(115) Deng, Q.; Wang, J.; Li, G.; Zhang, S. Synthesis, Structure and Magnetism of a New Ionic Pentanuclear Iron Cluster. *Acta Crystallogr. Sect. C Struct. Chem.* **2020**, *76* (7), 690–694. https://doi.org/10.1107/S205322962000861X.

(116) Martic, M.; Jakab-Simon, I. N.; Haahr, L. T.; Hagen, W. R.; Christensen, H. E. M. Heterometallic [AgFe3S4] Ferredoxin Variants: Synthesis, Characterization, and the

First Crystal Structure of an Engineered Heterometallic Iron–Sulfur Protein. *JBIC J. Biol. Inorg. Chem.* **2013**, *18* (2), 261–276. https://doi.org/10.1007/s00775-012-0971-3.

(117) Lewis, D. L.; Estes, E. D.; Hodgson, D. J. The Infrared Spectra of Coordinated Perchlorates. *J. Cryst. Mol. Struct.* **1975**, *5* (1), 67–74. https://doi.org/10.1007/BF01202553.

(118) Christmas, C. A.; Tsai, H. L.; Pardi, L.; Kesselman, J. M.; Gantzel, P. K.; Chadha, R. K.; Gatteschi, D.; Harvey, D. F.; Hendrickson, D. N. Hexanuclear Ferric Complexes Possessing Different Degrees of Spin Frustration. *J. Am. Chem. Soc.* **1993**, *115* (26), 12483–12490. https://doi.org/10.1021/ja00079a032.

Appendix

- $[Cu^{I}(\mu\text{-}L)]_3$ (L = Anle138b) Project
- Synthesis and characterization of $[Cu^{I}(\mu\text{-}L)]_3$

(Anle138b) (50 mg, 0.146 mmol) was dissolved in a 1:1 mixture of tetrahydrofuran and methanol. $Cu(CH_3CN)_4 \cdot PF_6$ (54.41mg, 0.146 mmol) were added to the solution under stirring. Lastly, triethylamine (20 µL, 0.1 mmol) was added. The reaction was left to stir for 24 h and a white precipitate was obtained by vacuum filtration and washed thoroughly with diethyl ether. The precipitate was allowed to dry in a desiccator. Crystallization was done by redissolving the precipitate in methylene chloride and doing vapor diffusion with methanol. Analysis for $Cu_3N_6Br_3O_6C_{48}H_{30}$ (1217.14 g mol^{-1}), Calcd: C, 47.37; H, 2.48; N, 6.90; Found: C, 47.60; H, 2.41; N, 6.21. FT-IR ($\tilde{\nu}_{max}$, cm^{-1}): 2877(w), 2102(w), 1840(w), 1597(m), 1562(w), 1506(m), 1466(vs), 1311(m), 1242(vs), 1211(s), 1116(m), 1036(vs), 930(m), 852(s), 808(m), 769(vs), 746(s), 677(s), 467(m), 409(s). ^{1}H NMR (400 MHz, CD2Cl2, 296K) δ(ppm) 7.79 (s, 1H), 7.60 (d, ^{2}J = 7.60 Hz, 1H), 7.36 (d, ^{2}J = 7.76 Hz, 1H), 7.13 (d, ^{2}J = 7.96 Hz, 1H), 7.09 (s, 1H), 6.88 (t, ^{3}J = 7.74 Hz, 1H), 6.66 (s, 1H), 6.47 (d, ^{2}J = 7.88 Hz, 1H), 5.96 (s, 2H).

- Crystallographic description of $[Cu^{I}(\mu\text{-}L)]_3$

Crystal structure with general formula $[Cu_3(C_{16}BrO_2N_2H_{10})_3]$ crystallizes in the triclinic *P-1* space group with a whole molecule in the asymmetric unit, featuring an asymmetrically oriented pyrazolyl group; the substituents at the pyrazolyl group's 3- and 5-positions do not show a regular alternating pattern (Figure A1). The structure refinement parameters and selected structural parameters are shown in Table A1 and Table A2,

respectively. The structure shows crystallographic disorder of the 3,5-substituted groups of the pyrazolato and was modeled with one pyrazolato in two positions. The copper centers are all equivalent in a 2-coordinate linear environment formed by two bridging pyrazolyl ligands. The nine membered $[Cu_3N_6]$ metallacycle shows significant deviation from planarity, the torsion angle of the metallacycle plane is 0.258°. $[Cu^I(\mu\text{-}L)]_3$ features well separated $[Cu_3]$ units that adopt a flattened chair arrangement. The inter-triangle Cu ··· Cu distances within the $[Cu_3]$ unit are 3.245 Å, 3.161 Å, and 3.071 Å. The Cu – N bond distances are between 1.77(3) Å and 1.92(2) Å. The intratrimer contacts between copper atoms only occur between Cu_3 ··· Cu_3 and Cu_1 ··· Cu_1, alternating with one another in an infinite staircase like chain of trimers with rather long distances of 4.415 Å and 4.545 Å, respectively (Figure A3).

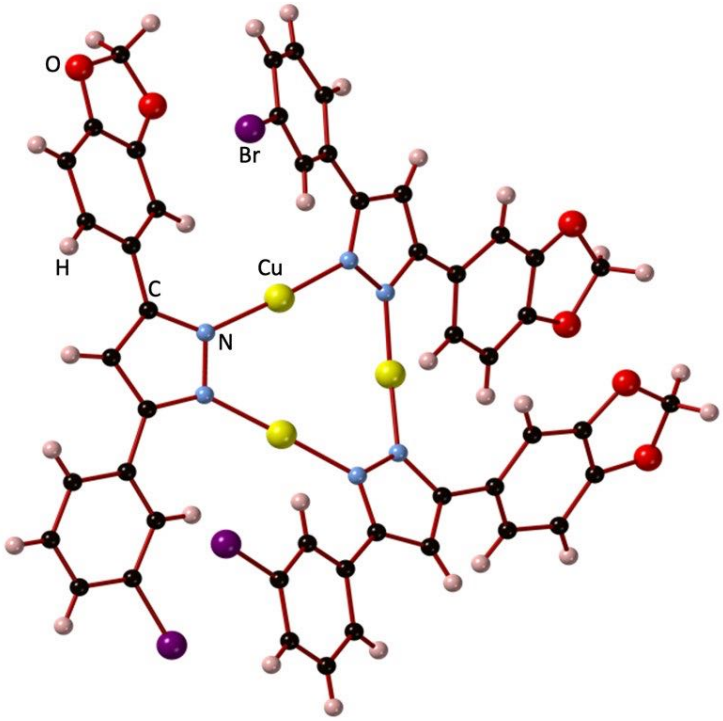

Figure A1. Ball-and-stick representation of $[Cu^I(\mu\text{-}L)]_3$.

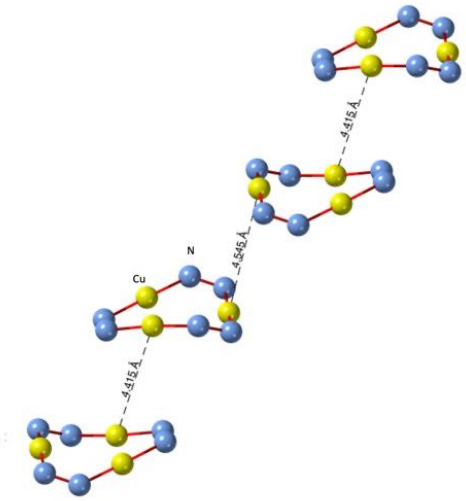

Figure A2. Packing of the Cu_3N_6 metallacycle in $[Cu^I(\mu\text{-L})]_3$ showing intra Cu … Cu distances.

Table A1. Structure refinement parameters for $[Cu^I(\mu\text{-L})]_3$.

Compound	**$[Cu^I(\mu\text{-L})]_3$**
Empirical formula	$C_{48}H_{27}Br_3Cu_3N_6O_6$
Formula weight	1214.10
Temperature/K	273
Crystal system	Triclinic
Space group	*P-1*
a/Å	12.1348(4)
b/Å	14.4421(5)
c/Å	14.8078(5)
α/°	92.375(1)
β/°	112.941(1)
γ/°	108.701(1)
Volume/Å3	2222.1(1)
Z	2
ρ_{calc}g/cm3	1.815
μ/mm^{-1}	4.178
Ref Coll./Indept. Ref	48868/4360
R_{int}	0.0801
Param/[a]Obsv. Ref	738/8121
[b]GooF	1.045
[c]wR_2	0.2064
[d]R_1	0.0609

[a] $I_o > 2\sigma(I_o)$

[b] GooF = $[\Sigma[w(F_o^2-F_c^2)^2]/(N_o-N_v)]^{1/2}$ (N_o=*number of observations*, N_v=*number of variables*)

[c] $wR_2 = \Sigma||F_o|-|F_c||/\Sigma|F_o|$

[d] $R_1 = [(\Sigma w(F_o^2-F_c^2)^2/\Sigma|F_o|^2)]^{1/2}$

Table A2. Selected structural parameters for $[Cu^{I}(\mu\text{-L})]_3$.

***d* Intra (Cu···Cu)/Å**	**∠Cu···Cu···Cu/°**	***d* Inter (Cu···Cu)/Å**	**∠N···Cu···N/°**	**Torsion Angle ∠Cu-N - N -Cu/°**	***d* Cu-N/Å**
3.16(1), 3.24(5), 3.07(1)	59.99(1), 57.25(4), 62.75(5)	4.41(5), 4.54(5)	172.5(3), 178.2(6), 175.0(3)	0.03(3), 0.13(4), 0.07(4)	1.85(1), 1.85(1), 1.85(1), 1.86(1), 1.84(9), 1.85(1)

- ^{1}H NMR and COSY NMR of $[Cu^{I}(\mu\text{-L})]_3$

The ^{1}H-NMR spectra of $[Cu^{I}(\mu\text{-L})]_3$ was measured in CD_2Cl_2 400 MHz at ambient temperature (Figure A4). The ^{1}H-NMR shows one set of signals corresponding to the deprotonated Anle138b ligand, meaning all pyrazolato ligands are equivalent. All coupling constants are around 7.5 Hz, corresponding to vicinal proton-proton coupling. Protons were assigned by COSY ^{1}H-NMR (Figure A5).

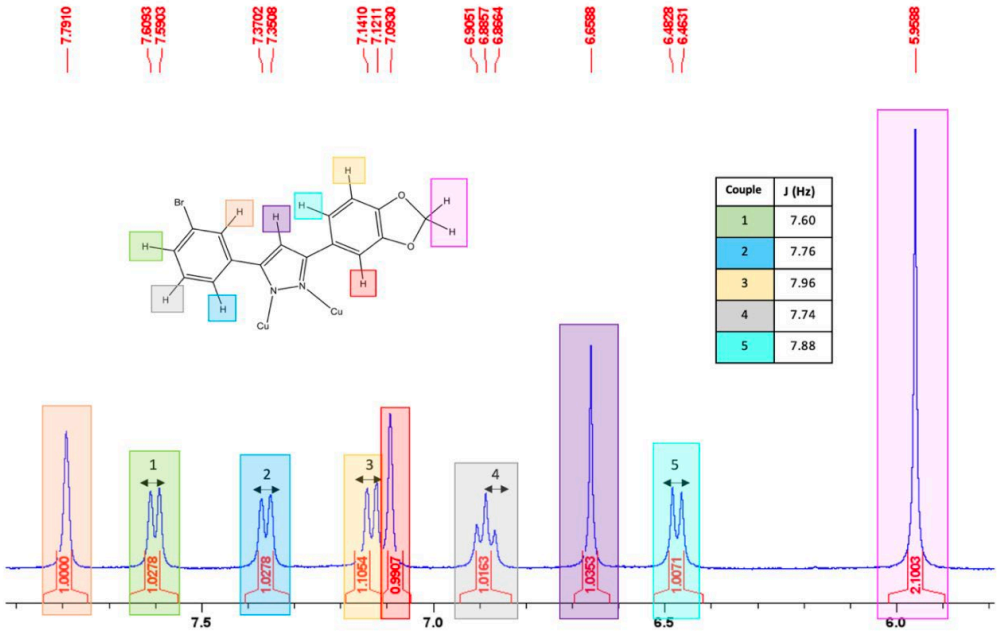

Figure A3. ^{1}H NMR of $[Cu^{I}(\mu\text{-L})]_3$ in CD_2Cl_2 at 400 MHz at ambient temperature. Protons were assigned based on COSY NMR. Coupling constants are shown in the spectrum.

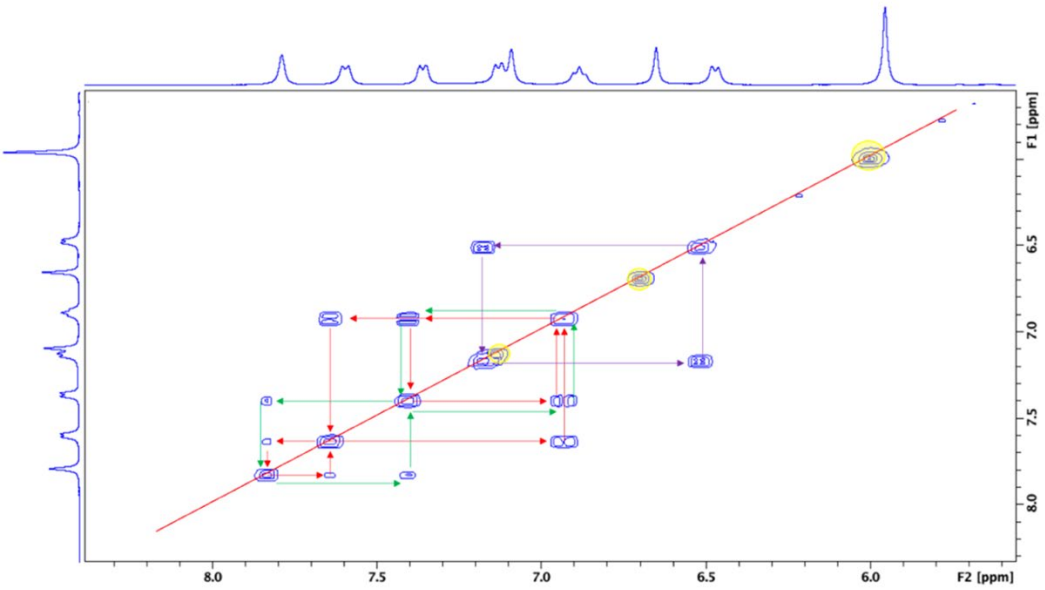

Figure A4. COSY ^{1}H NMR of $[Cu^{I}(\mu\text{-L})]_3$ in CD_2Cl_2 at 400 MHz at ambient temperature.

- FTIR and UV-vis-NIR of $[Cu^{I}(\mu\text{-L})]_3$

FTIR spectra of $[Cu^{I}(\mu\text{-L})]_3$ (Figure A6) shows no stretching bands above 3000 cm^{-1}, which confirms deprotonation of the pyrazole. Bands corresponding to the benzene aromatic ring are observed at 2102 cm^{-1} and 1840 cm^{-1}, and a sharp peak is observed at 1466 cm^{-1} that can be assigned to the C = N stretch. The sharp peak at 1036 cm^{-1} can be assigned to the C – O stretches and the one at 769 cm^{-1} to the C – Br stretch.

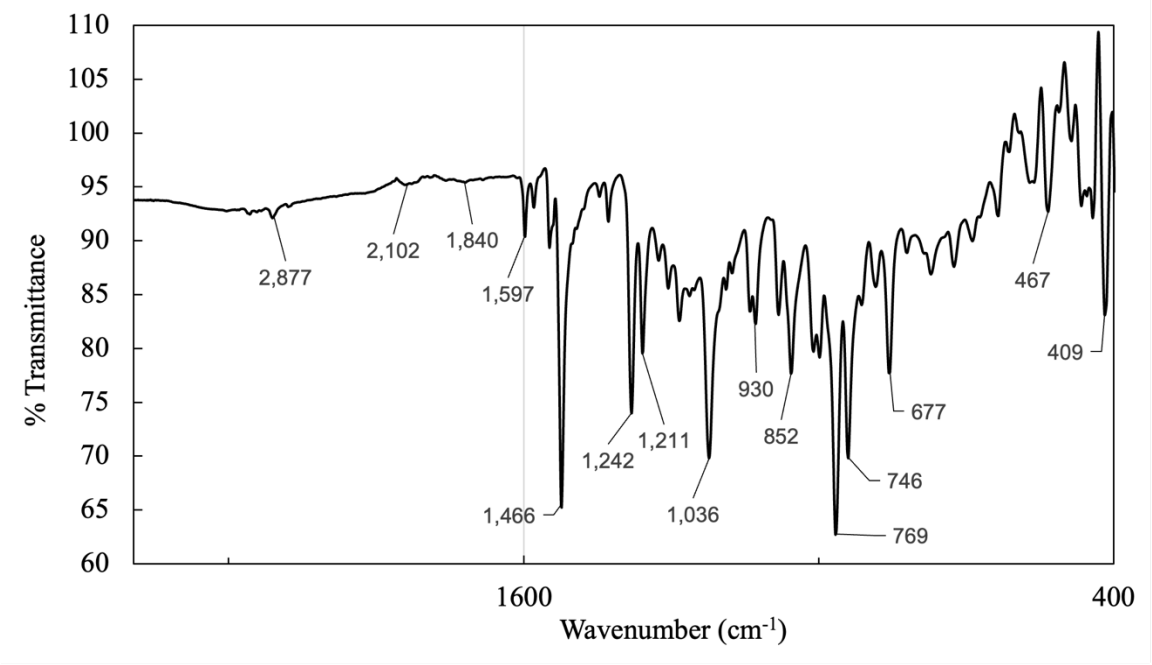

Figure A5. FTIR spectrum of $[Cu^{I}(\mu\text{-L})]_3$.

- Materials, Instrumentation and X-ray crystallography

Chemical reagents and solvents were purchased from Aldrich Chemical Co., Alfa Aesar, Fisher Scientific, and Acros Organics and used as received. 1H-NMR spectra were recorded on a 400 MHz Bruker Avance spectrometers. FTIR spectra was recorded with a Perkin Elmer Spectrum 100 FT-IR spectrometer. Elemental analyses (CHN) were performed by Galbraith Laboratories Inc. at Knoxville, Tennessee.

Refer to section 2.7.4 for crystallographic details.

- Appendix Figures: Chapter 2

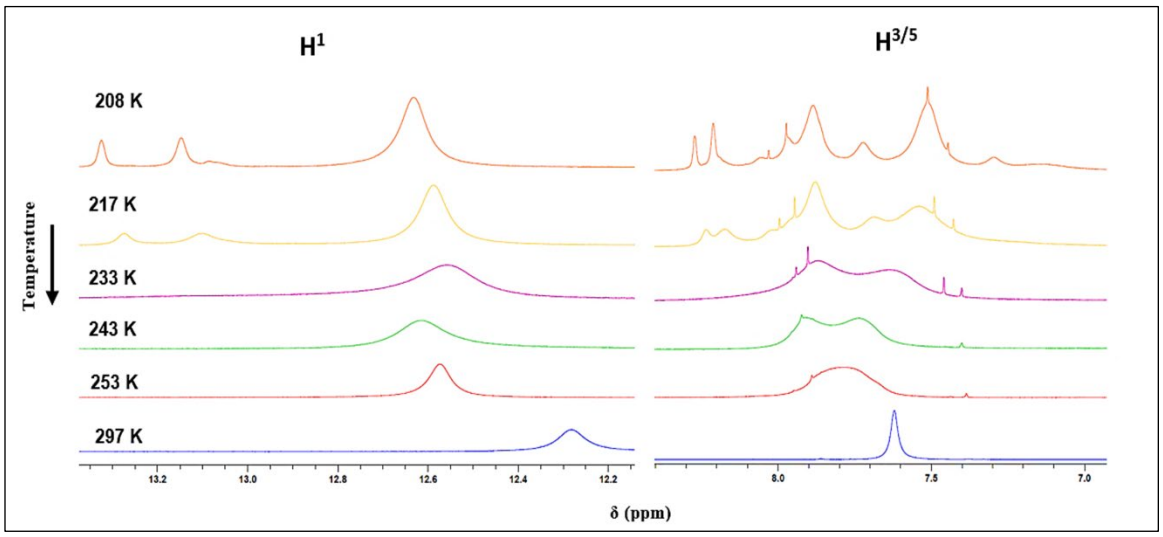

Figure A6. VT ^{1}H NMR spectra of complex **10** in THF-d_8 at 400 MHz.

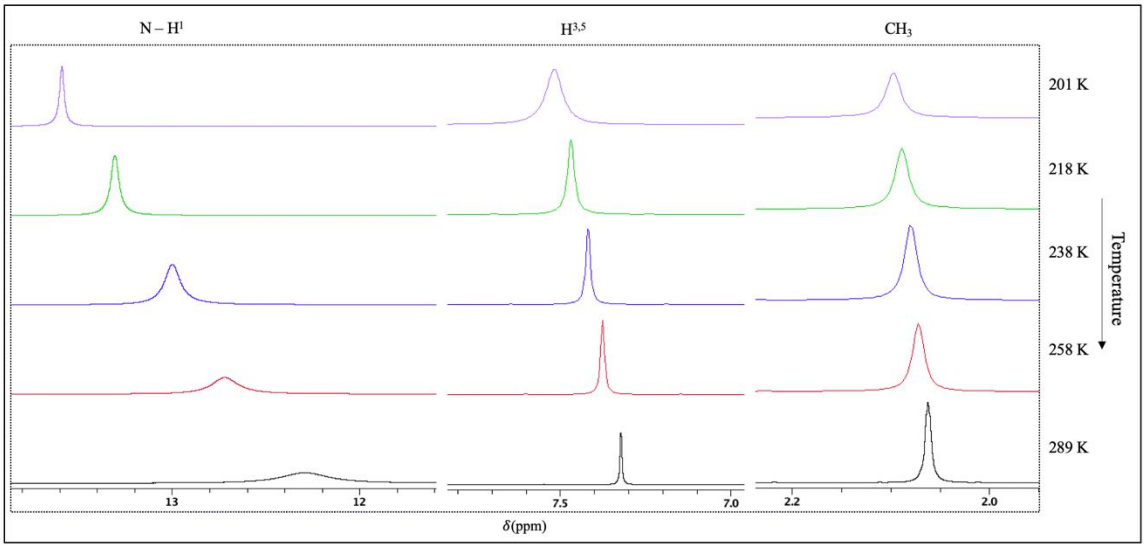

Figure A7. VT ^{1}H NMR of 4-Me-pzH in THF-d_8 at 400MHz.

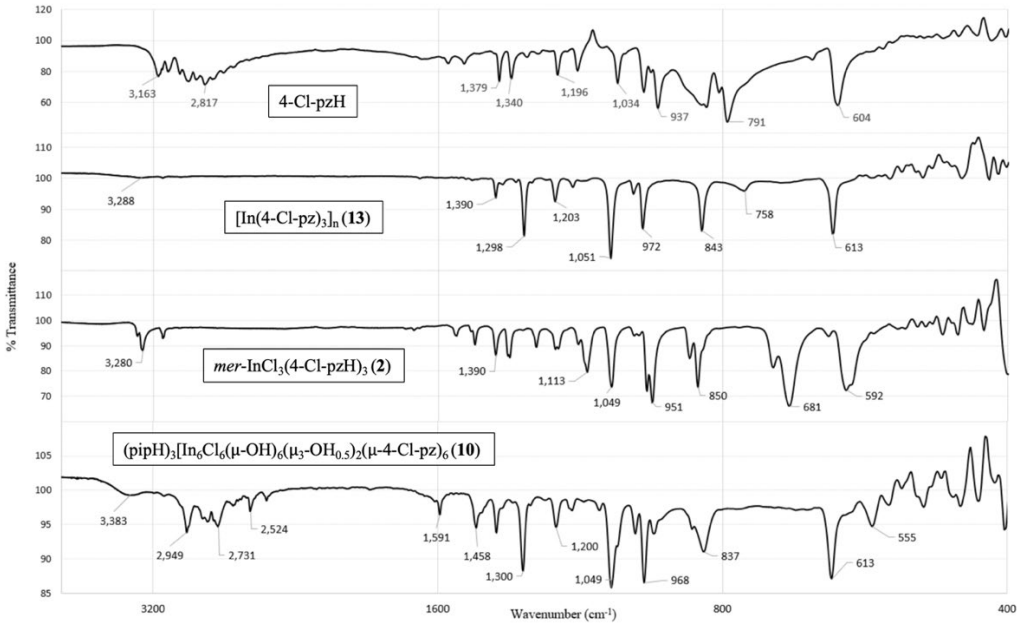

Figure A8. FTIR spectra of free 4-Cl-pzH, and complexes **2**, **10**, and **13**.

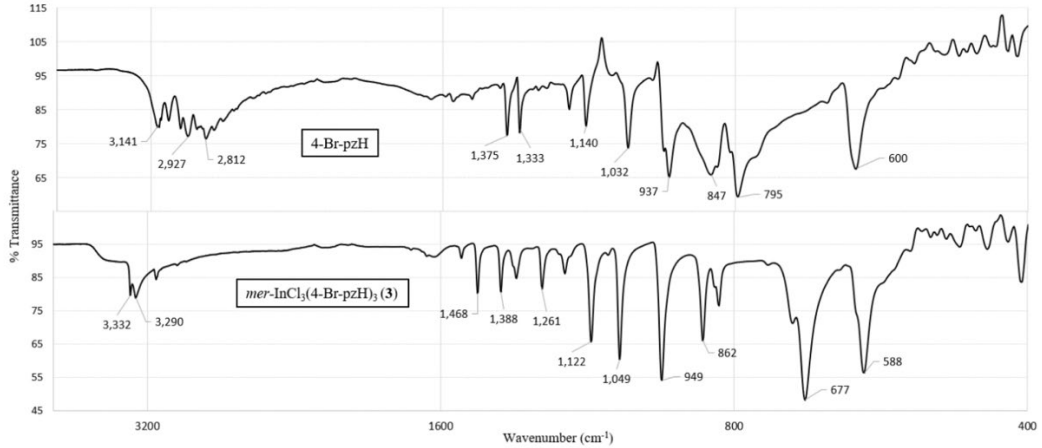

Figure A9. FTIR spectra of free 4-Br-pzH and complex **3**.

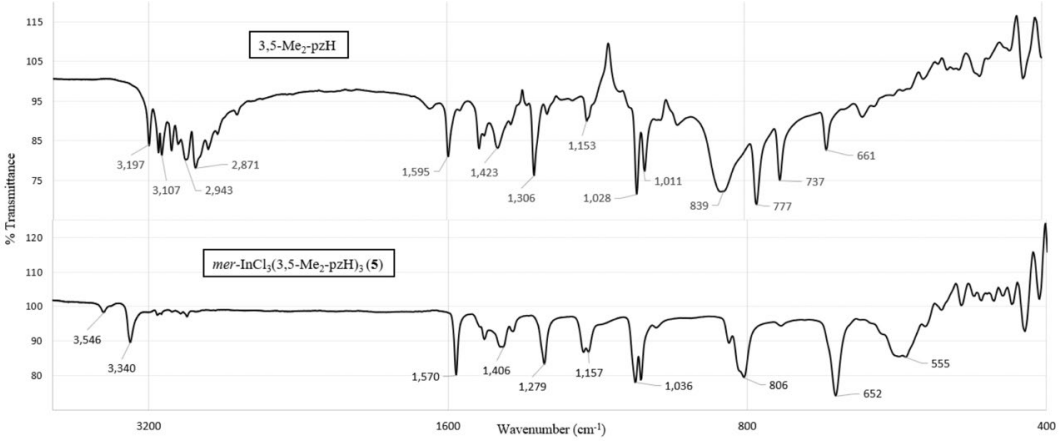

Figure A10. FTIR spectra of free 3,5-Me_2-pzH and complex **5**.

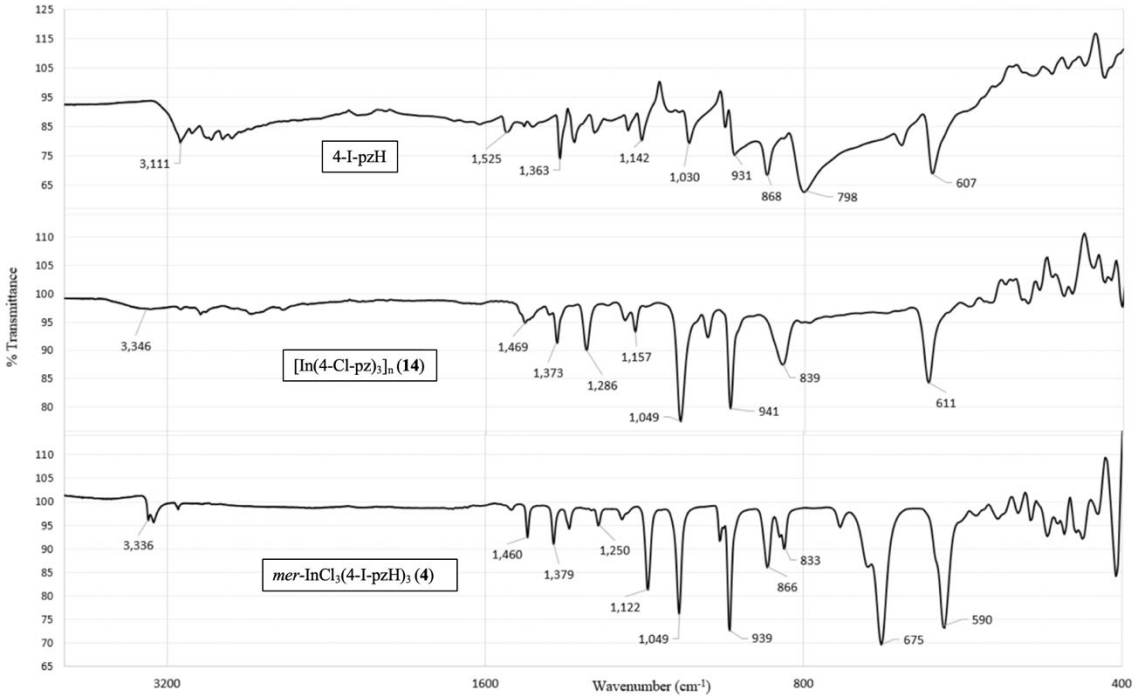

Figure A11. FTIR spectra of free 4-I-pzH, and complexes **4** and **14**.

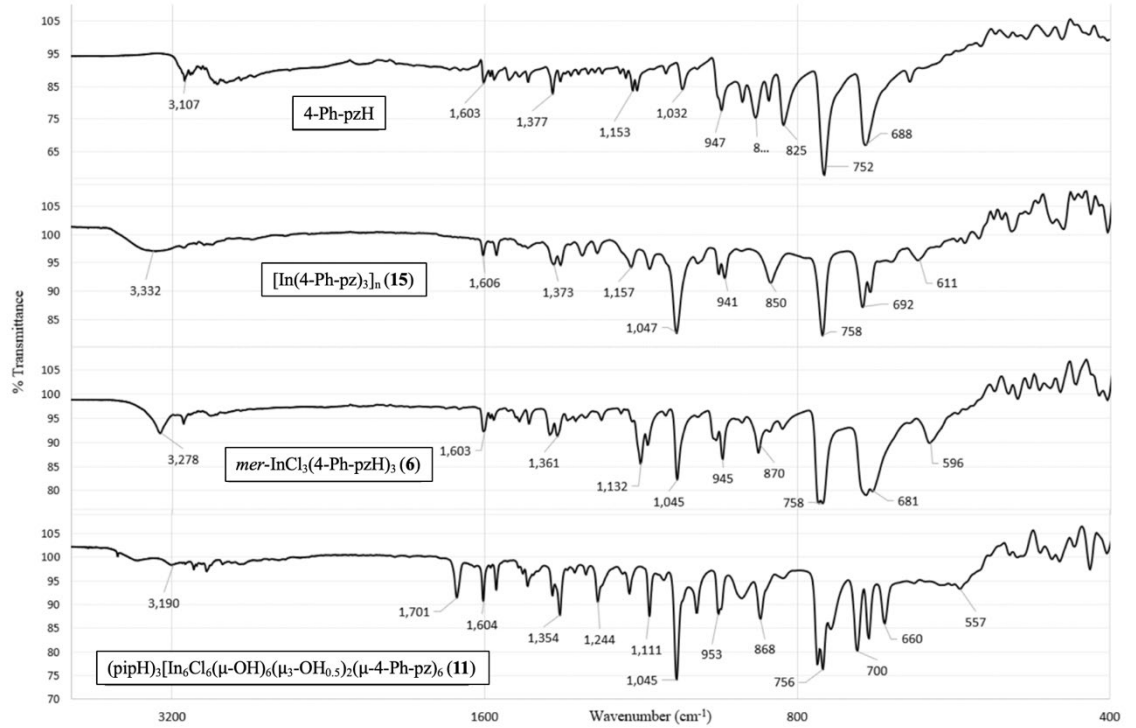

Figure A12. FTIR spectra of free 4-Ph-pzH and complexes **6**, **11**, and **15**.

- Appendix Figures: Chapter 4

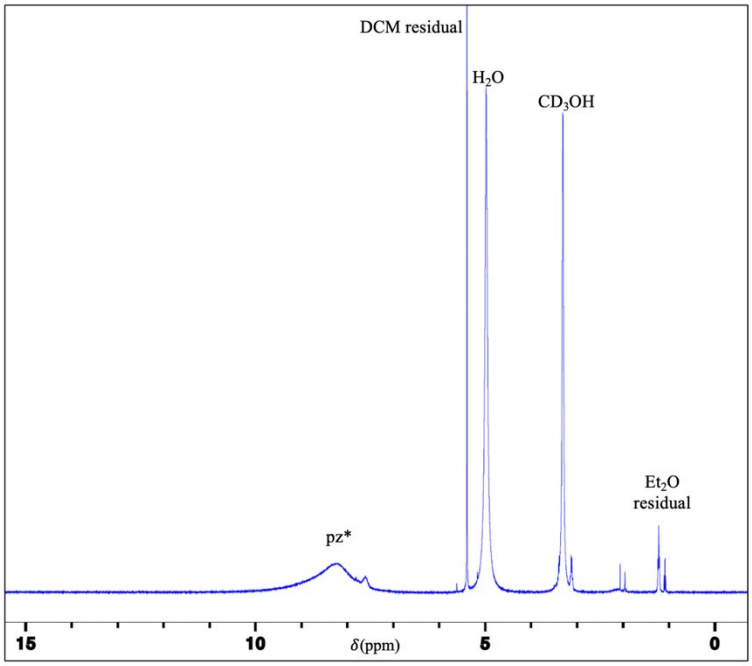

Figure A13. ^{1}H NMR of Fe-intermediate (**21**) in CD_3OD at 400 MHz at ambient temperature (pz* = 4-I-pzH or 4-I-pz).

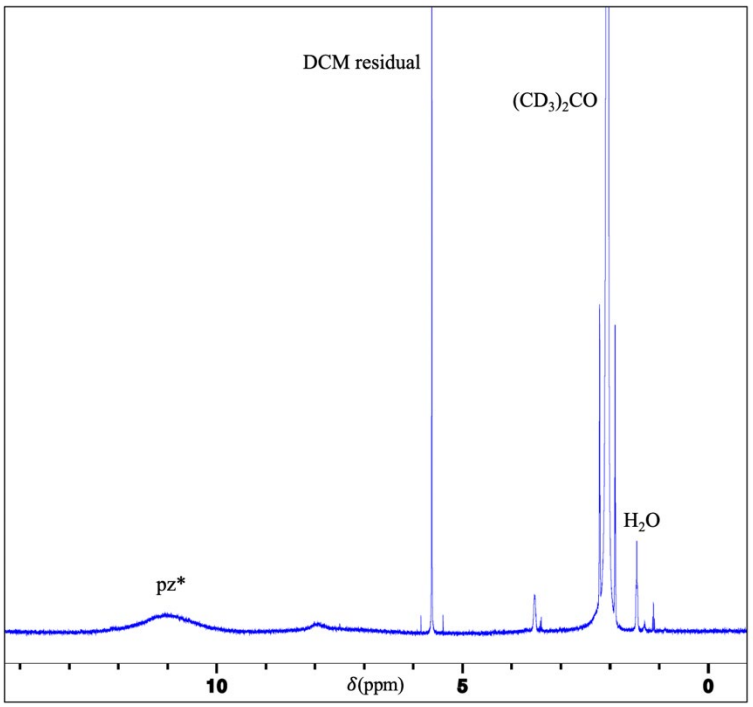

Figure A14. ^{1}H NMR of Fe-intermediate (**21**) in $(CD_3)_2CO$ at 400 MHz at ambient temperature (pz* = 4-I-pzH or 4-I-pz).

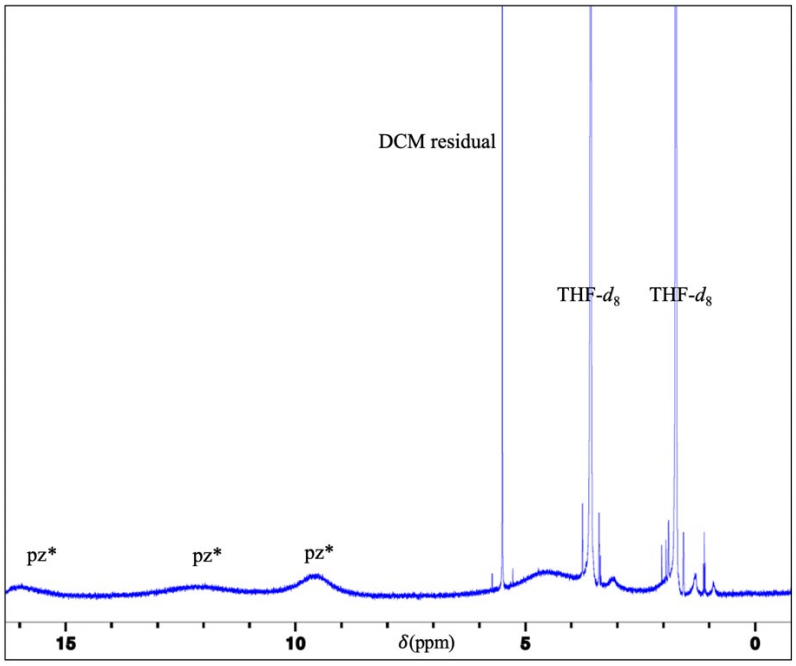

Figure A15. ^{1}H NMR of Fe-intermediate (**21**) in THF-d_8 at 400 MHz at ambient temperature (pz* = 4-I-pzH or 4-I-pz).

VITA

SUSANA HERRERA

Born, Havana, Cuba

2013-2017	Bachelor of Science in Biological Sciences Florida International University, Honors College Miami, Florida
2013-2017	Bachelor of Science in Chemistry Florida International University, Honors College Miami, Florida
2021	NNSA MSIPP Intern Sandia National Laboratory Livermore Remote
2022	Master of Science in Chemistry – Inorganic Chemistry Florida International University Miami, Florida
2022-2023	NNSA Nuclear Non-Proliferation Graduate Fellow Pacific Northwest National Laboratory Lawrence Livermore National Laboratory Livermore, California
2019 -2023	Doctoral Candidate Florida International University Miami, Florida

PUBLICATIONS AND PRESENTATIONS

Herrera, S.; Rivero, K. I.; Guzmán, A.; Cedeño, J.; Miksovska, J.; Raptis, R. G. Mononuclear, Hexanuclear and Polymeric Indium(III) Pyrazolido Complexes; Structural Characterization, Dynamic Solution Studies and Luminescent Properties. *Dalton Trans.* 2022, *51* (37), 14277–14286. https://doi.org/10.1039/D2DT01901A

Herrera, S.; Yoshinaga, M.; Raptis, R. G. Antibacterial properties of nine indium(III) complexes of substituted pyrazoles/pyrazolate and the structural and solution characterization of the *mer*- and *trans*-indium(III) complexes of 4-Me-pzH. *J. Inorg. Biochem.* 2023, (*submitted*)

Rue, K.; Herrera, S.; Chakraborty, I.; Mebel, A.; Raptis, R. G. 4-Halogenated-1H-Pyrazoles: Crystal Structure Determination of 4-Iodo-1H-Pyrazole and Spectroscopic Comparison. *Crystals*. 2023, (*submitted*)

Baker, A. and Herrera, S. "Cerium doped Galfenol magnetostrictive material manufacturing" The Minerals, Metals & Materials Society (TMS) 2023 Annual Meeting and Exhibition. San Diego, California.